

Low-energy stereodynamics of ion-forming reactions

Présentée le 29 mars 2021

Faculté des sciences de base
Laboratoire de chimie physique moléculaire
Programme doctoral en chimie et génie chimique

pour l'obtention du grade de Docteur ès Sciences

par

Junwen ZOU

Acceptée sur proposition du jury

Prof. J. Vanicek, président du jury
Prof. A. Osterwalder, directeur de thèse
Prof. S. Y. T. van de Meerakker, rapporteur
Prof. R. Wester, rapporteur
Dr M. Drabbels, rapporteur

大音希声，大象无形
—《道德经》

Acknowledgements

This thesis would not have been accomplished without the contribution and the support of many people. First of foremost, I would like to thank my supervisor, Andreas Osterwalder, for giving me the opportunity to work in his group and on this challenging topic. He not only provided the basic ideas for all the experiments but also gave supportable suggestions when I met the difficulties. Without his encouragement, some experiments would never become possible.

My science appreciation goes out to Sean Gordon for being the best colleague since the first day we met. His broad knowledge of molecular dynamics and work performance taught me to pursue excellence. I must also acknowledge your great work as the main person who set up the merged beam apparatus with the field manipulation. Without his help, I would never grow up in the field of molecular dynamics so quickly. I also want to thank my group members: Tanteri Silvia, Credidio Bruno, Gkogkoglou Nikolaos and Ian Oesterle. I truly appreciate the good time we have shared together and thanks for your support. As a member in LCPM, I thank the whole members of LCPM: Prof. Thomas Rizzo, Prof. Rainer D. Beck, Oleg Boyarkine, Bo-Jung Chen, Ana Gutierrez Gonzales, Jörn Werdecker, Lei Yue, Stephan Warnke, Voronina Liudmila and Scutelnic Valeriu. This big research family really gives me many happy moments here. In addition to the researchers, I appreciate working with the electronic and mechanical workshop at ISIC. Without their help, the design of the experimental apparatus can't be true in the actual world.

I could like to thank all my friends in Lausanne whose names can be in a long list: Dong Liu, Junrui Zhang, Xingyu Wu, Borui Guan, Zhenzhu Meng, Yanqi Liu, Tanxi, Xiangli Yi, Sijie Liu, Jiande Zhou, Zhengchao Wang, Ranqing Zhan, Zhipeng Li, Xiaoli Li, Xiaowang Liu, etc. I appreciate I have the chances to meet all of you in Switzerland.

At the bottom of the part, my deepest appreciation is to my parents. Words cannot describe how much I gain from your endless support in many ways. Without them, I might give up during this journey and go in the wrong direction. I would continue this journey in science.

Lausanne, 15th, December, 2020

Junwen

Abstract

In this thesis, an experimental study of low-temperature stereodynamics in the reactive scattering of $\text{Ne}(^3P_2) + \text{X}$ collisions ($\text{X} = \text{Ar}, \text{Kr}, \text{Xe}, \text{CO}$ and N_2) is presented. The steric effect of $\text{Ne}(^3P_2)$ in these reactions is observed experimentally using a controllable magnetic field. The observations are interpreted using classical and quantum models. This study provides state-selected stereodynamics over a wide range of collision energies from 1000 K down to sub-Kelvin energies using a combination of the merged beam technique and external field manipulation.

The key parameter to characterize the steric effect in these reactions is the branching between different possible reaction channels as a function of magnetic field direction. These branching ratios are obtained for individual states that differ only in Ω , the projection of the neon total angular momentum vector on the inter-particle axis, by using a Monte-Carlo fitting algorithm to fit an analytical expression for the relative importance of the different, state- and process-specific, reaction channels to the experimental data. From the comparison of these experimental data, several interesting dynamical phenomena are found, including the reorientation effect and predissociation in atom-molecule collisions, which provides a new way to understand the reaction dynamics at low temperatures.

Finally, we use a combination of an electrostatic hexapole and (2+1) resonance-enhanced multiphoton ionization to produce and characterize an oriented ammonia sample (ND_3) using a controllable electric field, which provides a method to study the stereodynamics of $\text{Ne}(^3P_2)$ with oriented polar molecules.

Keywords

Cold chemistry, Stereodynamics, Penning ionization, Merged beam

Résumé

Dans cette thèse, une étude expérimentale de la stéréodynamique à basse température dans la diffusion réactive des collisions $\text{Ne}(^3P_2) + \text{X}$ ($\text{X} = \text{Ar}, \text{Kr}, \text{Xe}, \text{CO}$ et N_2) est présentée. L'effet stérique de $\text{Ne}(^3P_2)$ dans ces réactions est observé expérimentalement en utilisant un champ magnétique contrôlable. Les observations sont interprétées à l'aide de modèles classiques et quantiques. Cette étude fournit une stéréodynamique sélectionnée par état sur une large gamme d'énergies de collision allant de 1000 K jusqu'à des températures de moins d'un Kelvin en utilisant une combinaison de la technique du faisceau fusionné et de la manipulation du champ externe.

Le paramètre clé pour caractériser l'effet stérique dans ces réactions est le rapport entre deux canaux réactives en fonction de la direction du champ magnétique. Ces rapports de ramification sont obtenues pour des états individuels qui diffèrent uniquement par la projection du vecteur de moment angulaire total du néon sur l'axe interparticulaire, en utilisant un algorithme d'ajustement Monte-Carlo pour ajuster une expression analytique de l'importance relative des différents canaux de réaction, spécifiques à l'état et au processus, pour les données expérimentales. La comparaison de ces données expérimentales permet de découvrir plusieurs phénomènes dynamiques intéressants, notamment l'effet de réorientation et la prédissociation dans les collisions entre atomes et molécules, ce qui offre une nouvelle façon de comprendre la dynamique des réactions à basse température.

Enfin, nous utilisons une combinaison d'un hexapole électrostatique et d'une ionisation multiphotonique (2+1) améliorée par résonance pour produire et caractériser un échantillon d'ammoniac orienté (ND_3) en utilisant un champ électrique contrôlable, ce qui fournit une nouvelle méthode pour étudier la stéréodynamique du $\text{Ne}(^3P_2)$ avec des molécules polaires orientées.

Mots-clés

Chimie froide, Stéréodynamique, Ionisation Penning, Faisceau fusionné

Contents

Acknowledgements	i
Abstract	iii
Résumé	v
1 Introduction	1
1.1 Cold chemistry	1
1.2 Reaction dynamics	2
1.2.1 Chemi-ionization process	2
1.2.2 Stereodynamics	4
1.3 Methods in cold chemistry	6
1.3.1 Absolute velocity manipulation	6
1.3.2 Intersection angle reduction between the reactants	7
1.4 Low-energy stereodynamics	9
1.5 Scope of the thesis	10
2 Theoretical Concepts	11
2.1 Production of supersonic beams	11
2.2 Kinematics of crossed and merged beams	14
2.3 Manipulation of neutrals	17
2.4 Coupling and predissociation	22
2.5 Orientation effect	24
2.6 Numerical methods in chemi-ionizations	26
3 Experimental apparatus and analysis	29
3.1 Experimental apparatus	29
3.1.1 Atomic/molecular beams	31
3.1.2 Magnetic hexapole	32
3.1.3 Orienting fields	34
3.1.4 Detection	37
3.2 Resonance-enhanced multiphoton ionization and detection	39
3.3 Data analysis and fitting	42
4 Stereodynamics of Ne* with rare gases	45
	vii

Contents

4.1	Introduction	45
4.2	Stereodynamics of the $\text{Ne}^* + \text{Rg}$ reactions	47
4.3	Sub-Kelvin stereodynamics of the $\text{Ne}^* + \text{Ar}$ reaction	49
4.4	Dynamics of the $\text{Ne}^* + \text{Rg}$ reactions	53
5	Stereodynamics of Ne^* with diatomic molecules	55
5.1	Introduction	55
5.2	Stereodynamics of the $\text{Ne}^* + \text{N}_2$ reaction	56
5.3	Sub-Kelvin stereodynamics of the $\text{Ne}^* + \text{N}_2, \text{CO}$ reactions	58
5.4	Reaction dynamics of the $\text{Ne}^* + \text{N}_2, \text{CO}$ reactions	66
6	Preparation of oriented ND_3 molecules	69
6.1	Introduction	69
6.2	Experimental apparatus	71
6.3	Experimental result	72
7	Conclusion and outlook	77
	Curriculum Vitae	91

List of Figures

2.1	Cooling effect that results in the adiabatic expansion through a pulsed value (Here, metastable neon is at ≈ 170 K). On the left, neon gas is kept at a pressure of a few atmospheres. The blue curve shows its speed distribution in the lower plot. Once the orifice is opened, the gas expands through a nozzle and rapidly cools. The beam then is filtered by a skimmer shown in the green curve, which generates a beam pulse with a narrow velocity distribution by adiabatic cooling.	12
2.2	Arrangement of a crossed molecular beam apparatus. In this frame, two molecular beams, whose mass of particles are m_1 and m_2 , propagate with velocities \vec{v}_1 and \vec{v}_2 , respectively. These two beams then cross at the center of a reaction zone at an angle θ . Products are collected by a rotatable detector.	14
2.3	Schematic diagram of the energy resolution using the time-sliced technique. (Adapted from Ref. [88])	15
2.4	Zeeman effect of metastable neon in 3P_2 state.	18
2.5	Rotational quantum numbers of a polar molecule in space. (Reproduced from Ref. [88])	20
2.6	First order Stark shift of ND_3 in the $J_K = 1_1$ state in electric fields. States are labeled as $ J, MK\rangle$.	21
2.7	Schematic diagram of the angular momentum \vec{J} in the laboratory reference frame Q and in the molecular frame whose projections are M_J and Ω respectively.	23
2.8	Schematic showing the potential direction of the angular momentum vectors \vec{J} with a reference axis (shown in red) for an oriented sample and an aligned sample. The corresponding M_J distributions, arising from the projection of the molecular angular momentum vector \vec{J} upon a symmetry axis z for an oriented sample and an aligned sample.	24
2.9	Schematic view of the potential curves in the $\text{Ne}^* + \text{Ar}$ reaction.	27
3.1	Reactions occur in a tunable magnetic field created by a pair of solenoid magnets. B fields, TOF-MS and MCP are the abbreviations of magnetic fields, time-of-flight mass spectrometer, and microchannel plates, respectively.	30
3.2	(a) Calculated transmission curves for Ne^* in the $M_J = 1$ (black line) and $M_J = 2$ (red line) states, respectively. (reproduced from Ref. [89]) The magnetic field strengths in the two parts of the hexapole: (b) the hexagonal part and (c) the merging part. The black circle is the inner opening. (reproduced from Ref. [88])	32

List of Figures

3.3	(a) Rendering of the magnetic orientating field setup in the interaction zone. (b) Schematic of the magnetic field arrangement. (c) Calibration diagram of the solenoid magnetic field as a function of the applied current.	34
3.4	Illustration of a magnetic field control loop. OCR is the abbreviation of optical character recognition.	35
3.5	Illustration of a Wiley-McLaren time-of-flight mass spectrometer with solenoid magnets. MCP is the abbreviation of microchannel plate.	37
3.6	Time-of-flight spectrum at a collision energy of 244 cm^{-1} and $\theta_{\text{KB}} = 90^\circ$ in the $\text{Ne}^* + \text{CO}$ reaction. BG is short for the background.	38
3.7	(a) Illustration of the REMPI configuration. Linearly polarized laser light enters perpendicular to the experimental setup with the polarization ϵ . (b) REMPI signals are obtained by changing the magnetic field at a fixed linear polarization of the excitation laser light (blue cross), and by rotating the laser light polarization at a fixed magnetic field (red square).	40
3.8	a) Time-of-flight spectra as a function of the magnetic field direction, expressed in the laboratory reference frame, for the $\text{Ne}^* + \text{Kr}$ reaction at a collision energy of 313 cm^{-1} . b) Experimental and fitted reactivities $\text{NeKr}^+/\text{Kr}^+$ as a function of θ_{KB} in the molecular reference frame.	42
3.9	Ω specific reactivities for the $\text{Ne}^* + \text{Kr}$ reaction at a collision energy of 313 cm^{-1}	43
4.1	Reactivities and interpolated and fitted surfaces for different rare gas atoms reacting with Ne^*	47
4.2	Experimental reactivities $\sigma_{\text{AI}}^\Omega/\sigma_{\text{PI}}^\Omega$ as a function of collision energy. In each case, the values for $\Omega = 0, 1$, and 2 are shown in black, red, and blue, respectively. The shaded areas represent one standard deviation.	48
4.3	Histogram of the specific reactivities at 400 cm^{-1} for the $\text{Ne}^* + \text{Ar}$, Kr and Xe reactions (left to right).	48
4.4	Steric effect for Ar (red), Kr (blue) and Xe (violet) defined as the ratio between the reactivities R at $\theta_{\text{KB}} = 90^\circ$ and $\theta_{\text{KB}} = 0^\circ$ as a function of collision energy. A value of 1 indicates no dependence on the Ne^* orientation.	49
4.5	Sample of raw ToF spectra at $\theta_{\text{KB}} = 5^\circ$ for (a) $E_{\text{coll}}/k_{\text{B}} = 370 \text{ K}$ and (b) $E_{\text{coll}}/k_{\text{B}} = 25 \text{ mK}$. (c), (d) The reactivity, $I_{\text{AI}}/I_{\text{PI}}$, as a function of θ_{KB} for the same collision energies. BG is short for background.	49
4.6	Ion yields of the associative ionization and Penning ionization channels at different collision energies, $E_{\text{coll}} = 22 \text{ mK}$ (a), 175 K (b) and 575 K (c).	50
4.7	Experimental (a) and fitted (b) two-dimensional plots of the complete angular-dependent data cover the entire energy range. The white region, overlaid by a smoothed contour, shows the area in which the PI and AI channels have equal ion yields $R(\theta, E_{\text{coll}}) = 1$. The properties of the slices at $\theta_{\text{KB}} = 90^\circ$ (blue dotted line) and $\theta_{\text{KB}} = 180^\circ$ (red dashed line) are given above the heat maps.	51
4.8	Experimental (red) state-dependent reactivities that quantify the steric effect are compared with the theoretical values (black).	51

4.9	The steric effect in the $\text{Ne}^* + \text{Ar}$ reaction. A value of 1 indicates no preference for specific orientations, hence no steric effect, while a value different from 1 indicates a strong dependence on the orientation. The red-shaded area below ≈ 30 mK shows the region of collision energies where the present experiment does not permit orientation control because the longitudinal and transverse velocities are similar.	52
4.10	(I) Radiative mechanism, occurring at long range and (II) exchange mechanism, taking place at short range.	53
5.1	Experimental and fitted data for the $\text{Ne}^* + \text{N}_2$ reaction. (a) The reactivity across the angular range at 400 cm^{-1} . (b) Ω specific reactivities as a function of collision energy. (c) Experimental and (d) fitted reactivities across the energy range of the cross-beam experiment.	56
5.2	Histogram of the Ω specific reactivities at 400 cm^{-1} for $\text{Ne}^* + \text{Ar}$, Kr , Xe , and N_2 (left to right).	57
5.3	Examples of angle-dependent ion yields: at $E_{\text{coll}}/k_B = 600$ mK for (a) the $\text{Ne}^* + \text{CO}$ reaction and (c) the $\text{Ne}^* + \text{N}_2$ reaction and at $E_{\text{coll}}/k_B = 352$ K for (b) the $\text{Ne}^* + \text{CO}$ collision and (d) the $\text{Ne}^* + \text{N}_2$ collision.	58
5.4	Experimental ratio $I_{\text{NeX}^+}/I_{\text{X}^+}$ ($\text{X} = \text{CO}$ and N_2) as a function of θ_{kB} and collision energy in the range of 0.06–700 K for the $\text{Ne}^* + \text{CO}$ reaction (top) and the $\text{Ne}^* + \text{N}_2$ reaction (bottom).	59
5.5	Raw ion yield ratio for the production in the $\text{Ne}^* + \text{N}_2$, CO reactions as a function of collision energy.	59
5.6	Steric effect for N_2 (blue symbols) and CO (red symbols), defined as the ratio between the reactivities $r(\theta_{\text{kB}} = 90^\circ)$ and $r(\theta_{\text{kB}} = 180^\circ)$, as a function of energy.	60
5.7	Predissociation probability P_{pd} of the AI products $[\text{Ne-X}]^+$, obtained by fitting Eq. 5.2 to the experimental data, for $\text{X} = \text{CO}$ (red) and $\text{X} = \text{N}_2$ (blue).	61
5.8	Ratio of the angle-integrated AI and PI yields for N_2 (blue) and CO (red). In contrast to the data in Fig. 5.5, these data take into account predissociation, using Eq. 5.3.	62
5.9	Experimental reactivity: for (a) the $\text{Ne}^* + \text{N}_2$ reaction and (c) the $\text{Ne}^* + \text{CO}$ reaction as a function of collision energy. Fitted reactivity as a function of collision energy for (b) the $\text{Ne}^* + \text{N}_2$ reaction and (d) the $\text{Ne}^* + \text{CO}$ reaction. In all cases, the left side shows the energy range of 0.3–40 K, and the right side shows the range of 40–700 K. (Left) Raw data. (Right) Actual AI/PI obtained through a fit using Eq. 5.3.	63
5.10	Reaction cross section ratios for $\Omega = 0, 1$, and 2 (a)–(c) for the $\text{Ne}^* + \text{CO}$ reaction and (d)–(f) for the $\text{Ne}^* + \text{N}_2$ reaction. The error bars represent the one standard deviations of the cross-section histograms obtained from the fit.	65

List of Figures

5.11	Relevant energy levels for the $\text{Ne}^* + \text{CO}$ reaction. Successive vibrational levels of CO are indicated in each case. For both accessible electronic states, the levels of the bare ion are shown on the left, and those of the complex are shown on the right.	66
5.12	Relevant energy levels for the $\text{Ne}^* + \text{N}_2$ reaction. AI, PI, and PD stand for associative ionization, Penning ionization, and predissociation, respectively.	67
6.1	Experimental branching ratios as a function of collision energy in the $\text{Ne}^* + \text{NH}_3$ reaction (blue circles) and $\text{Ne}^* + \text{ND}_3$ reaction (red squares). (Reproduced from Ref. [140])	70
6.2	(a) Side view of the apparatus used for the orientation of ND_3 . Molecules are injected from the left. (b) Front view of the printed hexapole element. The upper part is metal plated while the lower part is the electrically insulating base. (c) Top view of a single guide element.	72
6.3	Experimental (red and blue) and theoretical (black) REMPI spectra. The top spectrum was obtained when the guide voltage difference was 18 kV, the middle spectrum was recorded with the guide switched off. The theoretical spectrum was calculated using the PGOPHER software, assuming a rotational temperature of 15 K.	73
6.4	(a),(b) REMPI spectra recorded through the $\text{B}(\nu_2 = 6)$ and $\text{B}(\nu_2 = 5)$ vibrational level, respectively. Blue traces, signal of the pure supersonic expansion; red traces, signal from guided molecules.	74
6.5	Experimental (2+1) REMPI spectra of ND_3 recorded with different relative directions to the laser polarization ϵ , electric field axis \vec{E} , and beam velocity \vec{k} . Panels a and b were recorded with the electric field parallel and perpendicular to the molecular beam, respectively. In both panels the blue (red) spectrum was obtained with the laser polarization aligned parallel (perpendicular) to the electric field axis.	75
6.6	(2+1) REMPI signal at 63022.3 cm^{-1} of ND_3 as a function of angle between the laser polarization ϵ and the beam velocity \vec{k} when the angle between the electric field \vec{E} and the beam velocity \vec{k} is 0° (a), and 90° (b).	76

List of Tables

2.1	Strength of the magnetic moments for metastable neon in the $^3P_{0,1,2}$ states . . .	19
2.2	Hund's coupling cases	22
3.1	Properties of the supersonic valves.	31
3.2	Experimental conditions for the orientation detection	39
4.1	Branching ratios in the $\text{Ne}(^3P_{0,2}) + \text{Ar, Kr and Xe}$ collisions	45
6.1	Excited state and ground state for selected transitions in the (2 + 1) REMPI spectrum of ND_3	73

1 Introduction

To this date, almost 200 molecules containing up to 13 atoms have been identified in the interstellar space, indicating a rich and active chemical environment.[1] Investigating the properties of their reactions in naturally-occurring cold environments whose temperatures can be as low as a few Kelvins will not only help us learn about the chemistry of interstellar space but also improve our understanding of low-energy reaction dynamics in general, which is also a major focus in this thesis.

1.1 Cold chemistry

In the past 40 years, several different methods for the production and application of cold ($T < 10$ K) and ultracold matter ($T < 1$ mK) have been developed.[2, 3, 4, 5] These methods initially concentrated on cooling atoms, later expanding into cold and ultracold molecular systems, which provide a way to study cold chemistry.[6, 7, 8, 9] Using these methods not only allows us to investigate the properties of reactions postulated to be of astrochemical importance but also provides experimental data for the development of theory in cold chemistry. At low temperatures, various features related to the study of cold chemistry can be found.[10] The first one is minimization of kinetic energy in a collision, a consequence of which is that only a few partial waves contribute to the process that can greatly simplify the reaction dynamics.[11, 12] In the process of reduction of kinetic energy, we can also study the transition from classical to quantum reaction dynamics in collisions. At these low temperatures, particles display wave-like behavior, inducing different phenomena such as tunneling and scattering resonances.[11, 13] In addition to wave-like behavior, long interaction times in cold collisions provide the opportunity to undertake accurate measurements of reaction systems. These special environments enable high-precision characterization and determination of various properties of reactions such as rate coefficients, collision cross sections and branching ratios.[11, 14, 15]

When we use the reaction theories at high temperatures to model these cold reactions, it is found that they no longer work because at low temperatures quantum mechanical effects become important that are not included in high-temperature reactivity models. These in-

clude tunneling effects and resonances which are only visible when a low number of angular momentum partial waves contribute to the reaction. An altogether different description of chemical processes may be required when the de Broglie wavelength of the reactants becomes larger than relevant inter-particle distances. Therefore, researchers have developed various theories to model chemical processes in these regions.[16, 17]

In addition to cold collision, nowadays, we simultaneously control other reaction parameters such as selection of different quantum states of the reactants, and alignment and orientation of the reactants in the same collision.[12, 18, 19] The purpose of controlling these reaction parameters is to improve our understanding of how reactions occur at a fundamental level and to explain the influence of each variable on the outcome of a reactive collision under cold conditions.

1.2 Reaction dynamics

Reaction dynamics is a field within physical chemistry, attempting to understand the molecular-level mechanism of elementary chemical and physical processes, and the study of why, how and how fast chemical processes take place.[20] In a reaction, energy barriers need to be overcome by reactants to proceed towards products.[21] At low temperatures, if there is an energy barrier, the reaction rate is usually very low.[6]

However, some reactions are allowed to occur at very low temperatures because of the absence of the energy barrier. These reactions are good candidates for being studied at low temperatures. They include atom-molecule reactions, ion-neutral reactions, radical reactions and reactions of electronically or vibrationally excited molecules and unimolecular decompositions.[22]

1.2.1 Chemi-ionization process

Chemi-ionization reactions, as a barrierless reaction, are the formation of an ion through the reaction of a gas-phase reactant with another reactant while also forming new bonds.[23, 24] In such a reaction, an electronically excited atom A^* ionizes a neutral partner, X, provided that the internal energy of A^* is higher than the ionization potential (IE) of X:



which are called Penning ionization (PI), associative ionization(AI), dissociative ionization and rearrangement ionization, respectively. When X is a molecule BC, different reaction channels such as inelastic or bond-breaking dynamics are possible and the last two paths of molecule X

are then dissociated into B^+ and C.[23]

Chemi-ionizations have an important role in planetary atmospheres, interstellar environments, and chemistry and physics in plasma.[25, 26, 27] Different experimental methods have been successfully applied to investigate these reactions at high temperatures including energy-dependent measurements of total and partial ionization cross sections σ , associative to Penning ratios (σ_{AI}/σ_{PI}), Penning ionization electron spectra (PIES).[24, 28, 29]

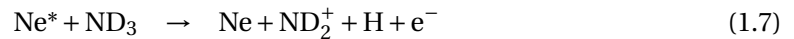
It would be interesting to know what happens when these reactions occur under cold and ultracold conditions as the low-temperature dynamical information is still missing. Due to the recent development of merged beams in neutral-neutral reactions, we have an opportunity to investigate the energy-dependent reaction rate of different chemi-ionization systems such as $He^* + H_2$ and $He^* + NH_3$ reactions and we observed different phenomena such as shape resonance at low temperatures.[11, 29]

One further step of these reactions is to study their stereodynamics at low temperature and we would like to investigate the steric effect when the reaction occurs in resonances. Here we choose chemi-ionizations between oriented neon in 3P_2 state (labeled as Ne^* in this thesis) and ground state reactant X ($X = Ar, Kr, Xe, N_2, CO$). As the internal energy of Ne^* (16.6 eV) is larger than the ionization energy of the X particle,[30] the reaction can occur without supplying additional energies,[3] and we observe two kinds of product ions which correspond to



where Eq. 1.5 and Eq. 1.6 are Penning ionization (PI) and associative ionization (AI), respectively.

In this thesis, we will also discuss the chemi-ionization reaction between Ne^* and ND_3 . This reaction can proceed along two principal pathways:



where the first channel is called dissociative ionization (DI) and the second one is PI. In contrast to the other reactions described in this thesis, associative ionization is not observed in this reaction and the branching ratio between DI and AI is independent of Ne^* orientation and collision energy.[15] In the stereodynamics study between Ne^* and ND_3 , we expect that the branching ratio is sensitive to the orientation of ND_3 and the preparation of oriented ND_3 molecules will be discussed in Chapter 6.

1.2.2 Stereodynamics

Stereodynamics, as defined by Levine,[20] is a concept associated with the chemical shape of molecules in collisions. Its aim is to determine and understand the dependence of reactivity as a function of distance and approach of the reagents. Chemical shape depends not only on the molecule itself, but also on the other reagent: It describes the apparent size and shape of a molecule when it is seen by another reagent atom or molecule in the process of a collision. Stereodynamics has worked as an important tool for explaining the reactivity and interactions in gas-phase reactions, since the first stereodynamics study of the $\text{CH}_3\text{I} + \text{K} \rightarrow \text{KI} + \text{CH}_3$ reaction that was firstly reported in 1966 when CH_3I molecules were oriented in electric fields.[31] A number of experimental techniques to probe chemical shape have been developed in last 40 years and there has been an increase in our understanding of the dynamics of chemical reactions. In this section, we will discuss methods for alignment and orientation of reactants which provide an intuitive way of studying directly the angular dependence of reactivity, including 'brute force' method, optical excitation and hexapole state selection with an external field.[32, 33, 34]

The brute force method uses a homogenous electric field to orient molecules with a permanent electric dipole moment via the second order Stark effect. When the field is applied, the polar molecule will tend to the direction of minimal energy with respect to the field. These molecules will perform a pendular motion if they have damped down into the lowest energy state according to their initial rotational angular momentum. This method requires a large electric field strength that is needed to achieve orientation. As an example, researchers can prepare an oriented molecular beam such as ICl in static electric fields with strengths ranging from 10 to 20 kV/cm.[35, 36]

The optical excitation methods are used to align molecules, typically in pulsed laser fields. Here the cleanest way to induce molecular alignment is done through a single transition between two vibrational levels in different electronic terms by a resonant laser. The alignment depends on the transition dipole moment of a molecule when it absorbs a linearly polarized photon.[37] For example, using an infrared laser, Wang et al.[38] could control the alignment of CHD_3 molecules the reaction of CHD_3 with Cl where they found within vibrational excitation of $\text{CHD}_3(\nu_1 = 1)$, the elongation of the C-H bond can enlarge the range of attack angles when it collides Cl , leading to an increase in the reaction probability.

Using the Stark effect, a polar molecule beam such as OH , OD and CH_2F_2 can be oriented using an electric hexapole(quadrupoles) state selection. This hexapole also works as a selector, which depends on the field strength.[39, 40] When this technique is used in a collision, we can accurately resolve differential cross sections for the corresponding reaction. For example, in the reaction of oriented $\text{NO} + \text{Rg}$ ($\text{Rg} = \text{Ar}$ and Kr) reactions, their differential cross sections for collisions in NO-Rg and ON-Rg configurations could be resolved using the velocity-mapped image detection in a controllable electric field.[41, 42]

In addition to the Stark effect, magnetic guides based on the Zeeman effect can prepare an

oriented paramagnetic sample. Kasai's group have reported several stereodynamics studies including oriented $\text{Ar}(^3P_2) + \text{CF}_3\text{H}$, [43], oriented $\text{Xe}(^3P_2) + \text{CF}_3\text{I}$, [44], oriented $\text{Kr}(^3P_2) + \text{CO}$, [45] and oriented $\text{Rg}(^3P_2) + \text{Halogen(X)}$ -containing molecules [46], where they found that the reaction products, such as M_J dependence for the chemiluminescence, depended on the orientation of reactants.

1.3 Methods in cold chemistry

In cold chemistry, we use temperature as a measure of the mean energy in chemical reactions, i.e. $E = k_B T$ where T and k_B are the temperature and the Boltzmann constant. In that sense, chemistry at low temperatures is actually chemistry at low energies. The collision energy in such a chemistry system only depends on the relative motion of the colliding reactants, which can be manipulated by either (1) tuning the relative velocities of reactants in a molecular reference frame or (2) controlling their absolute velocities.

To prepare a low energy collision, a necessary condition is the preparation of a cold sample in the laboratory reference frame from a pre-cooling procedure. This procedure is usually performed using supersonic expansion (producing a dense jet at high speed but with a narrow velocity distribution) [47] or buffer gas cooling (cooling atoms and molecules through inelastic collisions with a cryogenic gas, typically He or Ne.) [48] After the pre-cooling procedure, molecular pulses from the source usually are at low translational temperatures (typically ~ 1 K). Further improvement of a lower energy collision will be presented here.

1.3.1 Absolute velocity manipulation

Deceleration

Stark deceleration is a method that makes use of the Stark effect in polar molecules to slow down packets of molecules. [49] The Stark effect can be described by the perturbation in the energy levels of a polar molecule in the presence of an electric field. Depending on its quantum states, the effect can lead to an increase or a decrease in its potential energy, so that the states can be labeled as low-field-seeking states (lfs) or high-field-seeking states (hfs), respectively. [49] The technique was introduced by the group of Meijer who used it to slow a metastable CO molecule beam down to 98 m/s. [50] This technique has been applied to a wide range of polar molecules such as OH, [51] ammonia, [52] and YbF. [53] The group of Meerakker utilized it to investigate chemistry in atom-molecule collisions for probing quantum resonance at low temperatures. [19, 54, 55]

Following the success of Stark deceleration, Zeeman deceleration was developed, [56, 57] based on the Zeeman effect, using magnetic rather than electric fields. This expands the range of species including paramagnetic ones. Several species have been decelerated including H and D atoms, [57] metastable neon, [58] and He₂ molecules. [59] These slow particles have interesting prospects in high-resolution crossed-beam-scattering experiments.

Velocity selection

Velocity selection is another method to produce a slow molecular beam. A molecular beam, expanded from a pinhole nozzle at temperature T , displays a three-dimensional Maxwell

Boltzmann velocity distribution, which is shown by

$$f(v) = \left(\frac{m}{2\pi k_B T}\right)^{3/2} e^{-mv^2/2k_B T} \quad (1.9)$$

where m is the particle mass, k_B is the Boltzmann constant. At any temperature, it is the distribution that shows non-zero probability to have particles with low velocities. In other words, these molecules are translationally cold. A bent guide was developed using electric fields to select the cold part of the distribution.[60, 61, 62] Based on this, researchers in Munich developed a 'centrifuge' decelerator to produce a cold continuous molecule (~ 1 K) beam from a liquid nitrogen-cooled source. This setup includes a circular quadrupole guide and a rotating quadrupole guide that can decelerate a beam of CH_3F from 200 m/s to 15 m/s.[63] More recently, the same group has observed collisions between guided and decelerated CH_3F and ND_3 molecules inside the centrifuge.[64]

1.3.2 Intersection angle reduction between the reactants

Besides absolute velocity preparation, the manipulation of collision energy in a reaction can be also achieved by intersection angle reduction between reactants. Several examples are given here.

Crossed beam with small intersection angles

A typical example of small-angle scattering is reported by Bergeat et al.[65] where they studied inelastic $\text{CO}(j=0) + \text{He}$ collisions at a intersection angle that varies between 90° and 12.5° reaching collision energies as low as 4 cm^{-1} and they characterized the quantum-dynamical resonances in CO-He inelastic collisions with rotational $\text{CO}(j=0 \rightarrow 1)$ excitation.

Recently, a combination of Stark decelerator and reactant angle manipulation was used to study collisions between state-selected NO molecules and He atoms at $5\text{--}10^\circ$ intersection angles between the reactants where the collision energy resolution was pushed down to $0.2\text{--}3 \text{ cm}^{-1}$ and $0.8\text{--}8.5 \text{ cm}^{-1}$ allowing the observation of scattering resonances in differential collision cross sections.[55]

CRESU

The reaction kinetics in uniform supersonic flow technique (CRESU) was firstly introduced by Rowe and Marquette in the 1980s.[66] Initially, it was used for studying ion-molecule reactions and was later expanded to neutral-neutral reactions.[67] This technique involves the isentropic expansion of a mixture of gas from a high pressure reservoir into a vacuum through a Laval nozzle. The investigated reaction is initiated by creating one reactant from a predecessor in a beam by pulse laser photolysis or electron bombardment. The reactions were investigated using the CRESU method at temperatures as low as 5.8 K and the experimental

Chapter 1. Introduction

result was consistent with quantum calculations on a potential energy surface within long-range interactions.[68]

Intrabeam studies

In intrabeam studies, two different species are mixed in a supersonic expansion. By implementing a dual-slit chopper, these two species propagate and collide with separately fixed speeds in the interaction region at $\approx 0^\circ$. Based on this, the group of Suits performed an intrabeam study of Rydberg Xe + Xe reaction and found l -changing collisions at sub-Kelvin temperatures.[69] At the same time, inelastic scattering of HD with H₂ and D₂ in an intrabeam experiment was reported by Zare's group and they found a reorientation in collisions.[8] Recently, The group of Suits has employed a combination of velocity map imaging (VMI) and near-copropagating beam technique and has reported NO + Ar collision at ≈ 1 K where they found rotational de-excitation of NO after collisions with Ar at collision energies of 45 cm⁻¹ and 32 cm⁻¹. [70]

Merged beam studies

The intersection angle can also be minimized in a merged beam experiment, which has been used to study ion-neutral reactions since 1960s.[71, 72, 73] Its key element is to force the propagating path of one reactant to align with that of another so that the intersection angle becomes zero degrees. The first neutral-neutral merged beam experiments were reported by Narevicius's group and our laboratory.[11, 15] The reaction dynamics of several Penning ionization reactions, including Ne(³P₂) + ND₃, [15] He(³S₁) + NH₃, [29] and Ne(³P₂) + CH₃F, [74] from room temperature to sub-Kelvin were analyzed.

1.4 Low-energy stereodynamics

Previously, stereodynamics studies were mainly performed at collision energies above 300 K.[75, 76] The combination of low-energy collision with steric control is interesting because of some interesting effects such as quantum resonance, dynamical reorientation at low temperatures.[8, 77]

Rapid development of cooling techniques has provided the opportunity to investigate low-energy stereodynamics. However, until now, only a few reaction systems have been reported. The first ultracold stereodynamics of $\text{KRb} + \text{KRb}$ reaction in an electric field was reported by Ye's group.[78] In the sub-Kelvin region, Zare and coworkers analysed[18] the stereodynamics of oriented $\text{HD} + \text{D}_2$ using the intrabeam method. In this study, Stark-induced adiabatic Raman passage (SARP) was utilized to prepare ro-vibrationally excited HD molecules in the $(\nu = 1, j = 2)$ state with the molecular bond axis aligned either parallel or perpendicular to the molecular axis while their colliders D_2 molecules were kept in the $(\nu = 0, j = 0)$ state. In collisions at a collision energy of ~ 1 K, it was found that the rotational relaxation time of HD in the $\nu = 1, j = 1$ state was three times more likely to occur when HD was aligned perpendicular rather than parallel to the flight axis.

In our laboratory, paramagnetic oriented atom Ne^* was utilized to investigate the $\text{Ne}^* + \text{Ar}$ reaction and the $\text{Ne}^* + \text{CO}$, N_2 reactions using a merged beam apparatus whose details will be presented in the thesis.

1.5 Scope of the thesis

This thesis reports an experimental investigation of low-energy stereodynamics of the energy transfer reactions $\text{Ne}^* + \text{X}$ ($\text{X} = \text{N}_2, \text{CO}, \text{Ar}, \text{Kr}$ and Xe). Collision energies in the range of 0.02 K–1000 K are obtained using merged beam techniques. The orientation of Ne^* is controlled using magnetic fields. The experimental details and results are presented in the following order: Chapter 2 introduces the theoretical concepts that are used in the thesis including the kinetic energy of collisions, guiding dynamics and orientation effect; Chapter 3 presents the experimental details, including merged beam apparatus, magnetic hexapole, external field manipulation, detection method and fitting method for experimental branching ratios; in Chapter 4, the stereodynamics of Ne^* with other rare-gas atoms collisions in crossed and merged beams are investigated; in Chapter 5 the experiments are extended to $\text{Ne}^* + \text{molecule}$ collisions and it is shown that predissociation needs to be taken into account for the data interpretation; Chapter 6 presents our most recent efforts to prepare a sample of oriented ND_3 molecules using electric fields; Chapter 7 concludes this work and describes the prospects for future research.

2 Theoretical Concepts

This chapter provides an overview of theoretical concepts related to the work presented herein. First, the basic concepts for the description of supersonic expansions are given. Next, collision kinetics, guiding dynamics, Hund's cases and predissociation are discussed individually. Finally, the orientation effect and the theory of chemi-ionization are presented.

2.1 Production of supersonic beams

Pulsed supersonic beams are the starting point in the current experiment. Their generation and properties are described here because they provide dense packets of molecules that are translationally and rotationally cold. Pulsed atomic and molecular beams are generated by expanding a high-pressure gas from a reservoir into a vacuum through a nozzle. If the diameter of the expansion orifice is larger than the mean free path of the gas in the reservoir, particles go through many collisions when they escape from the reservoir. These collisions can cool the expanding gas particles because the thermal energy is converted into kinetic energy along the propagation path of the beam. As a result, a molecular supersonic jet is formed which is translationally and internally cold at the local speed, $a(z)$, but propagates at a high speed, $u(z)$, in the laboratory reference frame, as shown in Fig. 2.1.[79] When $u(z)/a(z) > 1$, we call it supersonic expansion.[80]

When a gas at high pressure p_0 in a reservoir at temperature T_0 expands into a low-pressure region along the z axis, the particle propagates and results in a final local pressure $p(z)$ and temperature $T(z)$. This expansion process is adiabatic, leading to the conservation of the total enthalpy H_0 of the system.[81] The total enthalpy is then converted into sum of the kinetic energy of the mass flow in the laboratory reference frame moving at speed $v(z)$ and the remaining enthalpy $H(z)$:

$$H_0 = H(z) + \frac{1}{2}nN_A m v^2(z) \quad (2.1)$$

where n , N_A and m are the number of moles in the beam, Avogadro's number, and the mass of

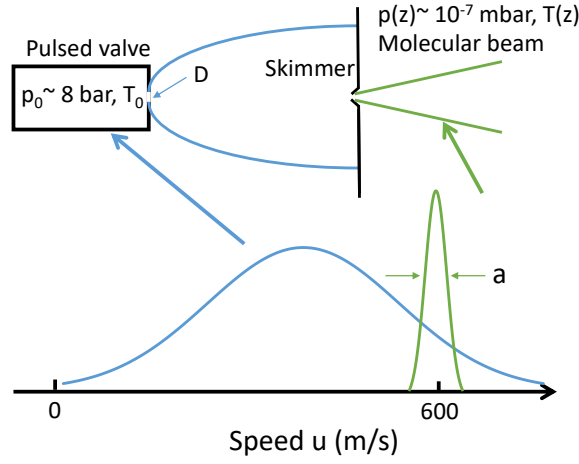


Figure 2.1 – Cooling effect that results in the adiabatic expansion through a pulsed valve (Here, metastable neon is at ≈ 170 K). On the left, neon gas is kept at a pressure of a few atmospheres. The blue curve shows its speed distribution in the lower plot. Once the orifice is opened, the gas expands through a nozzle and rapidly cools. The beam then is filtered by a skimmer shown in the green curve, which generates a beam pulse with a narrow velocity distribution by adiabatic cooling.

an individual gas particle, respectively. Its differential is

$$dH = nN_A c_p dT \quad (2.2)$$

where c_p is the constant-pressure molar heat capacity. The velocity at position z is

$$v^2(z) = \frac{2(H_0 - H(z))}{nN_A m} = 2 \int_{T(z)}^{T_0} \frac{c_p}{m} dT \quad (2.3)$$

We assume that c_p is independent of temperature, Eq. 2.3 can be rewritten as

$$v(z) = \sqrt{\frac{2c_p(T_0 - T(z))}{m}} \quad (2.4)$$

Next, the heat capacity ratio $\gamma = c_p/c_v$ is substituted into the $c_p = \frac{k_B \gamma}{(\gamma-1)}$, where c_v is the constant-volume molar heat capacity and k_B is the Boltzmann constant. If p_0 is large and the low-pressure region is vacuum, $T_0 \gg T(z)$, i.e., $T_0 - T(z) \approx T_0$, Eq. 2.4 becomes

$$v_{\max} = \sqrt{\frac{2k_B T_0}{m} \frac{\gamma}{\gamma-1}} \quad (2.5)$$

which is the largest possible velocity that may be obtained in the beam. For a collimated

supersonic beam, its velocity distribution is given in Ref. [82]:

$$f_n(v) = O_n v^n \exp\left[-\frac{(v - v_{\max})^2}{2\sigma_v^2}\right] \quad (2.6)$$

where O_n is a normalization constant and σ_v is the longitudinal velocity spread which is related to the final temperature $T(z)$ through $\sigma_v^2 = k_B T(z)/m$. In the case of $n = 2$, $f(v)$ corresponds to velocity distributions of the density and is for the flux density when $n = 3$. [82]

According to Eq. 2.5, the speed of a supersonic beam is proportional to the square root of the reservoir temperature. The speed of the beam can be easily adjusted by cooling or heating the gas reservoir. [83] Another accessible method to cover a wide range of speeds of the supersonic beam is to seed a small fraction of the target gas in a carrier gas, typically, a rare gas. [79, 84] Because the expansion dynamics in a seeded rare gas mix is mainly given by the major component of the mix, changing the mass of the rare gas can also be used to control final velocities of the beams. The detailed speed calculations of the carrier gas and target gas are given in Ref. [85].

2.2 Kinematics of crossed and merged beams

In order to manipulate collision energy in reactions, it is necessary to understand the kinematics of crossed and merged beams. Figure 2.2 illustrates an example of a crossed molecular beam apparatus which was first developed by Lee and Herschbach in 1968.[86] The total kinetic energy in this system is given by

$$E = E_1 + E_2 = \frac{m_1}{2} \vec{v}_1^2 + \frac{m_2}{2} \vec{v}_2^2 \quad (2.7)$$

Equation 2.7 can be separated into the kinetic energy of the center-of-mass E_{CM} and the collision energy E_{coll} ,

$$E = E_{\text{CM}} + E_{\text{coll}} = \frac{M}{2} \vec{v}_{\text{CM}}^2 + \frac{\mu}{2} \vec{v}_{\text{rel}}^2 \quad (2.8)$$

where $M = m_1 + m_2$ is the total mass, $\vec{v}_{\text{CM}} = \frac{m_1 \vec{v}_1 + m_2 \vec{v}_2}{M}$ is the velocity in the center of mass frame, $\mu = \frac{m_1 m_2}{m_1 + m_2}$ is the reduced mass and $\vec{v}_{\text{rel}} = \vec{v}_1 - \vec{v}_2$ is the relative velocity. Thus, the collision energy is given by

$$E_{\text{coll}} = \frac{\mu}{2} \vec{v}_{\text{rel}}^2 = \frac{\mu}{2} (\vec{v}_1 - \vec{v}_2)^2 = \frac{\mu}{2} (|\vec{v}_1|^2 + |\vec{v}_2|^2 - 2|\vec{v}_1||\vec{v}_2|\cos\theta) \quad (2.9)$$

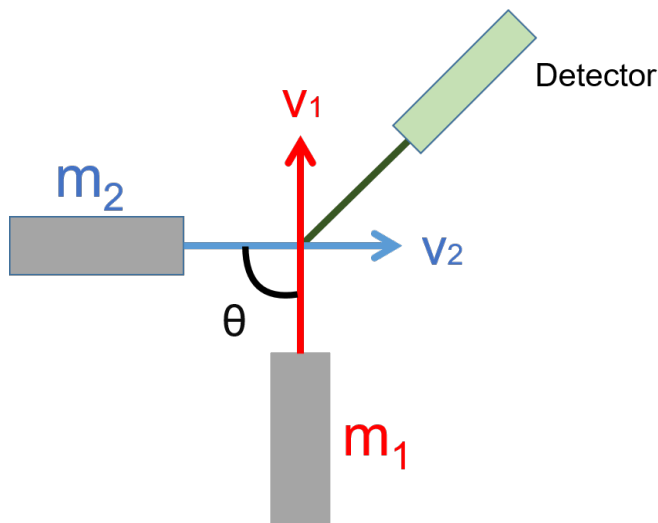


Figure 2.2 – Arrangement of a crossed molecular beam apparatus. In this frame, two molecular beams, whose mass of particles are m_1 and m_2 , propagate with velocities \vec{v}_1 and \vec{v}_2 , respectively. These two beams then cross at the center of a reaction zone at an angle θ . Products are collected by a rotatable detector.

where θ is the intersection angle between particles. In perfectly merged beams ($\theta = 0^\circ$), the collision energy only depends on the velocity difference of the reactants,

$$E_{\text{coll}} = \frac{\mu}{2} (|\vec{v}_1|^2 + |\vec{v}_2|^2 - 2|\vec{v}_1||\vec{v}_2|) = \frac{\mu}{2} (|\vec{v}_1| - |\vec{v}_2|)^2. \quad (2.10)$$

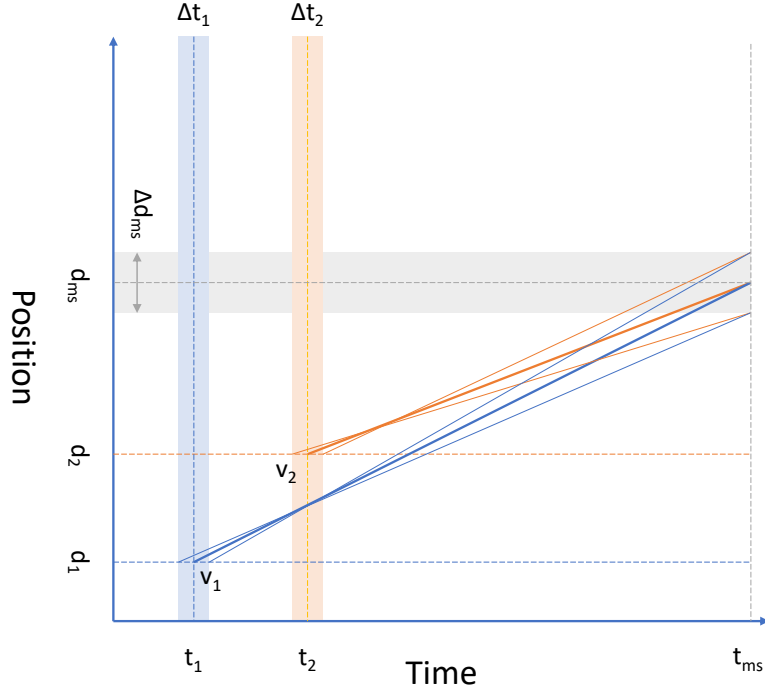


Figure 2.3 – Schematic diagram of the energy resolution using the time-sliced technique. (Adapted from Ref. [88])

Zero collision energy is obtained by setting the two velocities the same, i.e. $|\vec{v}_1| = |\vec{v}_2|$. However, the speed distributions in each of the beams are finite, displaying longitudinal and transverse divergences.[87] If we define the velocity spread as $\Delta v_i (i = 1, 2)$ for particle 1 or 2, the energy resolution can be determined using[84, 88]:

$$\Delta E_{\text{coll}} = \mu |v_1 - v_2| \sqrt{\Delta v_1^2 + \Delta v_2^2}. \quad (2.11)$$

In order to increase the energy resolution of the merged beam apparatus, a time-sliced detection, illustrated in Fig. 2.3, is introduced because it can reduce each $\Delta v_i (i = 1, 2)$ value as we have a detection method that is narrow in space and time.[87] Each molecular beam starts at the initial position $d_i (i = 1, 2)$ with a given average velocity $v_i (i = 1, 2)$ and each valve has a given opening time $\Delta t_i (i = 1, 2)$. After propagating a certain distance, these molecular beams collide at the position of a mass spectrometer (MS) d_{ms} and t_{ms} is the time when the TOF-MS is pulsed. The mean velocity v_i for each molecular pulse ($i = 1$ or 2) is

$$v_i = \frac{d_{\text{ms}} - d_i}{t_{\text{ms}} - t_i}. \quad (2.12)$$

In order to estimate the maximum velocity spread, the maximum and minimum velocities need to be calculated. In this case, the valve opening time $\Delta t_i (i = 1, 2)$ and the size of the

Chapter 2. Theoretical Concepts

detection area Δd_{ms} are taken into account, the maximum and minimum velocities in the detection region are:

$$v_{\text{imin}} = \frac{d_{\text{ms}} - d_i - \frac{1}{2}\Delta d_{\text{ms}}}{t_{\text{ms}} - t_i + \frac{1}{2}\Delta t_i} \quad (2.13)$$

$$v_{\text{imax}} = \frac{d_{\text{ms}} - d_i + \frac{1}{2}\Delta d_{\text{ms}}}{t_{\text{ms}} - t_i - \frac{1}{2}\Delta t_i} \quad (2.14)$$

Substitution of the v_{imin} and v_{imax} in the longitudinal velocity spread calculation gives the velocity spread at a given position:

$$\Delta v_i = v_{\text{imax}} - v_{\text{imin}} = \frac{(d_{\text{ms}} - d_i)\Delta t_i + (t_{\text{ms}} - t_i)\Delta d_{\text{ms}}}{(t_{\text{ms}} - t_i)^2 - \frac{1}{4}\Delta t_i^2} \quad (2.15)$$

If the valve opening time is significantly shorter than the flight time and the dimensions of the detection region are significantly smaller than the total flight distance, i.e., $\Delta t_i \ll (t_{\text{ms}} - t_i)$ and $\Delta d_{\text{ms}} \ll (d_{\text{ms}} - d_i)$, we can make the following approximation:

$$\Delta v_i \approx \frac{(d_{\text{ms}} - d_i)\Delta t_i + (t_{\text{ms}} - t_i)\Delta d_{\text{ms}}}{(t_{\text{ms}} - t_i)^2} = \frac{(d_{\text{ms}} - d_i)\Delta t_i}{(t_{\text{ms}} - t_i)^2} + \frac{\Delta d_{\text{ms}}}{(t_{\text{ms}} - t_i)} \approx \left(\frac{\Delta t_i}{t_{\text{F}}} \right) v_i \quad (2.16)$$

Considering the properties of the used sources as given in Table 3.1, the velocity spread is less than 3% of the beam velocity such that $v_{\text{Ne}^*} = 600$ m/s. The present beam sources combined with flight distances of $\approx 1\text{--}2$ m, provide Δv_{Ne^*} of around 10–20 m/s in the merged beam experiment.[89]

2.3 Manipulation of neutrals

To achieve the orientation control of paramagnetic atoms or polar molecules, it is essential to prepare a polarized sample. The term *polarized* describes a situation where the angular momentum \vec{J} is not randomly oriented. This property can also be reflected in an uneven population distribution over different quantum states M_J which is the projection of \vec{J} along the external field axis.[90]

The preparation of a polarized sample requires a good understanding of the energy level structure of the sample. When a particle is in an external electric or magnetic field, space quantization implies that its total angular momentum vector \vec{J} can only have certain orientations in space. The amplitude of the vector \vec{J} is $\hbar(J(J+1))^{1/2}$ and the projection of \vec{J} along the field direction is given by $\hbar M_J$ with $M_J = J, J-1, \dots, -J$. [49] The states with different quantum numbers M_J have different energies and these M_J -dependent energies need to be calculated.

Zeeman effect

When a paramagnetic particle is in a magnetic field, its total Hamiltonian is[91]

$$H = H_0 + V_M \quad (2.17)$$

where H_0 is the unperturbed Hamiltonian and the Zeeman Hamiltonian V_M is the perturbation by the field:

$$V_M = -\vec{\mu}^B \cdot \vec{B}. \quad (2.18)$$

$\vec{\mu}^B$ is the magnetic moment which involves the contributions of the angular momentum and the spin of the electrons (here we neglect the nuclear spin interaction), i.e.,

$$\vec{\mu}^B = -\frac{\mu_B(g_L\vec{L} + g_S\vec{S})}{\hbar} \quad (2.19)$$

where μ_B is the Bohr magneton, g_L is the orbital g -factor and g_S is the electron spin g -factor, \vec{L} is the orbital angular momentum and \vec{S} is the spin angular momentum. As $g_L = 1$ and $g_S = 2$, Eq. 2.18 becomes

$$V_M = \frac{\mu_B}{\hbar}(\vec{L} + 2\vec{S}) \cdot \vec{B}. \quad (2.20)$$

The total angular momentum of an atom can be described in Russell-Saunders coupling, where \vec{L} and \vec{S} are not conserved but the total angular momentum $\vec{J} = \vec{L} + \vec{S}$ is. The spin and angular momentum vectors precess about the fixed total angular momentum \vec{J} . The corresponding

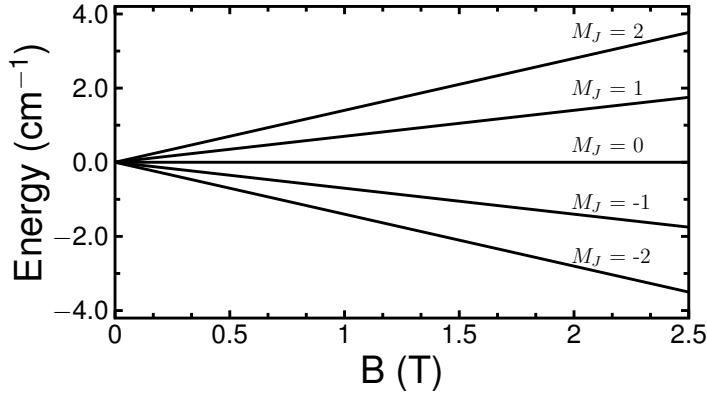


Figure 2.4 – Zeeman effect of metastable neon in 3P_2 state.

(time) average value for \vec{L} or \vec{S} is its projection along \vec{J} :

$$\vec{S}_{\text{avg}} = \frac{\langle \vec{S} \cdot \vec{J} \rangle}{|\vec{J}|^2} \vec{J} \quad (2.21)$$

$$\vec{L}_{\text{avg}} = \frac{\langle \vec{L} \cdot \vec{J} \rangle}{|\vec{J}|^2} \vec{J} \quad (2.22)$$

Therefore,

$$V_M = \frac{\langle \vec{L} \cdot \vec{J} \rangle + 2\langle \vec{S} \cdot \vec{J} \rangle}{|\vec{J}|^2} \frac{\mu_B \vec{J} \cdot \vec{B}}{\hbar}. \quad (2.23)$$

The Zeeman correction to the energy V_M can be written as

$$E_M = \mu_B B M_J g_J \quad (2.24)$$

where B is the scalar of the magnetic field \vec{B} , M_J is the eigenvalue of an angular momentum operator \vec{J}_z and g_J is the Lande g -factor expressed as $g_J = \frac{\langle \vec{L} \cdot \vec{J} \rangle + 2\langle \vec{S} \cdot \vec{J} \rangle}{2J(J+1)}$. Using $\vec{J} = \vec{L} + \vec{S}$, we get

$$g_J = \frac{3}{2} + \frac{S(S+1) - L(L+1)}{2J(J+1)} \quad (2.25)$$

Table 2.1 – Strength of the magnetic moments for metastable neon in the $^3P_{0,1,2}$ states

state	g_J	M_J	V_M
3P_2	$\frac{3}{2}$	2	$3\mu_B B$
		1	$\frac{3}{2}\mu_B B$
		0	0
3P_1	$\frac{3}{2}$	1	$\frac{3}{2}\mu_B B$
		0	0
3P_0	-	0	0

As can be seen in Eq. 2.24, in a magnetic guide the particles experience a different force which is dependent on the M_J components. The radial force of an ideal magnetic hexapole is given in terms of the magnetic field gradient by[49]

$$F(r) = -\nabla E_M = -g_J \mu_B M_J \frac{\partial B(r)}{\partial r} \quad (2.26)$$

where the radial magnetic field magnitude $B(r)$ can be calculated by the following expression:

$$B(r) = B_r \left(\frac{r}{r_0}\right)^2. \quad (2.27)$$

B_r is a constant, r is the distance from the center of the magnetic hexapole element, and r_0 is the inner radius of the hexapole guide. As can be seen in Eq. 2.26, the hexapole applies a restoring force that depends not only on the M_J value but also on the sign of M_J .

Zeeman effect of $\text{Ne}(^3P_2)$

When the neon atom is in its ground state, it has no permanent magnetic moment. It will change if neon is excited to the first excited state, i.e., a $2p$ electron is excited into the $3s$ orbital, which leads to four spin-orbit states that are denoted as 1P_1 , 3P_2 , 3P_1 , 3P_0 . The transition between the excited state $^3P_{2,0}$ and the ground state requires a change in total angular momentum of either $\Delta J = 2$ or $\Delta J = 0$ for $J = 0 \leftrightarrow 0$, which is not allowed in an electric dipole transition and their lifetimes are relatively long. $\text{Ne}(^3P_2)$ here is paramagnetic and it is possible to control the populations of states differing only by the magnetic quantum number M_J . Magnetic moments for different excited neon atoms are given in Table 2.1.

Stark effect

Under the influence of an external electric field, the splitting and shifting of spectral lines of atoms or molecules is called the Stark effect. It is analogous to the Zeeman effect.[49] For a polar molecule, Stark shift arises from the interaction between the electric dipole moment, $\vec{\mu}$ and the external electric field \vec{E} . The interaction can be written by an additional term in the Hamiltonian:

$$H = H_0 - \vec{\mu} \cdot \vec{E} \quad (2.28)$$

where H_0 is the unperturbed rotational Hamiltonian and the perturbation $W_s = -\vec{\mu} \cdot \vec{E}$ is due to the Stark effect.

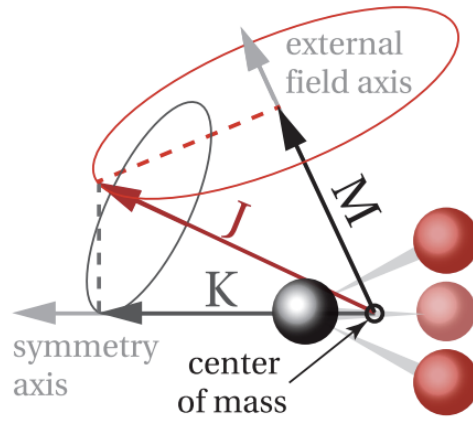


Figure 2.5 – Rotational quantum numbers of a polar molecule in space. (Reproduced from Ref. [88])

Here we take ammonia as an example which is a symmetric top molecule. Its component of the permanent dipole moment along the axis of the electric field, $\vec{\mu}_E$ can be derived from the projection of the permanent dipole moment $\vec{\mu}$ onto symmetry axis, $\vec{\mu}_K$ as shown in Fig. 2.5:

$$\vec{\mu}_K = \vec{\mu} \frac{K}{\sqrt{J(J+1)}}, \quad (2.29)$$

$$\vec{\mu}_E = \vec{\mu}_K \frac{M}{\sqrt{J(J+1)}} \quad (2.30)$$

where K is the projection of \vec{J} on the symmetry axis and M is the projection of \vec{J} on the external field axis as shown in Fig. 2.5. Using perturbation theory, the first-order corrected energy levels of ammonia can be calculated:

$$E_s = -\frac{MK}{J(J+1)} \mu E. \quad (2.31)$$

This equation indicates that the ammonia molecule in the $|J, K\rangle$ state can split up $(2J+1)M$ components in an external electric field. As we can see in Fig. 2.6, all the components can be split into two groups, i.e., the behavior of the $MK = 0$ and $MK \neq 0$ under the electric field. Depending on the orientation of the dipole moment relative to the electric field, the polar

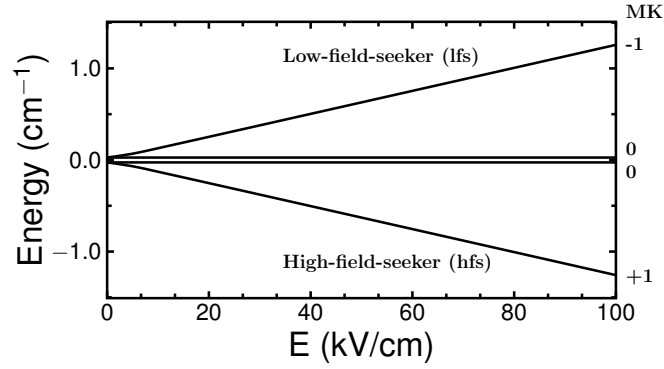


Figure 2.6 – First order Stark shift of ND_3 in the $J_K = 1_1$ state in electric fields. States are labeled as $|J, MK\rangle$.

particle can either gain or lose energy in the electric field, which is classified as a lfs if the particle is attracted by low field regions and a hfs if the particle moves towards higher fields. At zero field, we can observe that the ammonia molecule has an inversion splitting W_{inv} in the ground state. Both components of the inversion splitting have opposite parities and they can be coupled in the Hamiltonian of the Stark effect.[92] Therefore, the first order approximation of the Stark shift of the ammonia molecule is given by

$$E_s = \pm \sqrt{\left(\frac{W_{\text{inv}}}{2}\right)^2 + \left(\frac{MK}{J(J+1)}\mu E\right)^2} \mp \left(\frac{W_{\text{inv}}}{2}\right) \quad (2.32)$$

For example, the inversion splitting W_{inv} is 0.053 cm^{-1} for ND_3 . [93] As Eq. 2.32 shows, the Stark shift is linear when the inversion splitting can be neglected relative to the second term in the square root. In the case of ND_3 , the two terms are equal at $E = 1046 \text{ V/cm}$. At field strengths considerably above this value, the Stark shift increases almost linearly while below it, the dependence is near-quadratic. This transition happens at much lower field in a molecule like ND_3 (with a small zero-field splitting) than its hydrogenated counterpart, NH_3 , where the inversion splitting is 0.79 cm^{-1} . [94] In analogy with the Zeeman effect described above, the Stark effect can be used to exert a force on polar molecules if the gradient of the electric field is non-zero. Indeed, the Stark force can be written as $F_s = -\nabla E_s$ which permits to guide, state-select, and polarize polar molecules in an equivalent fashion as for paramagnetic particles in the presence of a Zeeman force.

2.4 Coupling and predissociation

Hund's cases

For the diatomic system $\text{Ne}^* + \text{X}$ ($\text{X} = \text{Ar}, \text{Kr}, \text{Xe}$), its coupling in reactions can be confined in a specific order of Hund's cases that are the scheme of total angular momentum coupling or de-coupling within the inter-particle electric field.[95]

In these couplings, there are three angular momenta (neglecting nuclear spin): electronic orbital angular momentum \vec{L} , electronic spin angular momentum \vec{S} , and nuclear rotation angular momentum \vec{R} . These momenta will couple together to the total angular momentum \vec{J} . According to the relative strengths of three basic interactions (interaction of an electrostatic nature, spin-orbit interaction of a magnetic nature and rotational or the Coriolis interaction), Hund's cases can be classified into five types whose patterns correspond to all possible hierarchies of the 'strong-intermediate-weak' type among these interactions. The detail is given in Table 2.2.

Table 2.2 – Hund's coupling cases

Hund's case	Electrostatic	Spin-orbit	Rotational
a	strong	intermediate	weak
b	strong	weak	intermediate
c	intermediate	strong	weak
d	intermediate	weak	strong
e	weak	intermediate	strong
		strong	intermediate

To describe the bare Ne^* atom in a magnetic field we defined M_J as the projection of \vec{J} on the magnetic field axis \vec{B} . In the diatomic system $\text{Ne}^* + \text{X}$, M_J is not a good quantum number but instead we must consider molecular coupling cases as introduced here. Here, when the interparticle distance is short, we use Hund's case (c) where the total spin and total electron angular momenta couple to form the total angular momentum \vec{J} (neglecting nuclear spin and molecular rotation). In this coupling case, sketched in Fig. 2.7, the projection of \vec{J} on the interatomic axis, called Ω , is also a conserved quantity, and is thus used to describe the proper coupling state in the current reactions. As will be shown before, the populations of states labeled by Ω can be obtained from the M_J specific populations through a frame rotation.

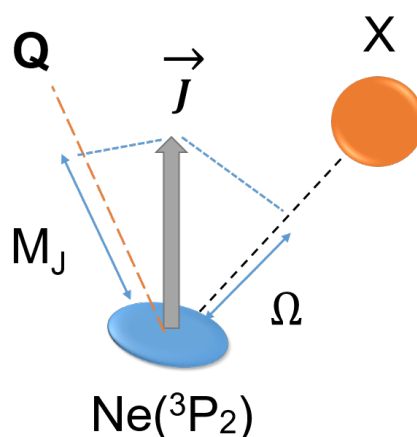


Figure 2.7 – Schematic diagram of the angular momentum \vec{J} in the laboratory reference frame Q and in the molecular frame whose projections are M_J and Ω respectively.

Predissociation

Predissociation is a process that can be observed when a molecule resides in a state that lies above some dissociation threshold.[96] In such a situation, appropriate coupling of the bound energy level to the continuum can lead to dissociation, either by vibrational energy transfer or through electronic coupling. Predissociation is a non-radiative process that has been observed in van der Waals complexes such as HF-Ar,[97] Cl₂-Ne.[98] The properties of these molecules have also been characterized including dissociative lifetimes and final rotational distributions of predissociation.[99] These studies become a reference when we investigate chemi-ionization reactions.

In the $\text{Ne}^* + \text{X}$ ($\text{X} = \text{CO}$ and N_2) reactions, if the intermediate complex $[\text{NeX}]^+$ is in the vibrational ground state with a long dissociation lifetime so that we can observe the associative ion in the products.[28] However, when the internal energy of the excited $[\text{NeX}]^+$ complex is larger than its binding energy, e.g. when the X^+ in the complex has vibrational excitation, the complex will release its internal energy from the decay and result in the bond breaking:[23]



where ΔE is the accessible energy which usually is much larger than the binding energy of $[\text{NeX}]^+$. The detailed description of predissociation will be presented in Chapter 5.

2.5 Orientation effect

In a chemical reaction, we consider not only its scalar properties such as how the rate of reaction depends on the energies of the reagents but also its vector properties e.g. velocities and angular momenta.[90] Only by understanding the scalar and vector properties, we can obtain the full picture of the reaction dynamics for this reaction. In this section, we concentrate on the rotational angular momentum \vec{J} of the reactants and describe angular momentum polarization in terms of alignment and orientation.

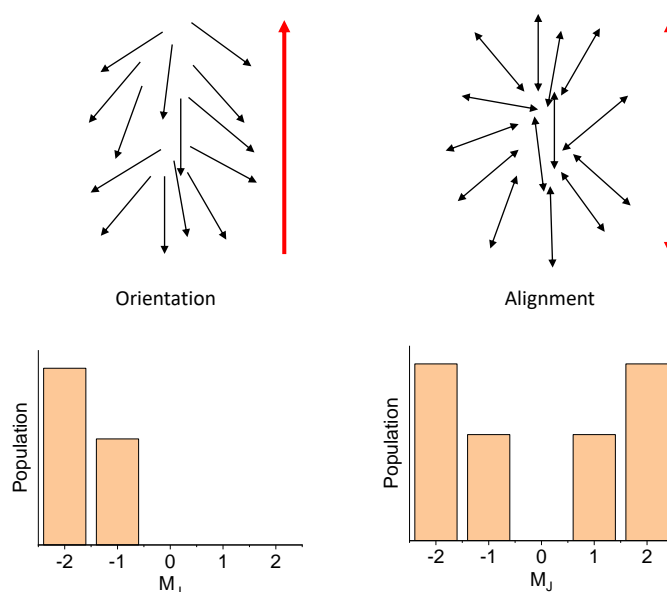


Figure 2.8 – Schematic showing the potential direction of the angular momentum vectors \vec{J} with a reference axis (shown in red) for an oriented sample and an aligned sample. The corresponding M_J distributions, arising from the projection of the molecular angular momentum vector \vec{J} upon a symmetry axis z for an oriented sample and an aligned sample.

Here we use simple examples to describe the qualitative meaning of orientation and alignment as shown in Fig. 2.8. Two ensembles of single-headed, double-headed arrows are given where their directions are anisotropically distributed. The single-headed arrows have a direction toward the bottom of the page and it can be referred to as orientation, while double-headed arrows have no directionality, in other words, they point toward the top and bottom of the page. When the direction of these arrows is preferentially along a certain axis we define this as an aligned sample. Because the arrows are double-headed there is no preference of direction in the case of alignment. If these arrows are thought to be rotational angular momentum vectors \vec{J} , we find that an oriented sample has a preferred direction for \vec{J} while we can only distinguish \vec{J} of an aligned sample whether they are pointing parallel or anti-parallel directions with respect to a given laboratory reference frame.

In order to describe the distribution of angular momentum vectors about a given reference axis,

alignment parameters are introduced here which are related to the populations of different M_J states. As can be seen, M_J for an oriented sample will be entirely negative or positive because of the fixed direction of \vec{J} on the reference axis, while M_J can have both positive and negative values for an aligned sample. These alignment parameters $A_q^{(k)}(J)$ of order k and component q are also related to the density matrix elements $\rho_{M'_J, M_J}$:

$$A_q^{(k)}(J) = \frac{c(k)}{[J(J+1)]^{k/2}} \sum_{M'_J, M_J} \rho_{M'_J, M_J} \langle JM_J | J_q^{(k)} | JM'_J \rangle \quad (2.34)$$

where $c(k)$ is a normalization factor, q is the component of k ($q = 0$ for cylindrical symmetry, otherwise, $-k \leq q \leq k$) and $J_q^{(k)}$ is the spherical-tensor angular momentum operator.[90] In our case, $q = 0$ so that the normalization factors $c(k)$ are

$$c(0) = 1, c(1) = 1, c(2) = \sqrt{6}, c(3) = \sqrt{5/2} \text{ and } c(4) = \sqrt{35/8}. \quad (2.35)$$

When $M'_J = M_J$ and $J' = J$, the matrix in Eq. 2.34 can be written as

$$\sum_{M_J, M_J} \rho_{M_J, M_J} \langle JM_J | J_q^{(k)} | JM_J \rangle = \sum_{M_J} \rho_{M_J, M_J} (-1)^{J-M_J} \begin{pmatrix} J & k & J \\ -M_J & q & M_J \end{pmatrix} \langle J || J^{(k)} || J \rangle \quad (2.36)$$

where the reduced matrix elements $\langle J || J^{(k)} || J \rangle$ are given in Ref. [100]. Once we obtain the density matrix elements $\rho_{M'_J, M_J}$, we can write its diagonal elements as fractional populations of $|J, M_J\rangle$ states, $p_{M_J} = \rho_{M_J, M_J}$.

2.6 Numerical methods in chemi-ionizations

In this section, we present the numerical methods that are used in the calculation of the PI (Penning ionization) and AI (associative ionization) cross sections in the $\text{Ne}^* + \text{Ar}$ reaction. The basic formulae for these purposes are given in Refs. [23, 101, 102] which gives the scattering amplitude for AI and PI based on O'Malley's theory of dissociative attachment. [103, 104].

Before the collision, \vec{k} is defined as the internuclear momentum vector with magnitude k and direction \hat{k} . After the collision, the magnitude of \vec{k} changes into k_f along the direction \hat{k}_f . Meanwhile, the Penning electron obtains energy ϵ along the \hat{k}_ϵ . In the scattering process, the energy conservation principle is used:

$$E_{\text{coll}} + \text{IE} = E_+ + \text{IP} + \epsilon, \quad (2.37)$$

where $E_{\text{coll}} = \frac{k^2 \hbar^2}{2\mu}$ is the initial kinetic energy, μ is the reduced mass, $E_+ = \frac{k_f^2 \hbar^2}{2\mu}$ is the kinetic energy of the atoms in the final channel, IE is the excitation energy of Ne^* atoms, and IP is the ionization energy of Ar in the ground state. To obtain the scattering cross sections, it is necessary to calculate the scattering amplitude whose expression is given by [105]:

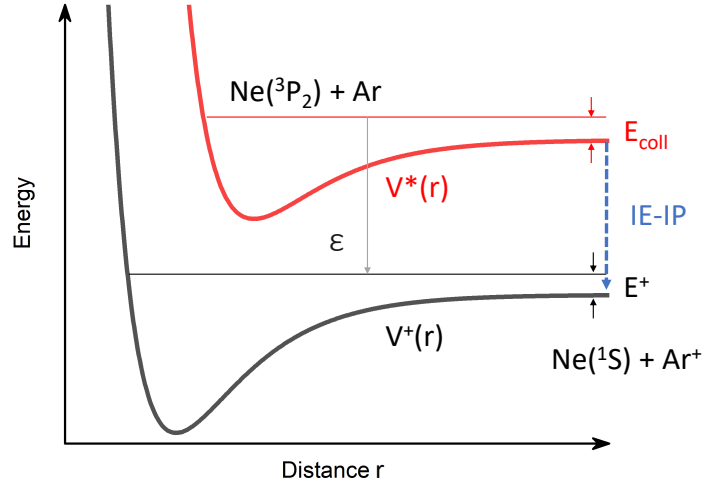
$$f(\hat{k}_f, \epsilon, \hat{k}_\epsilon; \vec{k}) = -\frac{2\mu\rho_\epsilon^{1/2}}{(4\pi\hbar)^2} \left(\frac{k_f}{k}\right)^{1/2} \langle \psi_\epsilon | V_{\epsilon, \hat{k}_\epsilon} | \psi_d \rangle \quad (2.38)$$

where $V_{\epsilon, \hat{k}_\epsilon}$ is the probability amplitude for the emission of an electron with ϵ and \hat{k}_ϵ , ρ_ϵ is the density of electronic continuum states. ψ_d is the incoming wave function calculated on the optical potential $V_*(r) - \frac{i}{2}\Gamma(r)$ of the $\text{Ne}^* + \text{Ar}$ curves and ψ_ϵ is the wave function on the exit channel $V_+(r)$. The $V_+(r)$ describes the bound and continuum states of the ionic $\text{Ne}(^1\text{S}) + \text{Ar}^+$ curves as shown in Fig. 2.9.

The optical potential in $\text{Ne}^* + \text{Ar}$ reaction is written as $V_{\text{opt}, \Omega \rightarrow X}(r) = V_*(r) - \frac{i}{2}\Gamma_{\Omega \rightarrow X}(r)$. $\Gamma_{\Omega \rightarrow X}(r)$ provides the ionization rate from the initial state (characterized by Ω which is the projection of J on the inter-particle axis) to the exit channel X , which results in either AI or PI product ions. Here, we approximate $\Gamma_{\Omega \rightarrow X} = \Gamma_\Omega W_{\Omega \rightarrow X}$ where the autoionization for a given Ω , $\Gamma_\Omega(r)$, is taken from Ref. [106]. In addition, the branching ratio $W_{\Omega \rightarrow X}$ from the Ω state to the channel X is obtained from Ref. [102] although the model is limited to the early semi-imperial energy surfaces in early-stage experiments. The real part $V_*(r)$ for all Ω states are given in Ref. [107] and the outgoing potential curves $V_+(r)$ include three possible molecular channels: $X^2\Sigma_{1/2}$, $A_1^2\Pi_{3/2}$ and $A_2^2\Pi_{1/2}$. [108]

In the scattering amplitude calculation, the incoming wave function $\psi_d(\vec{r})$ can be written in terms of spherical harmonics $Y_{J, m}$:

$$\psi_d(\vec{r}) = 4\pi \sum_{J_*=0}^{\infty} \sum_{m=-J_*}^{J_*} i^{J_*} e^{i\delta^{J_*}} \frac{\psi_d^{J_*}(r)}{k^{1/2} r} Y_{J_*, m}^*(\hat{k}) Y_{J_*, m}(\hat{r}) \quad (2.39)$$


 Figure 2.9 – Schematic view of the potential curves in the $\text{Ne}^* + \text{Ar}$ reaction.

where m is the magnetic quantum number, \hat{r} is the relative position of the atoms, J_* is the angular momentum of the complex and δ^{J_*} is the complex phase shift that accounts for the loss of flux because of ionization. The reduced wave function $\psi_d^{J_*}(r)$ is computed by solving the following Schrödinger equation

$$\left(-\frac{\hbar^2}{2\mu} \frac{d^2}{dr^2} + V_{\text{opt}}(r) + \frac{\hbar^2 J_*(J_* + 1)}{2\mu r^2} - E_{\text{coll}} \right) \psi_d^{J_*}(r) = 0, \quad (2.40)$$

When the distance between the atoms becomes infinitely large, the expression of $\psi_d^{J_*}(r)$ becomes

$$\psi_d^{J_*}(r) \xrightarrow{r \rightarrow \infty} k^{-1/2} \sin(kr - \pi J_*/2 + \delta^{J_*}) \quad (2.41)$$

where the phase shift δ^{J_*} can be computed as described in Ref. [109].

The final continuum state $\psi_\epsilon(\vec{r})$ of the $\text{Ne}(^1\text{S}) + \text{Ar}^+$ wave function is written as

$$\psi_\epsilon(\vec{r}) = 4\pi \sum_{J_+=0}^{\infty} \sum_{m'=-J_+}^{J_+} i^{J_+} e^{-i\delta_f^{J_+}} \frac{\psi_{\epsilon/v}^{J_+}(r)}{k_f^{1/2} r} Y_{J_+ m'}^*(\hat{k}) Y_{J_+ m'}(\hat{r}) \quad (2.42)$$

in which J_+ is the angular momentum of the ion fragment and $\delta_f^{J_+}$ is the real phase shift. We label with ϵ the PI case ($E_+ > 0$) and with v the vibrational (bound) states corresponding to AI ($E_+ < 0$).

Chapter 2. Theoretical Concepts

The reduced wave function $\psi_{\varepsilon/v}^{J_+}(r)$ is used in the equation

$$\left(-\frac{\hbar^2}{2\mu} \frac{d^2}{dr^2} + V_+(r) + \frac{\hbar^2}{2\mu} \frac{J_+(J_+ + 1)}{r^2} - E_+ \right) \psi_{\varepsilon/v}^{J_+}(r) = 0. \quad (2.43)$$

The asymptotic behavior of the PI/AI scattering state is

$$\psi_{\varepsilon/v}^{J_+}(r) \xrightarrow{r \rightarrow \infty} k_f^{-1/2} \sin(k_f r - \pi J_+/2 + \delta_f^{J_+}) \quad (2.44)$$

The final bound states $\psi_{\varepsilon/v}(r)$ of the exit channels are calculated by diagonalizing the Hamiltonian in the exit channels.[110]

Taking everything into account, and considering that we have an incoherent mixture, the scattering amplitudes for the decay from the entrance channel Ω to the exit channel X in the Born-Oppenheimer approximation are written as

$$f_{X,\Omega}(\hat{k}_f, \varepsilon, \hat{k}_\varepsilon; \vec{k}) = \frac{\sqrt{\pi}}{ik} \sum_{\ell, m, J_*, J_+} i^{J_* - J_+} [(2J_* + 1)(2J_+ + 1)]^{1/2} \begin{pmatrix} J_+ & \ell & J_* \\ 0 & 0 & 0 \end{pmatrix} \times \\ \begin{pmatrix} J_+ & \ell & J_* \\ -m & m & 0 \end{pmatrix} S_{J_+, \ell}^{J_*, \Omega}(X, \varepsilon) Y_{J_+ - m}(\hat{k}_f) Y_{\ell m}(\hat{k}_\varepsilon), \quad (2.45)$$

The cross section for each reaction channel is given by $\sigma_X^\Omega(\hat{k}_f, \varepsilon, \hat{k}_\varepsilon; \vec{k}) = |f_{X,\Omega}(\hat{k}_f, \varepsilon, \hat{k}_\varepsilon; \vec{k})|^2$. [105] By using Eq. 2.45 and integrating over the final angles of the ejected electron and the final relative momentum of the atoms, we can obtain

$$\sigma_{\text{AI;PI}}^\Omega(\varepsilon) = \frac{\pi}{k^2} \sum_{\ell, J_*, J_+} (2J_+ + 1)(2J_* + 1) \left(\begin{pmatrix} J_+ & \ell & J_* \\ 0 & 0 & 0 \end{pmatrix} \right)^2 |S_{J_+, \ell}^{J_*, \Omega}(X, \varepsilon)|^2 \quad (2.46)$$

where the scattering matrices are given in terms of different phase shifts δ^{J_*/J_+}

$$S_{J_+, \ell}^{J_*, \Omega}(X, \varepsilon) = -2i \frac{2\mu \rho_\varepsilon^{1/2}}{\hbar^2} e^{i(\delta^{J_*} + \delta_f^{J_+})} \langle \psi_\varepsilon^{J_+} | V_{\varepsilon \ell} | \psi_d^{J_*} \rangle, \quad (2.47)$$

for the PI and

$$S_{J_+, \ell}^{J_*, \Omega}(X, \varepsilon) = -2i \left(\frac{2\mu \rho_\varepsilon}{\hbar^2} \right)^{1/2} e^{i\delta^{J_*}} \langle \psi_v^{J_+} | V_{\varepsilon \ell} | \psi_d^{J_*} \rangle, \quad (2.48)$$

for the AI[23].

3 Experimental apparatus and analysis

This chapter presents the experimental apparatus used for the stereodynamics investigations performed herein. The experimental setup contains different components: molecular sources, a time-of-flight MS (TOF-MS), a magnetic hexapole and an orienting field generator. In addition, REMPI spectroscopy and the fitting method for branching ratio are presented.

3.1 Experimental apparatus

Figure 3.1 shows a schematic of the experimental apparatus used for the crossed- and merged-beam experiments. The merged beam method utilizes the Zeeman effect to bend the path of a reactant on the same axis of another one. The original merged-beam apparatus was designed and constructed by Bertsche and Osterwalder.[88, 89] The original setup is then modified to the current version which contains four essential components:

- Three supersonic beams.
- A curved magnetic hexapole guide.
- A TOF-MS.
- Two pairs of solenoid magnets.

The experiment starts from a velocity-tuned metastable neon beam (3P_J , $J = 0, 1, 2$) whose detail is given in subsection 3.1.1. The beam is then skimmed and enters a 1.8 m curved magnetic hexapole. The purpose of the hexapole is to polarize an atomic ensemble as a state selector and to guide a paramagnetic beam to the reaction zone. The detailed description of the hexapole design is given in subsection 3.1.2. After the curved hexapole, the polarized beam propagates freely and then collides another ground-state reactant at 90° or 0° in the center of the reaction zone under a controllable magnetic field which is generated by two pairs of solenoid magnets. The magnetic field is used to adiabatically reorient the polarized beam (here is Ne^*) and the detailed component design and calibration of the magnets are described in subsection 3.1.3. Product ions are extracted and detected using a pulsed TOF-MS.

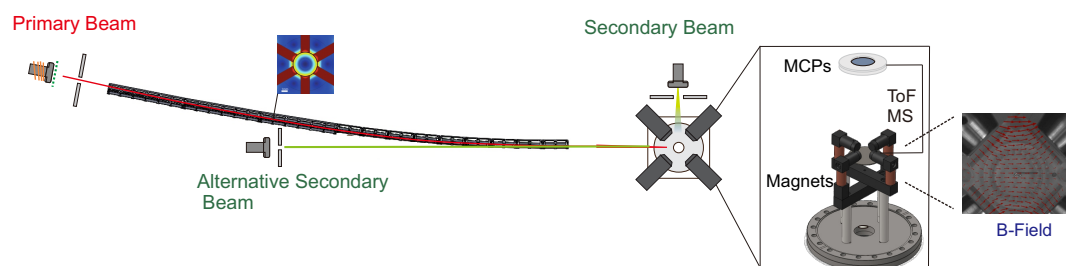


Figure 3.1 – Reactions occur in a tunable magnetic field created by a pair of solenoid magnets. B fields, TOF-MS and MCP are the abbreviations of magnetic fields, time-of-flight mass spectrometer, and microchannel plates, respectively.

The design of MS is given in subsection 3.1.4.

3.1.1 Atomic/molecular beams

Two types of supersonic molecular valves are utilized and the properties of the atom/molecular sources are listed in Table 3.1.

Table 3.1 – Properties of the supersonic valves.

Source	Type	Gas X	X:He ratio	backing pressure	velocity range
Primary beam	Even-Lavie	Ne	Pure	8 bar	530-760 m/s
Secondary beam	General valve	Ar	Pure	1 bar	558 ± 55 m/s
		Kr		1 bar	386 ± 38 m/s
		Xe		1 bar	308 ± 30 m/s
		N ₂		2 bar	667 ± 66 m/s
Alternative second beam	Even-Laive	N ₂	10:1–1:30	4 bar	750 m/s–1700 m/s
		CO	10:1–1:30	3 bar	750 m/s–1700 m/s
		Ar	Pure-1:30	10 bar	680 m/s–1500ms

For a metastable neon beam, we use an Even-Lavie valve with a dielectric barrier discharge (DBD).[111] The pulse duration is set to 15–20 μ s and the valve is operated with a backing pressure of 8 bar. By cooling the valve with cold N₂ gas and then heating with an electric coil, the valve body temperature can be tuned in the range of 150–300 K, providing the central speed of Ne* from 530 m/s to 760 m/s in the collision region. The error of the controlled temperature of the valve is smaller than 0.1 K.

In the crossed beam experiment, a Parker general valve (series 9) is operated at room temperature (~ 300 K) and its backing pressure is low (≈ 1 bar) with the purpose of avoiding possible condensation and clustering of the molecules. The beam is skimmed and enters the interaction zone without further modification.

In merged beams, the secondary beam is generated by an Even-Laive valve and its velocity is controlled by the seed ratios between rare gases and molecules at room temperature (~ 300 K). Here we also measured the delay (68.7 μ s) between the opening time of the valve and the input trigger pulse in terms of the trigger pulse used in the energy resolution calculation. Given the accessible speeds of the two reactants and the masses of the reactants involved in the present studies we can access ranges of collision energies E_{coll}/k_B from 20 mK–1000 K.

3.1.2 Magnetic hexapole

A 1.8 m curved magnetic hexapole guide, as shown in Fig. 3.1, is used to polarize and guide paramagnetic particles in the experiment. The magnetic field inside the guide is generated by permanent NdFeB magnets (grade N35, nickel coated) with a remanent magnetization $B_r \approx 1.17$ T. The guide has two parts: the first part close to the source has a symmetric hexapole configuration (inner diameter = 8 mm) as can be seen in Fig. 3.2 (b). The first part is made by three 30 cm long straight segments, each of which is tilted by one degree in the horizontal plane with respect to the previous one. The second part is for merging two molecular beams as shown in Fig. 3.2 (c). Its geometry is different from the first part and it consists of 10 segments. Each segment is 100 mm long and titled by one degree with respect to the previous one. Although two magnets at the outside bend are removed, the magnetic field in the guide is still sufficiently strong to keep the paramagnetic particles inside the guide.[88]

According to Eq. 2.26, a restoring force in the guide acts on a metastable neon beam in different M_J states depending not only on the sign of the M_J state but also on its value. If the particle is in a higher M_J state, it is subjected to a stronger force. This force is used to polarize an atomic ensemble and works as a state selector. This is because of the excited neon atoms ($^3P_{0,1,2}$, 1P_1) formed in the primary expansion, only those in the 3P_2 state are long-lived (14.73 s)[112] and can be guided to the interaction zone; 3P_1 and 1P_1 , have short lifetimes because the particles in these two states are mixed and the decay $^1P_1 \rightarrow ^1S$ is via a dipole transition; and 3P_0 is not paramagnetic, although its lifetime is relatively long (430 s).[113]

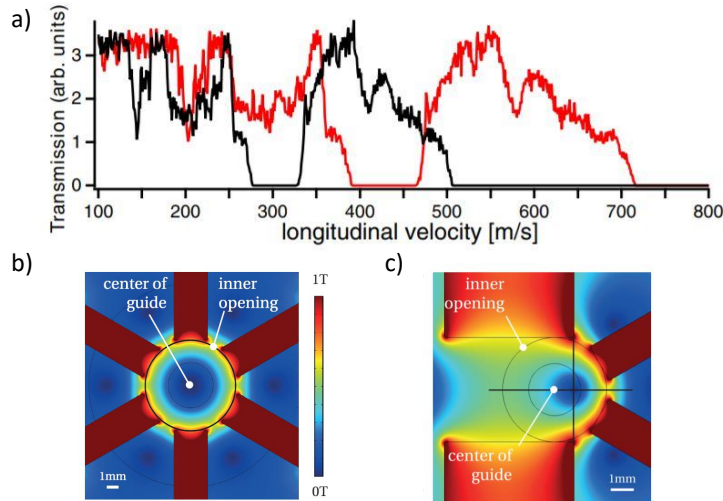


Figure 3.2 – (a) Calculated transmission curves for Ne* in the $M_J = 1$ (black line) and $M_J = 2$ (red line) states, respectively.(reproduced from Ref. [89]) The magnetic field strengths in the two parts of the hexapole: (b) the hexagonal part and (c) the merging part. The black circle is the inner opening. (reproduced from Ref. [88])

Figure 3.2 (a) shows the calculated transmission profile for Ne* through the guide used in

the present experiment. In these calculations the initial velocity distribution was chosen to be very broad enough to cover the entire transverse acceptance, and a flat distribution of the longitudinal velocity was used. The black and red traces show the results for $M_J = 1$ and 2, respectively. A local reduction in the transmission to zero is found in each trace which is known as stop bands. It is because unexpected dynamics at the points where segments are joined may alter the velocity-dependent transmission substantially.[114] In our case, this is a result of the small gaps between adjacent elements of the permanent magnet guides, and the velocity range is shifted between the red and black trace because of the different magnetic moments.

In the current experiment, the central speed of Ne^* is in the range of 530–760 m/s, indicating that only Ne^* atoms in the $M_J = 2$ state can pass through the guide. In fact, Ne^* atoms in the $M_J = 1$ state were also found when the beam emerged from the magnetic guide, which is because the precise state in which the particles leave the guide is neither sufficiently well-defined nor is there sufficient information on its evolution behind the guide.[115]

3.1.3 Orienting fields

The utilization of the Zeeman effect allows us to prepare a polarized sample emerging from the guide. It is important to note that the paramagnetic particles in the guide are not oriented because the field direction rotates in the plane perpendicular to the guide axis. In other words, the quantization axis of the guide is only defined locally, not macroscopically. In order to turn the polarized sample into an oriented sample, we must fully control the quantization axis. As Ne^* is paramagnetic, an orienting magnetic field is the choice to manipulate the quantization axis. Here two clamp-shaped magnetic steel structures equipped with two solenoids are used as shown in Fig. 3.3 (a). By applying currents up to 10 A through these solenoids, a magnetic field of ≈ 10 mT is generated. These two solenoid magnets are oriented at 90° with respect to each other.

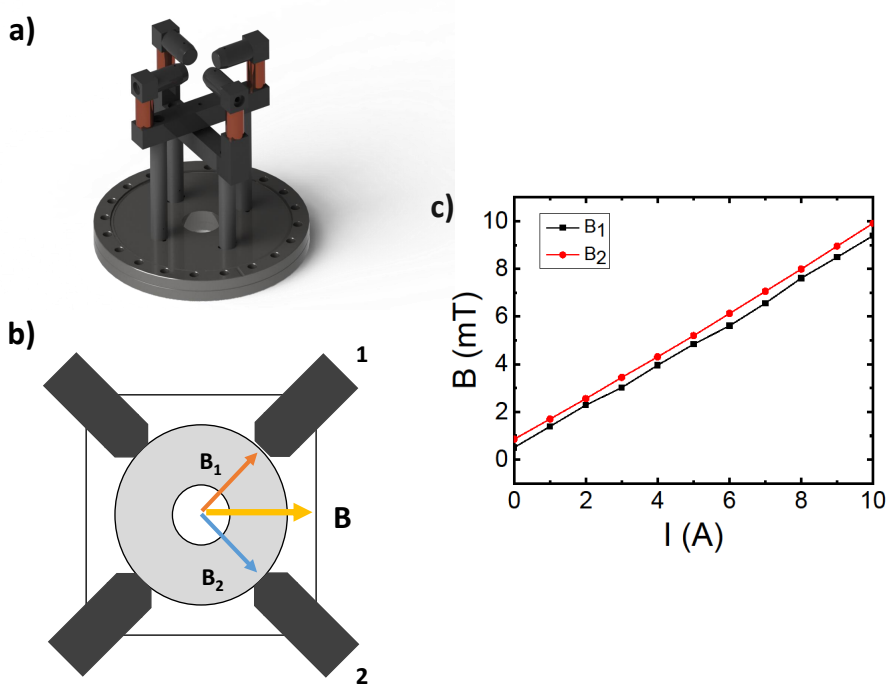


Figure 3.3 – (a) Rendering of the magnetic orientating field setup in the interaction zone. (b) Schematic of the magnetic field arrangement. (c) Calibration diagram of the solenoid magnetic field as a function of the applied current.

Each magnetic field should be calibrated. A magnetic probe is used to measure the magnetic field \vec{B}_i ($i = 1, 2$) when the current is applied to only one of the magnets as shown in Fig. 3.3 (b). Figure 3.3 (c) presents the calibration curves for the solenoid magnets. These magnetic fields are superposed in the interaction zone and result in a total field $\vec{B} = \vec{B}_1 + \vec{B}_2$. By varying the relative magnitude and the direction of the individual fields, we can control not only the total field strength but also its orientation. In the measurement, we also need to keep the amplitude of \vec{B} as a constant. The value of $|\vec{B}|$ needs to be set in a certain region where the maximum can

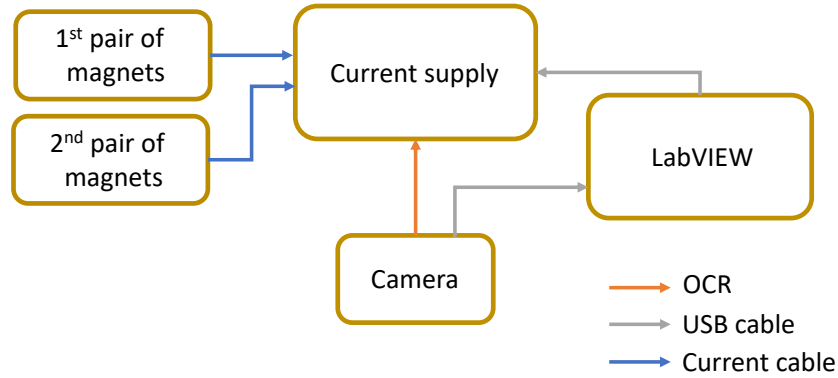


Figure 3.4 – Illustration of a magnetic field control loop. OCR is the abbreviation of optical character recognition.

achieve ≈ 15 mT due to the current supply and the minimum should be larger than 0.04 mT in order to surpass the effect of the earth's magnetic field.[116] Therefore, we set $|\vec{B}|$ to be ≈ 10 mT in all measurements with respect to different field directions.

Optical character recognition calibration

During an experiment, the orientation fields are set by computer-controlled (LabVIEW-based) current sources that are utilized for automation of the data acquisition (orienting the magnetic field direction to the desired one). Traditional analog remote controlling of the current supplies can roughly set to the desired values. However, further steps are required to achieve a high degree of control over the magnetic field direction: the field from one magnet can induce additional current on the current flowing through the solenoids of the other magnet. The display of the power supplies used here shows the effective current actually, but the control voltage does not take into account the induction from the other magnet. As a result, the control setting can lead to a false current.

To mitigate the problem of inductive coupling between the two solenoids it was necessary to implement a feedback loop for the control of the current supplies. A block schematic is shown in Fig. 3.4: initially, the two currents are set to the target values by setting the input control voltage on both power supplies, using LabVIEW and a digital/analog converter. The true current flowing through the coil is, however, different from that because of the inductive coupling with the second solenoid. In the current supplies used here (Delta Elektronika ES015), the true current is displayed on the device, hence a camera was used to monitor the display, and the numbers were interpreted using optical character recognition (OCR). The resulting value was fed back to the control software which adjusted the control value. This cycle was repeated until the difference between the measured value was within a set interval of the desired value. This approach permits the definition of the magnetic field direction with a

Chapter 3. Experimental apparatus and analysis

precision of better than 5 degrees.

3.1.4 Detection

A Wiley-McLaren TOF-MS is used to detect ions as shown in Fig. 3.1.[117] Figure 3.5 depicts its construction, which includes two metal plates, a TOF tube and a microchannel plate(MCP). The structure for the magnetic field generation slightly protrudes into the MS between the first and second electrodes and is adjusted in height to be aligned with the molecular beams. The second plate has a central hole with a diameter of 1 cm which is covered by a high-transmission Ni mesh. The

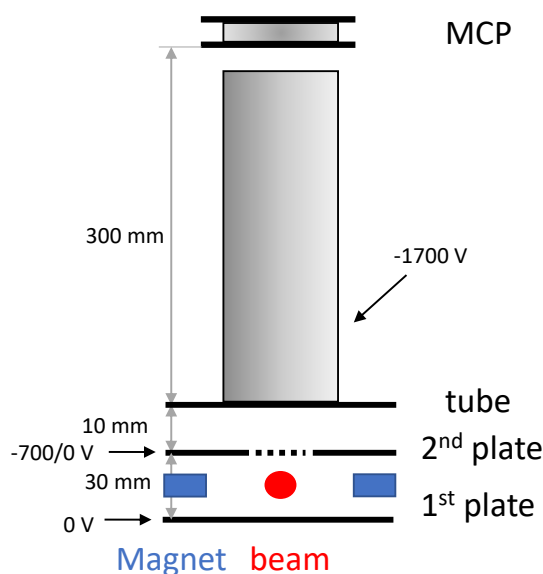


Figure 3.5 – Illustration of a Wiley-McLaren time-of-flight mass spectrometer with solenoid magnets. MCP is the abbreviation of microchannel plate.

During an experiment the MS is operated in a pulsed mode in order to select a narrow slice from within the complete molecular beam pulses. This procedure is critical to increase the energy resolution and reach the lowest collision energies (see Chapter 2). In this mode the voltage on the flight tube is kept constant at -1.7 kV which removes any product ion from the beam if formed outside the mass spectrometer. The repeller and extraction plates are both at 0V except for a duration of ≈ 1 microsecond during which products are accelerated toward the MCP and detected. Only collision products between the first two plates can pass through the mesh of the 2nd plate and be accelerated towards the MCP eventually. This MS has a resolution $m/\Delta m \approx 30$. [88] In the measurement, we find that different product ions have a similar detection efficiency so that we can neglect the magnetic field effect in the detection.

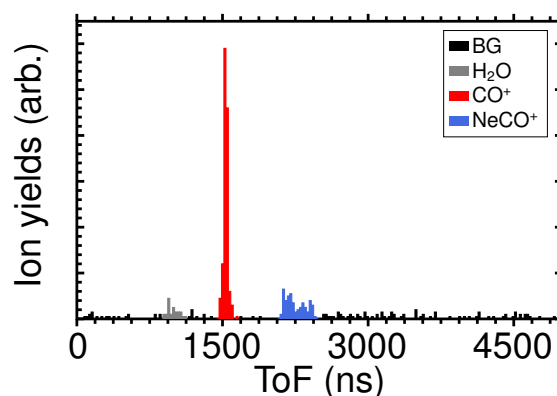


Figure 3.6 – Time-of-flight spectrum at a collision energy of 244 cm^{-1} and $\theta_{\text{KB}} = 90^\circ$ in the $\text{Ne}^* + \text{CO}$ reaction. BG is short for the background.

Event counting

At low collision energies, the ion signals in the chemi-ionization reduce substantially so that it is impossible to obtain a full TOF spectrum instead of single ion shots in the detection. In this case, we need to introduce the event counting technique here to obtain the full mass spectrum. In one measurement, we count every ion when it is extracted in the TOF-MS. Each ion shot is counted as one event at a given flight time in the mass spectrum. Repeating the measurements and counting all the ions can result in a digital spectrum. Typically, we could record a few hundred ions in one measurement which contains 15000 to 40000 single beam collisions over some time (5–20 min). A typical mass spectrum of the $\text{Ne}^* + \text{CO}$ reaction is shown in Fig. 3.6 where we can distinguish all product ions in the spectrum for future analysis.

3.2 Resonance-enhanced multiphoton ionization and detection

When the laser light interacts with an oriented or aligned sample, the interaction depends on an anisotropic distribution of transition-dipole moments that is related to an anisotropic distribution of angular momenta \vec{J} in space. The anisotropic distribution of transition-dipole moments has an influence on the degree of absorption or emission of different light polarization at a given angle. Here, linear polarized light is sensitive to alignment parameters.[90]

Therefore, resonance-enhanced multiphoton ionization (REMPI) is used as a detection tool to measure the orientation of Ne^* and to determine its populations in different M_J states, Here the laser beam is generated by a pulsed dye laser (Fine adjustment) pumped by a Nd:YAG laser (InnoLas SpitLight 1000). For the (1+2) REMPI characterization of the Ne^* sample, Q and P branch transitions through the $2s^2 2p^5(^2P_{3/2})3p(J)$ were used as detailed in Table 3.2.[118] Using a polarized laser, the direction of the laser polarization can be used to confirm and characterize the polarization of the sample. The polarization vector of the laser light is controlled using a $\lambda/2$ plate. This laser beam is then focused through an optical window into the experiment environment. The geometry of REMPI is shown in Fig. 3.7 (a). Photoions are detected using a channeltron (Photonis Magnum) mounted between the magnets.

Table 3.2 – Experimental conditions for the orientation detection

Atom	REMPI	Intermediate state	λ (nm)	Dye
$\text{Ne}(^3P_2)$	(1+2)	$2s^2 2p^5(^2P_{3/2})3p(J=2)$	614.306	DCM
		$2s^2 2p^5(^2P_{3/2})3p(J=1)$	621.728	

In order to confirm the orientation of the Ne^* beam, two independent probing geometries are shown in Fig. 3.7 b):

1. Red square symbols indicate the magnetic field is constant and parallel to the propagation direction of the Ne^* beam while the laser light polarization is controlled by the $\lambda/2$ wave plate.
2. Blue cross symbols indicate that the laser polarization is constant and parallel to the propagation direction of the Ne^* beam while the magnetic field is changed by tuning the currents in the solenoids.

The two graphs look nearly identical, thus confirming that: (1) the oscillations are not artifacts originating from the magnetic field and a potentially varied detection efficiency, and (2) the orientation of the Ne^* atoms follows the direction of the magnetic field adiabatically.

To analyze the angle-dependent intensities and extract M_J specific populations we employ the method developed by Rakitzis and Alexander.[119] To quantify the polarization they define the alignment parameters $A_q^{(k)}(J)$ that are given in Eq. 2.34. The measured intensities of specific REMPI transitions can then be calculated by taking into account the relative directions of laser

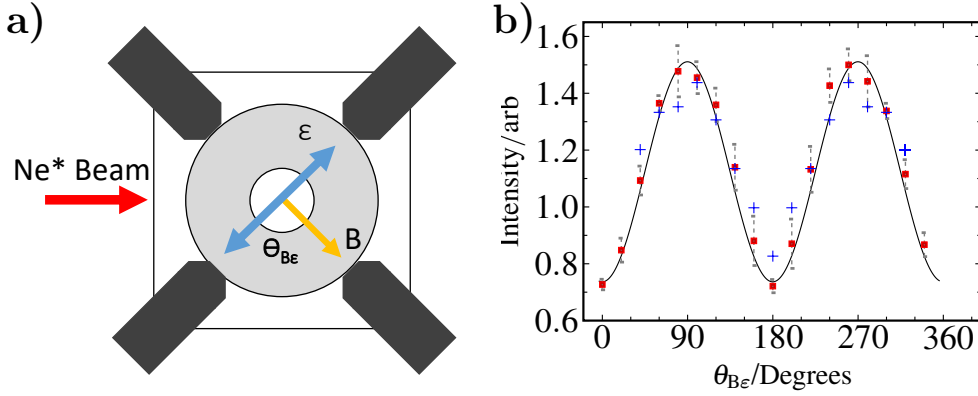


Figure 3.7 – (a) Illustration of the REMPI configuration. Linearly polarized laser light enters perpendicular to the experimental setup with the polarization ϵ . (b) REMPI signals are obtained by changing the magnetic field at a fixed linear polarization of the excitation laser light (blue cross), and by rotating the laser light polarization at a fixed magnetic field (red square).

polarization ϵ and magnetic field \vec{B} as well as the ΔM_J selection rules, giving in Ref. [115]

$$I(\theta_{B\epsilon}) = I_0 \left[1 + \sum_{k=1}^{2J} s_k(J, J', \lambda) P_k(\cos \theta_{B\epsilon}) A_q^{(k)}(J) \right] \quad (3.1)$$

where $\theta_{B\epsilon}$ is the angle between the laser polarization and the magnetic field direction, I_0 is a constant, $P_k(\cos \theta_{B\epsilon})$ is an associated Legendre polynomial and s_k are so-called detection sensitivity parameters which are given in Ref. [119]

$$s_k = P_k \frac{[J(J+1)]^{k/2} \sqrt{2k+1} \sqrt{2J+1}}{c(k) \langle J || J^{(k)} || J \rangle} \quad (3.2)$$

where $c(k)$ and $\langle J || J^{(k)} || J \rangle$ are the normalization factors and the reduced matrix elements introduced in Chapter 2.

In the case of Ne^* , the (J, M_J) states have cylindrical symmetry about the external field axis so that we only need to consider the case of $q = 0$ (cylindrical symmetry) and $J = 2$ (neon in the 3P_2 state). Using these parameters and $\rho_{2,2} = p_{M_J=2}$, $\rho_{1,1} = p_{M_J=1}$, $\rho_{0,0} = p_{M_J=0}$ and all

3.2. Resonance-enhanced multiphoton ionization and detection

other components $\rho_{M'_J, M_J} = 0$, we can obtain $A_q^{(k)}(J)$ from Eq. 2.34 in terms of p_{M_J} :

$$A_0^{(1)} = \frac{1}{\sqrt{6}}(p_{M_J=1} + 2p_{M_J=2}) \quad (3.3)$$

$$A_0^{(2)} = -p_{M_J=0} - \frac{1}{2}p_{M_J=1} + p_{M_J=2} \quad (3.4)$$

$$A_0^{(3)} = \frac{1}{\sqrt{12}}(-\sqrt{2}p_{M_J=1} + \frac{1}{\sqrt{2}}p_{M_J=2}) \quad (3.5)$$

$$A_0^{(4)} = \frac{1}{4}(p_{M_J=0} - \frac{2}{3}p_{M_J=1} + \frac{1}{6}p_{M_J=2}) \quad (3.6)$$

By fitting Eq. 3.1 to the spectrum, we not only find that $p_{M_J=0} = 0.087 \pm 0.015$, $p_{M_J=1} = 0.75 \pm 0.02$, $p_{M_J=2} = 0.163 \pm 0.025$, but also plot the fitted $I(\theta_{Be})$ as a black line in Fig. 3.7 (b).

3.3 Data analysis and fitting

A sample set of normalized raw data from the TOF-MS is shown in Fig. 3.8 (a) for $\text{Ne}^* + \text{Kr}$ collisions recorded at a collision energy of 313 cm^{-1} . The horizontal axis shows the time-of-flight while the out-of-plane axis shows the magnetic field angle in the laboratory reference frame. The early and late peaks show the Kr^+ (normalized to 1) and NeKr^+ ions, respectively. In this representation the fluctuation of the relative signal intensity as a function of angle is immediately visible. Integration of each of the peaks permits the calculation of the reactivity, defined as

$$R(\theta) = \frac{I_{\text{AI}}(\theta, E_{\text{coll}})}{I_{\text{PI}}(\theta, E_{\text{coll}})} \quad (3.7)$$

R needs to be expressed in the molecular reference frame, by rotating the angle of the magnetic field accordingly. This produces curves like the ones shown in Fig. 3.8 (b).

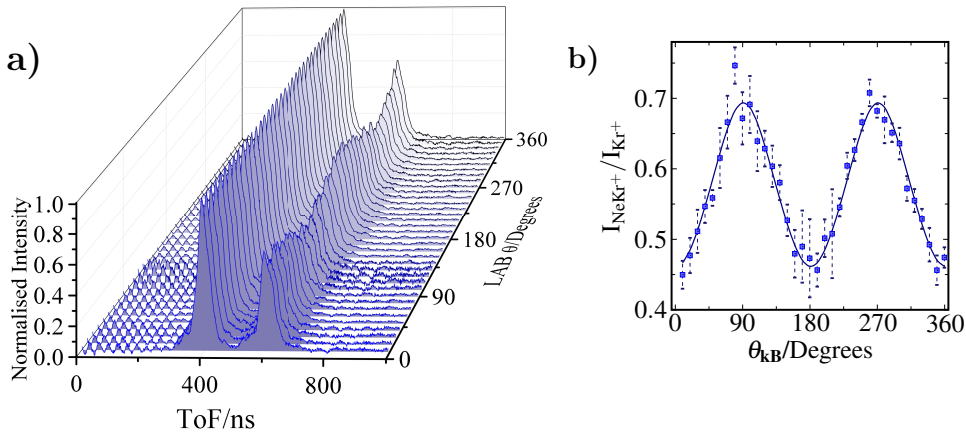


Figure 3.8 – a) Time-of-flight spectra as a function of the magnetic field direction, expressed in the laboratory reference frame, for the $\text{Ne}^* + \text{Kr}$ reaction at a collision energy of 313 cm^{-1} . b) Experimental and fitted reactivities $\text{NeKr}^+/\text{Kr}^+$ as a function of θ_{kB} in the molecular reference frame.

The observed signals are proportional to the cross sections $\sigma_{\text{AI;PI}}$ for the respective $\text{Ne}^* + \text{X}$ ($\text{X} = \text{Ar}, \text{Kr}, \text{Xe}, \text{N}_2, \text{CO}$) reaction channel. For the present case, they are in particular also explicitly defined for different magnetic quantum numbers. However, they need to be expressed in the molecular frame where the projection of \vec{J} on the interatomic axis, labeled Ω , is used rather than M_J . Because there is no coherence between the states with different Ω quantum numbers, the total product yield is the sum of all independent contributions. For each reaction channel (AI and PI) we define the ion yield as the sum of the contributions from the individual substates, each characterized by its own reaction cross section:

$$I_{\text{AI;PI}}(\theta_{\text{kB}}) = Q \sum_{\Omega=0}^J p_{\Omega}(\theta_{\text{kB}}) \sigma_{\text{AI;PI}}^{\Omega} \quad (3.8)$$

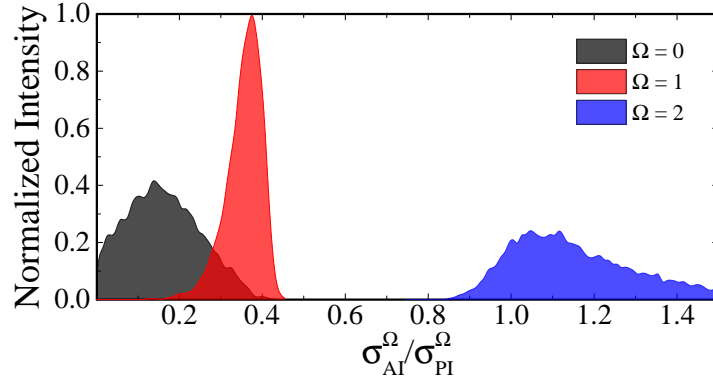


Figure 3.9 – Ω specific reactivities for the $\text{Ne}^* + \text{Kr}$ reaction at a collision energy of 313 cm^{-1} .

where Q is a constant to characterize the experimental condition. Although the Q value is unknown, we can assume that it changes slowly with time but is the same for the AI and PI channels. The initial M_J populations are retained during the orientation of the Ne^* atoms in the magnetic field. A frame transformation is utilized to rotate from the laboratory into the molecular reference frame, thus converting the M_J into Ω . The populations p_Ω for any given angle θ_{kB} between the magnetic field \vec{B} and the relative velocity \vec{k} , are obtained using reduced Wigner rotation matrices,[100]

$$p_\Omega(\theta_{\text{kB}}) = \sum_0^J p_{M_J} w_q |d_{\Omega,q}^J(\theta_{\text{kB}})|^2. \quad (3.9)$$

The w_q are the weighting coefficients, equal to 2 and 1 for $\Omega = 1, 2$ and $\Omega = 0$, respectively. By inserting Eq. 3.8 into Eq. 3.7, the reactivity can be written as

$$R(\theta_{\text{kB}}) = \frac{I_{\text{AI}}(\theta_{\text{kB}})}{I_{\text{PI}}(\theta_{\text{kB}})} = \frac{\sum_{\Omega=0}^J p_\Omega(\theta_{\text{kB}}) \sigma_{\text{AI}}^\Omega}{\sum_{\Omega=0}^J p_\Omega(\theta_{\text{kB}}) \sigma_{\text{PI}}^\Omega} \quad (3.10)$$

where only the Ω dependent populations of Ne^* and the state-dependent cross sections are left.

Since the fit-parameters in Eq. 3.10 are highly correlated, standard fitting methods fail to converge for this problem. This is because many values of the cross sections can lead to the same ratio making a standard fitting approach impossible. In order to overcome this issue, we make use of a Monte-Carlo fitting algorithm. The basic concept of this approach is to randomly generate sets of reaction cross sections and use those to calculate what reactivity they would produce. These synthetic results are then compared to the experimental data and retained only if the agreement lies within a predefined range. Specifically, the procedure is as follows: 6 random cross sections $\sigma_{\text{AI;PI}}$ are generated in the range between 0 and 10000 (units are arbitrary). Using the known p_Ω populations and taking into account the error margins in these values, Eq. 3.10 is then used to calculate the reactivities at all angles probed experimentally. The resulting curve is compared by the experimental data by calculating the root mean square

Chapter 3. Experimental apparatus and analysis

difference between the two data sets, and only if this value is below a certain threshold, the set of cross sections is retained, and these are the basis of the histogram shown in Fig. 3.9.

This procedure is repeated typically 10^{11} times and yields around 10000 accepted sets of cross sections. The principal result from these calculations are the most probable ratios of cross sections, i.e. the maxima in the histogram, and the confidence intervals defined by the width of the distributions. These cross sections are also the basis of the fitted curves and surfaces shown, for example, in Fig. 4.1.

4 Stereodynamics of Ne* with rare gases

This chapter will report the stereodynamics of the $\text{Ne}^* + \text{Rg}$ ($\text{Rg} = \text{Ar}, \text{Kr}$ and Xe) reactions using crossed and merged beams. We will discuss their reaction dynamics using two proposed reaction mechanisms and the results in this chapter are based on Refs. [14] and [120].

4.1 Introduction

The reaction dynamics between an excited rare gas atom and a ground state rare gas has been the target of many investigations in the past decades.[23] As an early example, Tang et al.[121] reported a total cross section measurement of the $\text{Ne}(^3P_{0,2}) + \text{Ar}, \text{Kr}$, and Xe reactions and found that the interaction leading to the ionization was short-range.

Later, Neynaber and Magnuson used a merging-beam setup to measure $\text{Ne}(^3P_{0,2}) + \text{Ar}, \text{Kr}$ collisions at $E_{\text{coll}} = 0.01\text{--}600$ eV and $E_{\text{coll}} = 0.01\text{--}10$ eV and they found that the PI cross section raised with decreasing E_{coll} , while the AI cross section increased with decreasing E_{coll} . [122, 123] At the same time, W. P. West et al. [124] measured the branching ratios of the $\text{Ne}(^3P_{0,2}) + \text{Rg}$ ($\text{Rg} = \text{Ar}, \text{Kr}$ and Xe) reactions at a collision energy of 435 K. All these results are presented in Table 4.1.

Table 4.1 – Branching ratios in the $\text{Ne}(^3P_{0,2}) + \text{Ar}, \text{Kr}$ and Xe collisions

Branching ratio	$\text{Ne}(^3P_{0,2})$		
	Ref. [124]	Ref. [125]	Ref. [126]
$\text{NeAr}^+/\text{Ar}^+$	0.449		0.5151
$\text{NeKr}^+/\text{Kr}^+$	0.429	0.515	0.471
$\text{NeXe}^+/\text{Xe}^+$	0.316	0.299	
Temp (K)	435	435	330

In addition to the experiments, the high-temperature theory of the $\text{Ne}(^3P_2) + \text{Rg}$ reactions was first developed by Gregor and Siska where they calculated the optical potentials of $\text{Ne}(^3P_{0,2}) +$

Rg reactions. In their models, they found that the real parts of the potentials were similar to the sodium-rare gas van der Waals potentials. The imaginary parts Γ confirmed a Coulomb or radiative mechanism in PI.[127] Brumer and co-workers[128] reported a theoretical calculation of the coherent control of PI and AI of the $\text{Ne}(^3P_2) + \text{Ar}(^1S_0)$ reaction at collision energies of 1–8 kcal/mole. The results were explained by describing the collision complex in a Hund's case (c) coupling scheme, using the projection of \vec{J} on the internuclear axis to define Ω and classify the states accordingly. And they predicted that reactivities $R_\Omega = \sigma_{\text{AI}}/\sigma_{\text{PI}}$ were small and of a similar magnitude for $\Omega = 0$ and $\Omega = 1$ but larger for $\Omega = 2$.

More recently, Falcinelli and co-workers used a crossed molecular beam apparatus to study the chemi-ionization between $\text{Ne}(^3P_{0,2})$ and Rg. An important finding is that at low-energy collisions between $\text{Ne}(^3P_2)$ and a rare gas atom, the ratio of the cross sections for AI and PI, $\sigma_{\text{AI}}/\sigma_{\text{PI}}$, maximizes for neon atoms in the $|J, \Omega\rangle = |2, 2\rangle$ entrance channel. This was explained in terms of a less repulsive wall in the $V_{|2,2\rangle}$ potential that appears at an intermediate distance of the $\text{Ne}(^3P_2)$ - $\text{Rg}(^1S)$ potential curve and opens a favorable pathway to the trapping in the potential well of the exit channels. In contrast, at high collision energies the branching ratio between the AI and PI channels drops rapidly because the reactions provide ionic products confined in the repulsive region of the exit channels, leading to dissociated ions.[129]

4.2 Stereodynamics of the Ne* + Rg reactions

This section describes the stereodynamics of the Ne* + Rg (Rg = Ar, Kr and Xe) reactions in a crossed-molecular-beam apparatus at collision energies of 320–500 cm⁻¹.

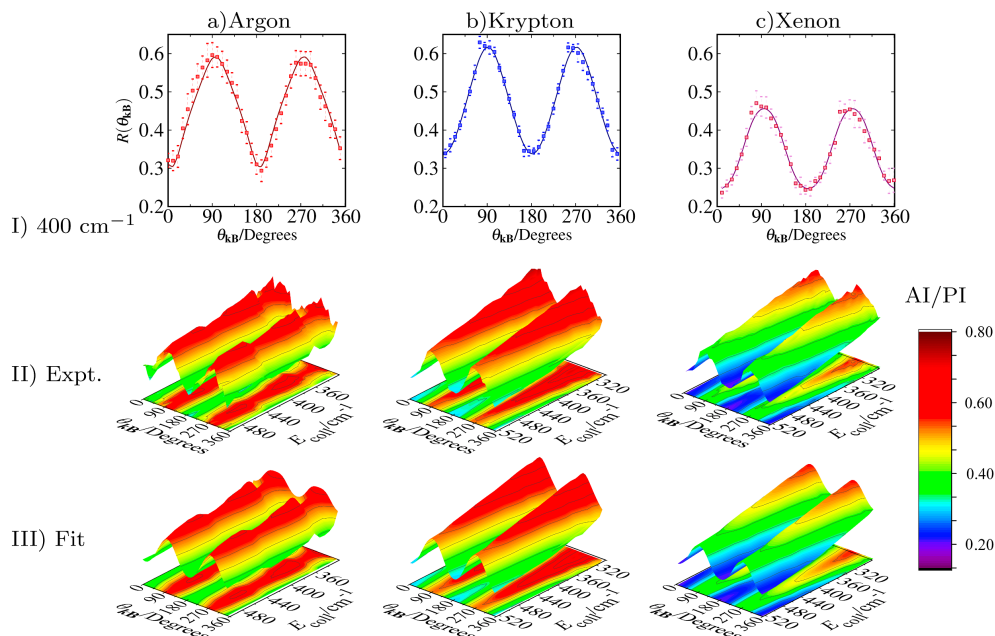


Figure 4.1 – Reactivities and interpolated and fitted surfaces for different rare gas atoms reacting with Ne*.

The principal experimental data from these studies are shown in Fig. 4.1. The top row presents the angle-dependent reactivities R at a collision energy of 400 cm⁻¹. The data are analyzed by fitting Eq. 3.10 to the experimental data, using the algorithm described in Chapter 3, and the results are shown as solid lines in Fig. 4.1I. The surfaces in row II show the experimental values of R as a function of angle (in the molecular reference frame) and collision energy. The fitted surfaces are shown in row III of Fig. 4.1. The energy-dependent reactivities shown in Fig. 4.1II and III reveal that overall, all reactivities decrease with increasing collision energy. $R(\theta_{kB})$ is minimum when the relative velocity \vec{k} is aligned to the magnetic field \vec{B} , parallel or anti-parallel and maximum when the relative velocity \vec{k} is perpendicular to the magnetic field \vec{B} . The magnitude of R oscillates around 0.5 in the Ne* + Ar, Kr reactions, and around 0.4 in the Ne* + Xe reaction at 400 cm⁻¹.

The actual Ω specific ratios σ_{AI}/σ_{PI} are shown in Fig. 4.2 as a function of collision energy, where the confidence interval is shown as a shaded area and corresponds to the full-width at half-maximum from the distributions. These values are used with Eq. 3.10 to calculate the surfaces shown in row III of Fig. 4.1.

For an easier comparison, Fig. 4.3 shows the Ω specific reactivities for all these reactions at a collision energy of 400 cm⁻¹. Each bar corresponds the reactivity measured for one particular

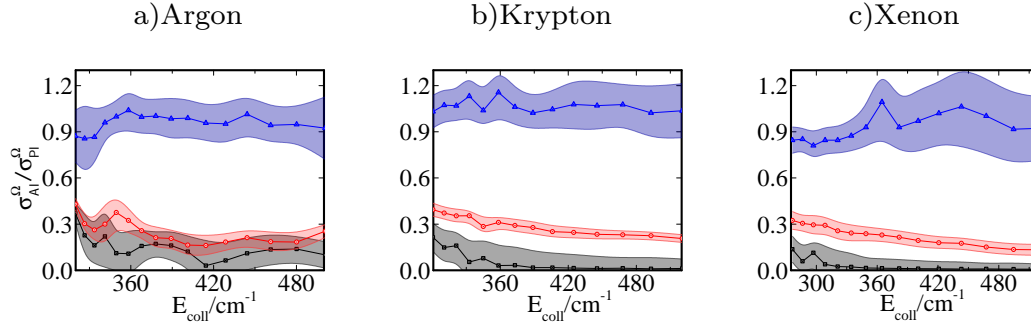


Figure 4.2 – Experimental reactivities $\sigma_{AI}^{\Omega}/\sigma_{PI}^{\Omega}$ as a function of collision energy. In each case, the values for $\Omega = 0, 1$, and 2 are shown in black, red, and blue, respectively. The shaded areas represent one standard deviation.

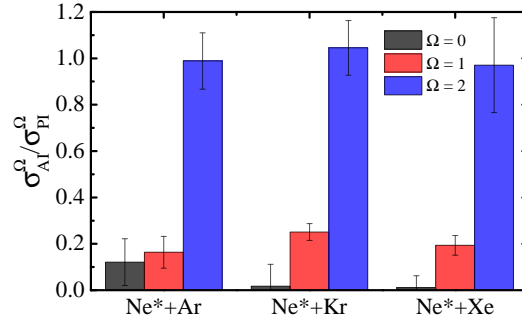


Figure 4.3 – Histogram of the specific reactivities at 400 cm^{-1} for the $\text{Ne}^* + \text{Ar}$, Kr and Xe reactions (left to right).

value of Ω and one rare gas. For each system, the reactivity raises with increasing Ω . The $\sigma_{PI}^{\Omega=2} \approx \sigma_{AI}^{\Omega=2}$ while the $\sigma_{PI}^{\Omega=0,1}$ are significantly larger than the $\sigma_{AI}^{\Omega=0,1}$. The reactivities in the $\Omega = 0, 1$ are similar throughout.

In order to quantify the effect of the field, we introduce a quantity (steric effect) which describes the amplitude of the angle-dependent oscillations. To determine it, we calculate the ratio of the reactivities at $\theta_{kB} = 90^\circ$ and $\theta_{kB} = 0^\circ$, i.e. the maximum and minimum of the oscillation. If the ratio is close to 1, no angle-dependent ratios are observed, i.e., no steric effect. The larger the ratio is, the more substantial steric effect occurs in the reactions. Over the entire collision energy range, we find that the ratios deduce with lower collision energy in the range of $320\text{--}500 \text{ cm}^{-1}$. The largest reactivity ratio (2) is in the $\text{Ne}^* + \text{Ar}$ while the minimum ratio (1.4) in the same reaction is at 320 cm^{-1} . Overall, the difference between these reactions is not significant in the steric control at high collision energies.

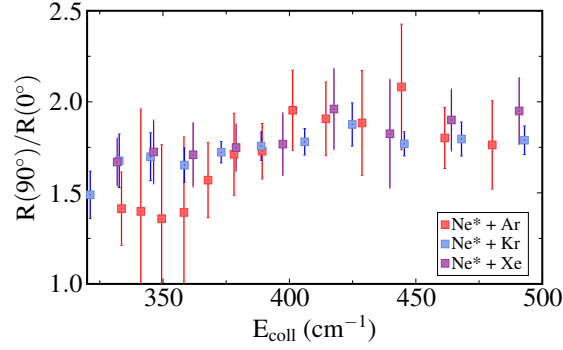


Figure 4.4 – Steric effect for Ar (red), Kr (blue) and Xe (violet) defined as the ratio between the reactivities R at $\theta_{\text{KB}} = 90^\circ$ and $\theta_{\text{KB}} = 0^\circ$ as a function of collision energy. A value of 1 indicates no dependence on the Ne* orientation.

4.3 Sub-Kelvin stereodynamics of the Ne* + Ar reaction

The low-energy stereodynamics study of the Ne* + Ar reaction in the merged-beam experiment at collision energies of 20 mK–1000 K will be discussed in this section as the high-level theory is available.[128, 17] Here we discuss not only the experimental result but also the numerical model in Chapter 2 that is used to describe the reaction dynamics.

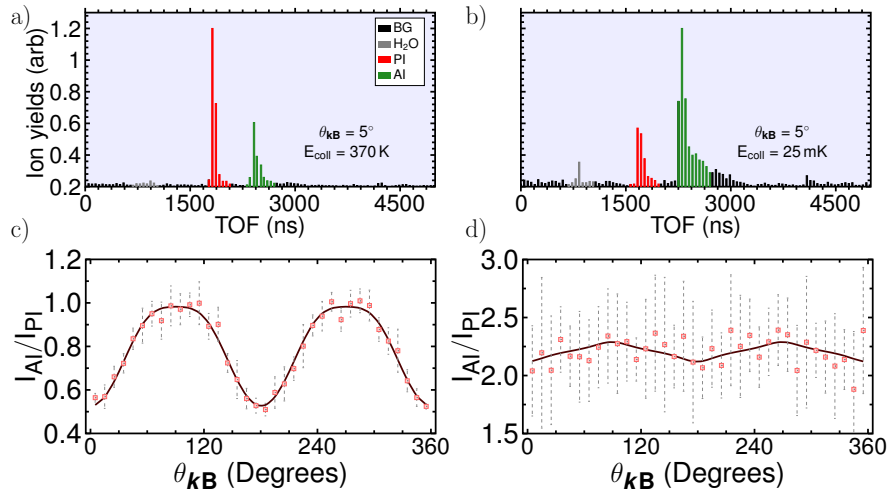


Figure 4.5 – Sample of raw ToF spectra at $\theta_{\text{KB}} = 5^\circ$ for (a) $E_{\text{coll}}/k_B = 370$ K and (b) $E_{\text{coll}}/k_B = 25$ mK. (c), (d) The reactivity, $I_{\text{AI}}/I_{\text{PI}}$, as a function of θ_{KB} for the same collision energies. BG is short for background.

A panel in Fig. 4.5 shows two examples of mass spectra at a collision energy of 370 K (a) and 25 mK(b), respectively. By integrating the ion yield as a function of θ_{KB} , the reactivities $I_{\text{AI}}/I_{\text{PI}}$ are precisely determined on the bottom. The fitted solid lines in Figs. 4.5 (c) and (d) are not only constrained by the Monte-Carlo fitting procedure for the intensities themselves but also by the ratio of the intensities. From this panel, we find that 1) as the orientation angle θ_{KB} , is

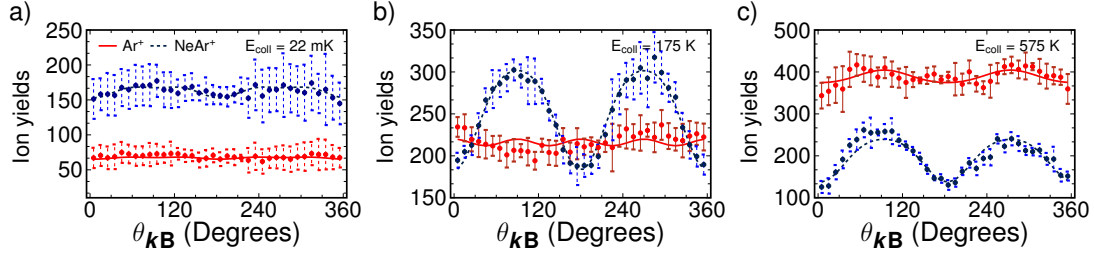


Figure 4.6 – Ion yields of the associative ionization and Penning ionization channels at different collision energies, $E_{\text{coll}} = 22$ mK (a), 175 K (b) and 575 K (c).

varied from 0° to 360° , the reaction oscillates between PI dominated and AI dominated at high temperature (370 K) while the AI dominates at low temperatures (25 mK). 2) The steric effect is strong at high collision energies and we lose the steric control at low collision energies.

In certain cases the experimental long-term stability was sufficiently high to obtain reliable yields for AI and PI alone in Fig. 4.6, eliminating the need to calculate the reactivity. The error bars are the standard deviation of the yields over multiple experimental runs. In these cases, the AI channel determines the steric effect, and the PI channel is insensitive to the orientation of the magnetic field. The solid red and blue dashed lines are obtained by fitting Eq. 3.8 to the AI and PI signals individually.

Figure 4.7 (a),(b) show the raw and fitted reactivity, respectively, as a function of orientation angle θ_{kB} and collision energy. The degree of AI and of PI can be tuned simply by turning the field direction and shifting the collision energy, which allows control of the reaction outcome externally. Selecting reactivity at $\theta_{\text{kB}} = 90^\circ$ (blue dotted line) and $\theta_{\text{kB}} = 180^\circ$ (red dashed line) can give the steric information directly as they are corresponding to the maximum and minimum reactivity respectively. In the fitted reactivity surface, the fitted method can also recover the state-dependent cross sections, whose ratios are shown in Fig. 4.8 as red traces for $\Omega = 0, 1$, and 2 , respectively. In these figures, we find that: the $\Omega = 0, 1$ reactivities are close to zero at high energies and rise to ≈ 2 below 40 K, and the $\Omega = 2$ reactivity oscillates around 2 over the entire collision energy range.

Theoretical calculations based on the scaled Verheijen and Beijerinck optical potential[128] are shown in Fig. 4.8 together with the experimental data. In the model, we neglect reorientation in collisions. The details about the theoretical calculations are given in Chapter 2. In brief, the Ne*–Ar entrance channel is originated from an optical potential, which describes the probability of ionization as a function of internuclear distance for each Ω and exit channel for AI(or PI). The width given from the potential describes the continuum of energy states that correspond to the ejected electron energy. The real part of the optical potential describes each atom dynamics during collisions and is assumed to be indistinguishable for each Ω state. By computing the scattering amplitudes including the scattering state in the entrance channel,

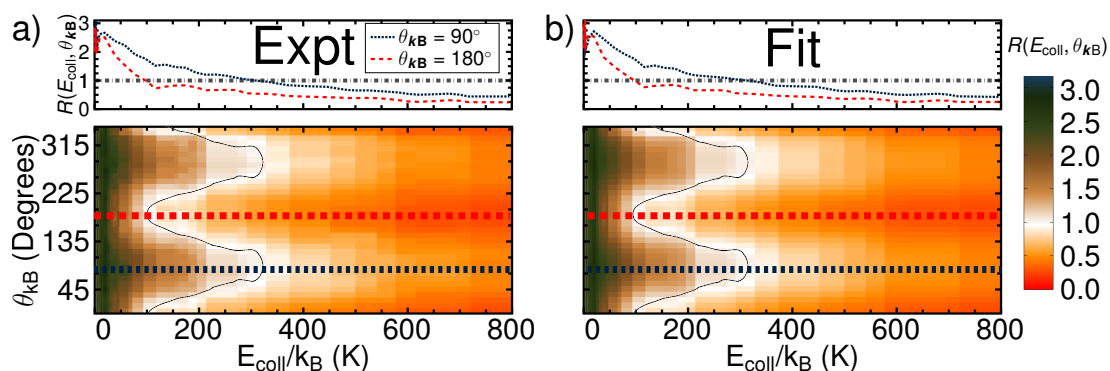


Figure 4.7 – Experimental (a) and fitted (b) two-dimensional plots of the complete angular-dependent data cover the entire energy range. The white region, overlaid by a smoothed contour, shows the area in which the PI and AI channels have equal ion yields $R(\theta, E_{\text{coll}}) = 1$. The properties of the slices at $\theta_{\text{kB}} = 90^\circ$ (blue dotted line) and $\theta_{\text{kB}} = 180^\circ$ (red dashed line) are given above the heat maps.

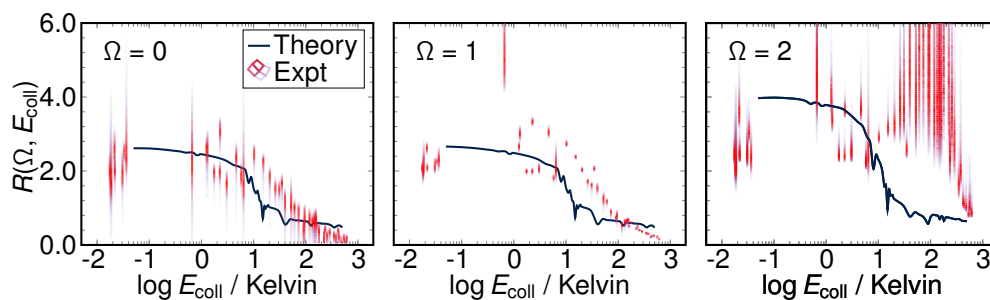


Figure 4.8 – Experimental (red) state-dependent reactivities that quantify the steric effect are compared with the theoretical values (black).

final continuum and the bound state of the exit channel, the theoretical results are depicted in black curves.

Compared to the experimental data, the calculated ionization ratios reproduce the general trend in the state-dependent reactivity, but the overall form of the curves shifted to lower energies. The trend obtained theoretically is similar to all Ω values and we find that a plateau region is below approximately 7 K. Above this temperature, the computed ratio falls drastically until ~ 20 K, and continues to diminish at a lower rate. This sudden drop is related to the shape of the repulsive barrier and the structure of the exit channels. And we also find that the agreement between the theoretical calculations and the experiment is good for $\Omega = 0, 1$, but the agreement doesn't work for $\Omega = 2$. For example, the drop of the experimental reactivity occurs at higher energies than the predicted one. To improve the agreement between experiment and theory, more accurate ab initio calculations of the potential energy surface will be required in the future.

Figure 4.9 shows a plot of the steric effect as a function of collision energy. Here the plot

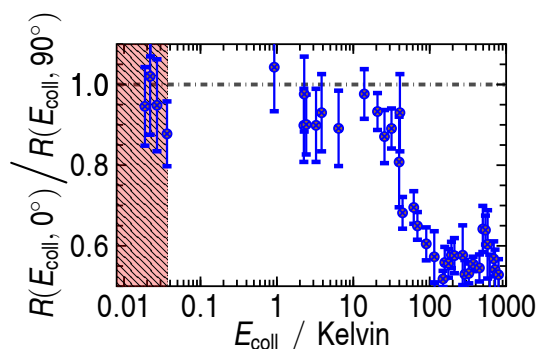


Figure 4.9 – The steric effect in the Ne* + Ar reaction. A value of 1 indicates no preference for specific orientations, hence no steric effect, while a value different from 1 indicates a strong dependence on the orientation. The red-shaded area below ≈ 30 mK shows the region of collision energies where the present experiment does not permit orientation control because the longitudinal and transverse velocities are similar.

values are the ratio between $R(E_{\text{coll}})$ at 0° (the minimum in Fig. 4.7) and that at 90° (the maximum). If this ratio is close to 1, the steric control is lost. The steric effect is strong at high collision energies and disappears around 30 K. As no steric effect is observed at lower temperatures, dynamical effects (dynamic reorientation) can result in its disappearance in this range. At low energies, the incoming reagent approaches another one very slow because of the low relative speed. The long-range part of the potential can shift the atoms into a favorable orientation for the complex formation before the energy transfer occurs resulting in a greater degree of the complex formation and therefore more AI. At higher energies, using an external field to position reagents manually can induce more AI. Please note that the stereodynamics experiments require a well-defined relative velocity, \vec{k} , between the reactants, which in the present case means that the longitudinal velocity, which we control, needs to be substantially larger than the transverse ones that are not controlled. The transition point, at which the full-width at half-maximum (FWHM) spread of the transverse velocities reaches the difference in the forward velocity occurs at energies of around 30 mK as indicated by the shaded area in Fig. 4.9. As the ratio of the longitudinal energy to the transverse energy spread gradually increases, it is clear that the absence of the steric effect at energies up to 30 K cannot be explained by the kinematics alone but must be due to an inherent effect of the reaction dynamics.

4.4 Dynamics of the $\text{Ne}^* + \text{Rg}$ reactions

It was proposed theoretically that in the $\text{Ne}^* + \text{Rg}$ reactions, two independent mechanisms excellently explained PI and AI formation: ‘exchange’ and ‘radiative’ mechanisms.[130] The mechanisms are sketched in Fig. 4.10. As argued below, the relative importance of these two mechanisms depends on the Ω quantum number because this is related to the orientation of the Ne^* electron cloud.

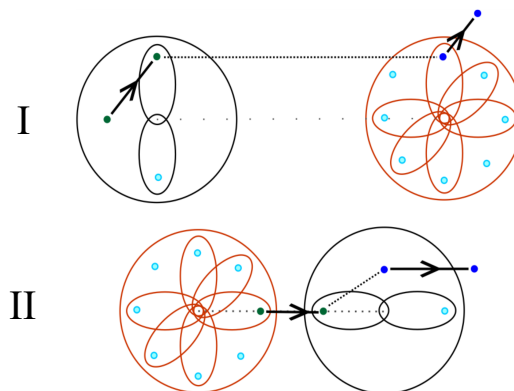


Figure 4.10 – (I) Radiative mechanism, occurring at long range and (II) exchange mechanism, taking place at short range.

The radiative mechanism (outlined in Fig. 4.10(I)) is believed to dominate mainly at long range. In this mechanism, an excited s electron from Ne^* de-excites into the p orbital, i.e., $(\text{Ne}(^3P_2) \rightarrow \text{Ne}(^1S))$ with the emission of a virtual photon. The virtual photon releases its internal energy to ionize the collision partner after the energy release.[130, 131] Thus, the orientation of Ne^* in the AI channel has little influence on the reactivity because mechanism I takes place at long internuclear distances, the probability for complex formation is small. As a result, mechanism I is believed to only lead to PI.

The exchange mechanism (illustrated by Fig. 4.10(II)) takes place at shorter distances. Here the outer p electron of Rg is transferred to the vacant p orbital of Ne^* , leading to ionization. This process requires overlap between the p -orbitals and thus is strongly dependent of the interatomic distance. It becomes most efficient when the singly occupied p orbital of Ne^* overlaps with Rg, meaning that the process becomes more efficient for $\Omega = 2$ when the p orbital is aligned along the bond axis than $\Omega = 0$ and 1 where it is perpendicular to the bond axis. The exchange mechanism can lead to both AI and PI, but because of the more favorable orbital overlap for complex formation, the propensity for AI is enhanced for $\Omega = 2$.

We find experimentally that for $\Omega = 2$, AI has approximately the same cross section in the PI channel at high energies (> 100 K), as shown in Fig. 4.3. In this configuration, the Ne^* and Rg atoms can form the intermediate complex through the exchange mechanism. When the p orbital is aligned along the internuclear axis, the configuration favors exchange and the internal energy transfers from the excited electron to the bound ro-vibrational states

in the complex, which determines the cross sections for the AI and PI channels. When $\Omega = 0$ and 1, the Rg p orbital overlaps less than that of the Ne p orbital which suppresses the complex formation. We also consider the radiative mechanism, which can cause PI before the complexation occurs. With declining collision energy, the AI channel is increasing in importance for $\Omega = 0$ and 1. Three Ω specific reactivities tend to have the same value at the lowest collision energy. Here, this trend indicates either that, at these energies, the long-range radiative mechanism is becoming less favored at low collision energies. The stereodynamics study of Ne* + Ar confirms that the radiative process should lose its importance entirely when the collision energy approaches zero.

5 Stereodynamics of Ne* with diatomic molecules

In the previous chapter, we described the stereodynamics of the $\text{Ne}^* + \text{Rg}$ reactions. We show that the reactivities $I_{\text{AI}}/I_{\text{PI}}$ are sensitive to Ne^* orientation and collision energy. In this section, we will discuss the dynamics in the triatomic $\text{Ne}^* + \text{X}$ ($\text{X} = \text{N}_2$ and CO) reactions. The discussion is based on Refs. [77, 120, 132].

5.1 Introduction

In chemical reactions, a triatomic reaction is challenging to investigate because of the complexity of molecules. Here we choose two simplest molecules X ($\text{X} = \text{N}_2$ and CO) reacting with Ne^* because they are isoelectronic molecules and have similar reaction channels, i.e., Penning ionization and associative ionization as mentioned in Chapter 1.

The earliest Penning electron and photoelectron spectra in the $\text{Ne}(^3P_{0,2}) + \text{N}_2$ chemi-ionization was given by Hotop and Niehaus.[133] Later, Sonnenfroh and Leone reported vibrational-rotational N_2^+ distributions in the $\text{Ne}^*(^3P_2) + \text{N}_2$ reaction, probed using laser-induced fluorescence.[134] Meanwhile, Appolloni et al.[135] found that the branching ratio $\text{N}_2^+/\text{NeN}_2^+$ decreased at lower collision energies in the $\text{Ne}(^3P_{0,2}) + \text{N}_2$ reaction.

In the comparison of N_2 chemi-ionizations, CO molecules have been rarely reported in chemi-ionization with metastable neon. The earliest study was reported by West et al.[124] in the reaction between $\text{Ne}(^3P_{0,2})$ and CO where they found 92.5% of NeCO^+ and 7.5 % CO^+ at a collision energy of 435 K. Later, energy-dependent cross sections in the $\text{Ne}(^3P_{0,2}) + \text{CO}$ reaction at collision energies of 0.02–0.4 eV were reported by Appolloni et al,[135] where they found that the AI cross section increased with decreasing collision energy while the PI decreased with declining collision energy.

5.2 Stereodynamics of the Ne* + N₂ reaction

The first investigated triatomic reaction is Ne* + N₂ reaction. It was performed in a crossed beam setup at collision energies of 320–500 cm⁻¹.

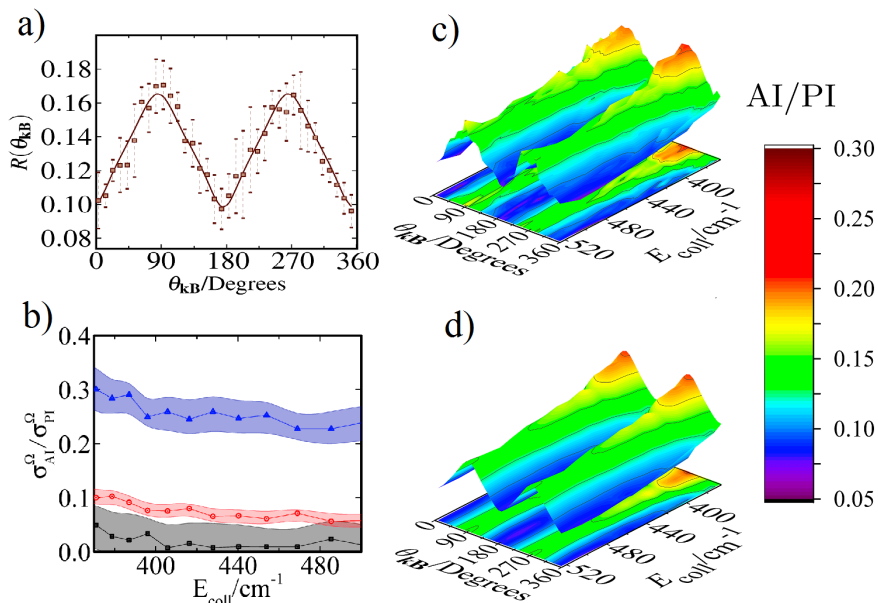


Figure 5.1 – Experimental and fitted data for the Ne* + N₂ reaction. (a) The reactivity across the angular range at 400 cm⁻¹. (b) Ω specific reactivities as a function of collision energy. (c) Experimental and (d) fitted reactivities across the energy range of the cross-beam experiment.

The principal results from this study are represented in Fig. 5.1. Panel (a) shows the experimental reactivity $I_{\text{NeN}_2^+}/I_{\text{N}_2^+}$ as a function of θ_{kB} in the molecular reference frame at a collision energy of 400 cm⁻¹. The fitted reactivity is also plotted as a solid line in the same figure. Panel (c) shows the experimental reactivity surface at collision energies of 320–500 cm⁻¹ while the fitted reactivity surface is given in Panel (d). Finally, Fig. 5.1 (b) shows the Ω -specific reactivities σ_{AI}/σ_{PI} as a function of collision energy. In order to understand the difference between the Ne* + N₂ reaction and the Ne* + Rg reactions, we add the Ω dependent reactivity of the Ne* + N₂ reaction to the histogram in Fig. 4.3, creating a new histogram shown in Fig. 5.2. For each system, the reactivity increases with increasing Ω . $\sigma_{AI} \approx \sigma_{PI}$ for $\Omega = 2$ in the Ne* + Rg reactions while $\sigma_{AI} < \sigma_{PI}$ for $\Omega = 2$ in the Ne* + N₂ reaction.

It has been shown that the potential energy surfaces of Ne* + Ar, Ne* + N₂ are similar,[136] and we should expect similar Ω specific reactivity distributions at the same collision energy. However, we find a big difference between these reactions which indicates that another reaction process occurs after collisions as we only detect the final product ions in the AI and PI channels. In Ne* + N₂, like in the case of the rare gases, the reaction is believed to proceed through an intermediate complex $[\text{NeN}_2]^+$ which then autoionizes.[137] However, in contrast to the atomic systems, the vibrational structure of N₂⁺ opens a new decay channel wherein a

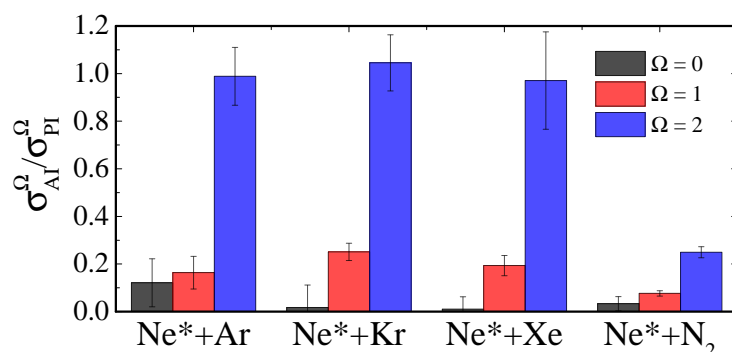


Figure 5.2 – Histogram of the Ω specific reactivities at 400 cm^{-1} for $\text{Ne}^* + \text{Ar}$, Kr , Xe , and N_2 (left to right).

complex is formed on the neutral excited surface which decays to a vibrationally excited state on the ionic surface. In this state, internal energy transfer can move vibrational excitation from the N-N bond to the Ne-N_2^+ bond and lead to dissociation. In a previous experiment, Sonnenfroh and Leone first observed a bimodal rotational distribution in N_2^+ spectra, giving an indirect evidence of this predissociation pathway (PD).[134] The vibrational frequency of N_2^+ is 2207 cm^{-1} , [30] while the Ne-N_2^+ binding energy is estimated, on the basis of experimental data, to be 300 cm^{-1} . [138] As a consequence, even a single quantum of vibrational excitation in N_2^+ is sufficient to dissociate the complex. The predissociation timescale is estimated to be 10^{-10} s . [120] As the dissociation process of AI ions (e.g. Ne-N_2^+) has a faster timescale than the flight time in a TOF-MS ($\sim 10^{-7} \text{ s}$), the predissociated ions can join the PI ions so that we cannot distinguish them from the spectrum using the current experimental apparatus. Quantitative determination of the predissociation efficiency requires additional experiments at low temperatures.

5.3 Sub-Kelvin stereodynamics of the Ne* + N₂, CO reactions

As the crossed beam experiment of the Ne* + N₂ reaction stops at at 320 cm⁻¹, the reactivity at lower collision energies is unknown. In this section, we add another system (Ne* + CO reaction) to explore the low-energy stereodynamics of the Ne* + X (X = N₂ and CO) reactions. All experiments were performed in the merged-beam apparatus. The details are similar to the Ne* + Ar reaction case.

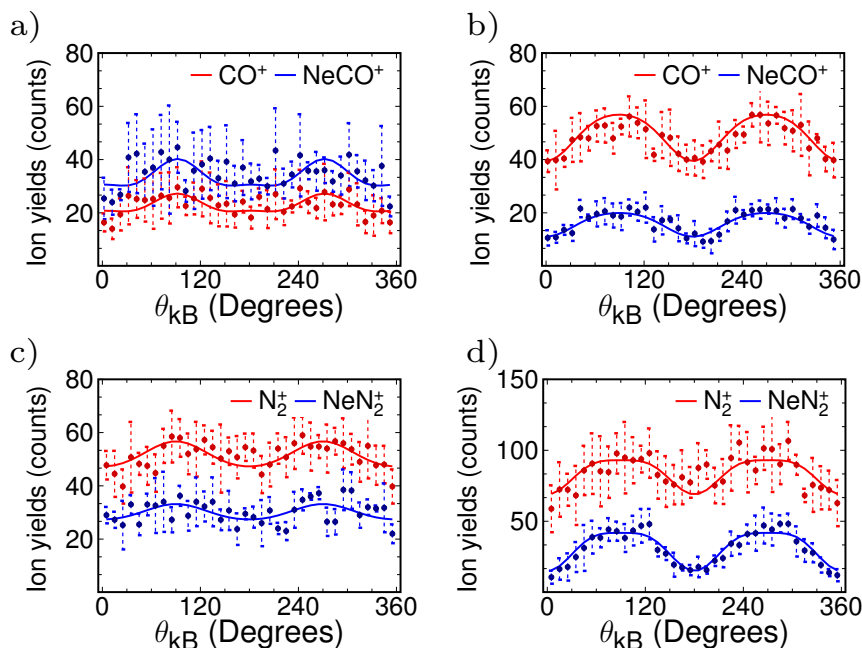


Figure 5.3 – Examples of angle-dependent ion yields: at $E_{\text{coll}}/k_B = 600$ mK for (a) the Ne* + CO reaction and (c) the Ne* + N₂ reaction and at $E_{\text{coll}}/k_B = 352$ K for (b) the Ne* + CO collision and (d) the Ne* + N₂ collision.

Figure 5.3 shows angle-dependent ion yields for Ne* + CO [panels (a) and (b)] and Ne* + N₂ [panels (c) and (d)] at different collision energies. Panels (a) and (c) show the results obtained at a collision energy of 600 mK; and panels (b) and (d) show those at 352 K. Each panel shows bare molecular ions X⁺ as red symbols and complex ions NeX⁺ as blue symbols. Fitting these data provides cross sections for each reaction channel and generates the solid lines in Fig. 5.3. The complete dataset over the entire energy range (0.2–700 K) is shown in Fig. 5.4 including the experimental ratio surfaces $I_{\text{NeX}^+}/I_{\text{X}^+}$ as a function of collision energy and θ_{kB} . Analyzing the reactivity rather than the raw ion signals eliminates most of the noise and signal fluctuations.

To isolate the energy-dependent reactivity in Fig. 5.4 from the steric effect, the ion yields are integrated over all angles, generating the curves in Fig. 5.5. In this figure, the ion yield ratios $r(\theta_{\text{kB}}) = \frac{I(\text{NeCO}^+)}{I(\text{CO}^+)}$ or $\frac{I(\text{NeN}_2^+)}{I(\text{N}_2^+)}$ are given in red and blue, respectively, over the entire energy range covered here, that is, between 0.2 and 700 K. We find that the formation of bare ions dominates over the whole energy range in the case of N₂, while the ratio becomes larger than one at

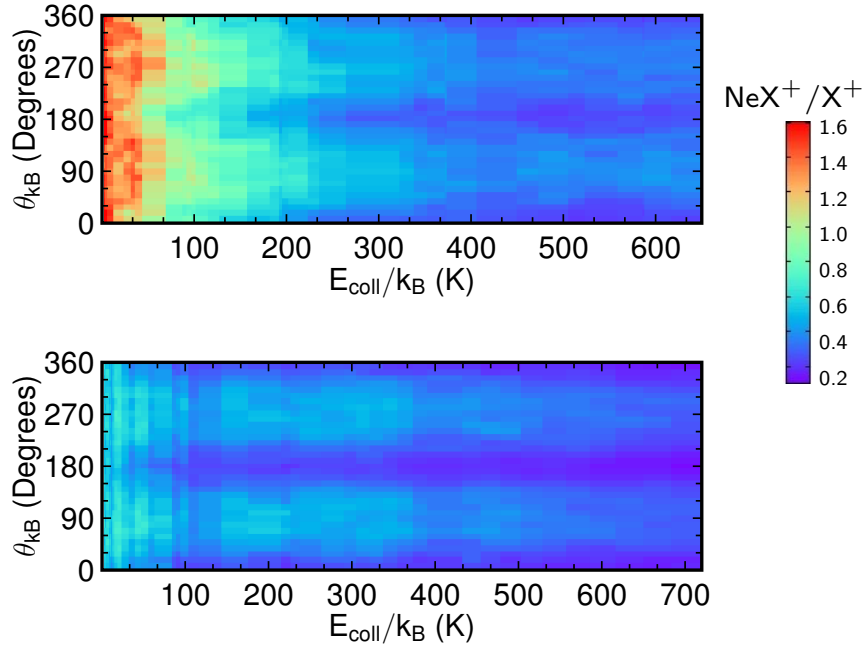


Figure 5.4 – Experimental ratio $I_{\text{NeX}^+}/I_{\text{X}^+}$ ($\text{X} = \text{CO}$ and N_2) as a function of θ_{kB} and collision energy in the range of 0.06–700 K for the $\text{Ne}^* + \text{CO}$ reaction (top) and the $\text{Ne}^* + \text{N}_2$ reaction (bottom).

energies below ≈ 100 K in the case of CO.

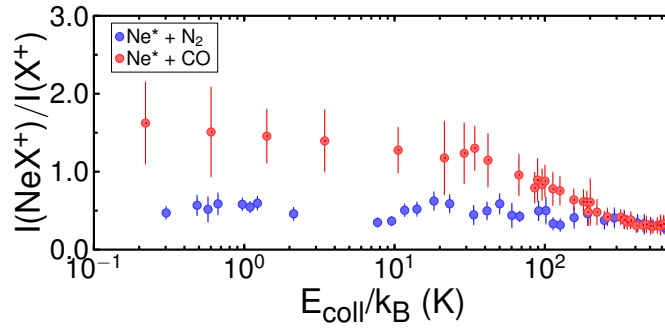


Figure 5.5 – Raw ion yield ratio for the production in the $\text{Ne}^* + \text{N}_2$, CO reactions as a function of collision energy.

Inspection of the angle-dependent ratios allows to extract the steric effect in terms of total relative cross sections for NeX^+ and X^+ formation by quantifying the amplitude of the angle-dependent oscillations. The energy-dependent steric effect, as it is shown in Fig. 5.3 (b) and (d), is used to calculate the ratio between the relative ion yield ratios at 90° and at 180° . This ratio, $r(\theta_{\text{kB}} = 180^\circ)/r(\theta_{\text{kB}} = 90^\circ)$ is a measure of the amplitude of the angle-dependent oscillations. In Fig. 5.6, the plots for CO (red) and N_2 (blue) can be seen, showing a value of 1 at collision energies below ≈ 40 K, which indicates that, at those energies the orientation control is lost.

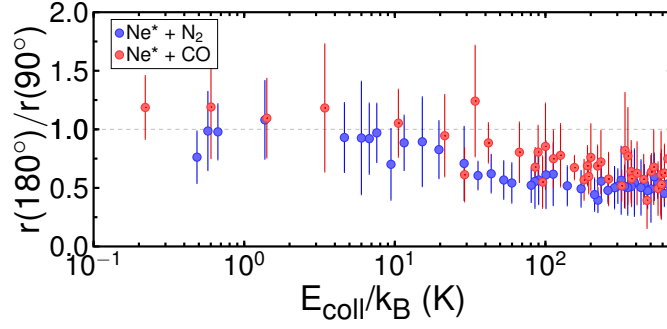


Figure 5.6 – Steric effect for N₂ (blue symbols) and CO (red symbols), defined as the ratio between the reactivities $r(\theta_{\text{KB}} = 90^\circ)$ and $r(\theta_{\text{KB}} = 180^\circ)$, as a function of energy.

In contrast, the value is closer to 0.5, owing to the fact that $r(\theta_{\text{KB}})$ strongly depends on the orientation angle. One may suggest that the steric effect in the case of CO appears at higher collision energy, but a definitive statement is impossible based on the present data. The same has also been shown in the Ne* + Ar reaction and it is due to a dynamic reorientation of the Ne* as it approaches the secondary reactant at low speed.

In the case of chemi-ionizations with molecules, we observe an angle-dependent yield of the bare ion as shown in Fig. 5.3. For N₂, it was found that the observed ion yield of bare N₂⁺ ions largely exceeded those from the rare gas reactions in the previous section. This was explained by including an additional channel, AI followed by predissociation (PD). Compared to the rare gas reactions as shown in Fig. 4.6, we can assume that PI is independent of the Ne* orientation and the angle-dependent formation of bare ions is interpreted as the result of predissociating AI complexes from vibrationally excited states. Predissociation occurs on a time scale faster than the extraction time of the TOF-MS. We can only distinguish between [Ne-X]⁺ and X⁺, not the ions between AI+PD and PI.

To quantify the angle dependence in the red trace in Fig. 5.3 (b) and (d), their dynamics in the analysis are used by the following relation between the observed X⁺ signal and the true ion yields for PI and AI as a linear combination of the PI and AI-PD:

$$I_{X^+}(\theta_{\text{KB}}, E_{\text{coll}}) = w_{\text{pd}}(E_{\text{coll}}) I_{\text{NeX}^+}(\theta_{\text{KB}}, E_{\text{coll}}) + I_{\text{PI}}(E_{\text{coll}}), \quad (5.1)$$

where $w_{\text{pd}}(E_{\text{coll}})$ is the fraction of NeX⁺ ions that predissociate into X⁺, and $I_{\text{PI}}(E_{\text{coll}})$ is the fraction of X⁺ ions that are formed through direct PI. From the $w_{\text{pd}}(E_{\text{coll}})$, we can easily find the predissociation probability:

$$P_{\text{pd}}(E_{\text{coll}}) = \frac{w_{\text{pd}}(E_{\text{coll}})}{1 + w_{\text{pd}}(E_{\text{coll}})} \quad (5.2)$$

P_{pd} is independent with the magnetic field direction, but varies with collision energy. The

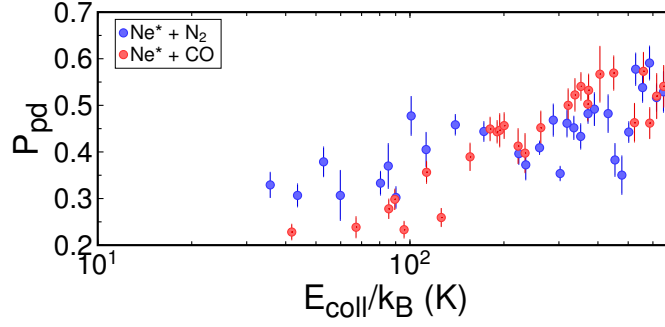


Figure 5.7 – Predissociation probability P_{pd} of the AI products $[\text{Ne-X}]^+$, obtained by fitting Eq. 5.2 to the experimental data, for $\text{X} = \text{CO}$ (red) and $\text{X} = \text{N}_2$ (blue).

actual reactivity between PI and AI then becomes

$$R(\theta_{\text{kB}}) = \frac{I_{\text{AI}}}{I_{\text{PI}}} = \frac{I_{\text{NeX}^+}(\theta_{\text{kB}}) + w_{\text{pd}} I_{\text{NeX}^+}(\theta_{\text{kB}})}{I_{\text{X}^+}(\theta_{\text{kB}}) - w_{\text{pd}} I_{\text{NeX}^+}(\theta_{\text{kB}})}, \quad (5.3)$$

This approximation only works when the steric effect is observable at high collision energies. Below ≈ 40 K, we lose the steric control, and this formalism no longer permits the definition of the orientation angle, and thus the separation of the ion signals into AI and PI.

Thus, we write the low-energy reactivity directly as the ratio between the ion yields

$$R_{\text{lowE}} = I_{\text{NeX}^+}(\theta_{\text{kB}}) / I_{\text{X}^+}(\theta_{\text{kB}}). \quad (5.4)$$

The resulting probability for predissociation, P_{pd} , is shown for the N_2 - and CO -data as a function of collision energy in Fig. 5.7. It reveals the same upward trend with increasing collision energy for CO (red) and N_2 (blue) in the range of 0.3–0.6. Figure 5.8 shows the PD-corrected reactivities as a function of collision energy, after integration over all angles. These data show a similar trend as observed in Fig. 5.5, namely, the probability for AI and PI is nearly the same at all energies in the case of N_2 , but the probability for AI is about two times higher than that for PI at low energies in the CO case.

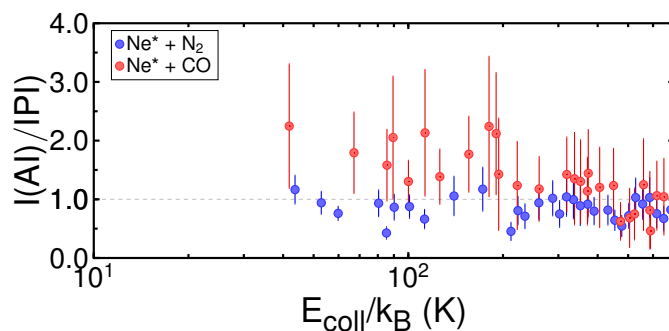


Figure 5.8 – Ratio of the angle-integrated AI and PI yields for N₂ (blue) and CO (red). In contrast to the data in Fig. 5.5, these data take into account predissociation, using Eq. 5.3.

Based on the predissociation model, the actual reactivity surface AI/PI can be extracted from the original data in Fig. 5.3. The actual AI/PI reactivity needs to be divided into two parts: the ion yield ratio $R_{\text{lowE}} < 40$ K and the reactivity $R = I_{\text{AI}}/I_{\text{PI}} > 40$ K. Panel in Fig. 5.9 (a) (c) show the experimental reactivity surfaces between AI and PI for Ne* + CO, N₂ reactions respectively. The corresponding fitted surfaces are also given. At low temperatures (< 40 K), the Monte-Carlo search procedure depends on Eq. 3.8 for traces from the AI and PI channels and on Eq. 3.10 for the reactivity with respect to θ_{KB} , whereas at high temperatures, this search procedure only depends on Eq. 3.10. The experimental reactivity surfaces show that, above 40 K, all these reactivities strongly depend on θ_{KB} , and are nearly independent of the collision energy. As the orientation angle θ_{KB} is varied from 0° to 360° , the Ne* + N₂ reaction oscillates between being PI-dominated and AI-dominated, whereas the AI channel dominates in the Ne* + CO reactions. At low temperatures, the AI and PI cross sections tend to be the same for Ne* + CO reaction, whereas PI dominates in the Ne* + N₂ reaction despite the angle-dependent oscillations.

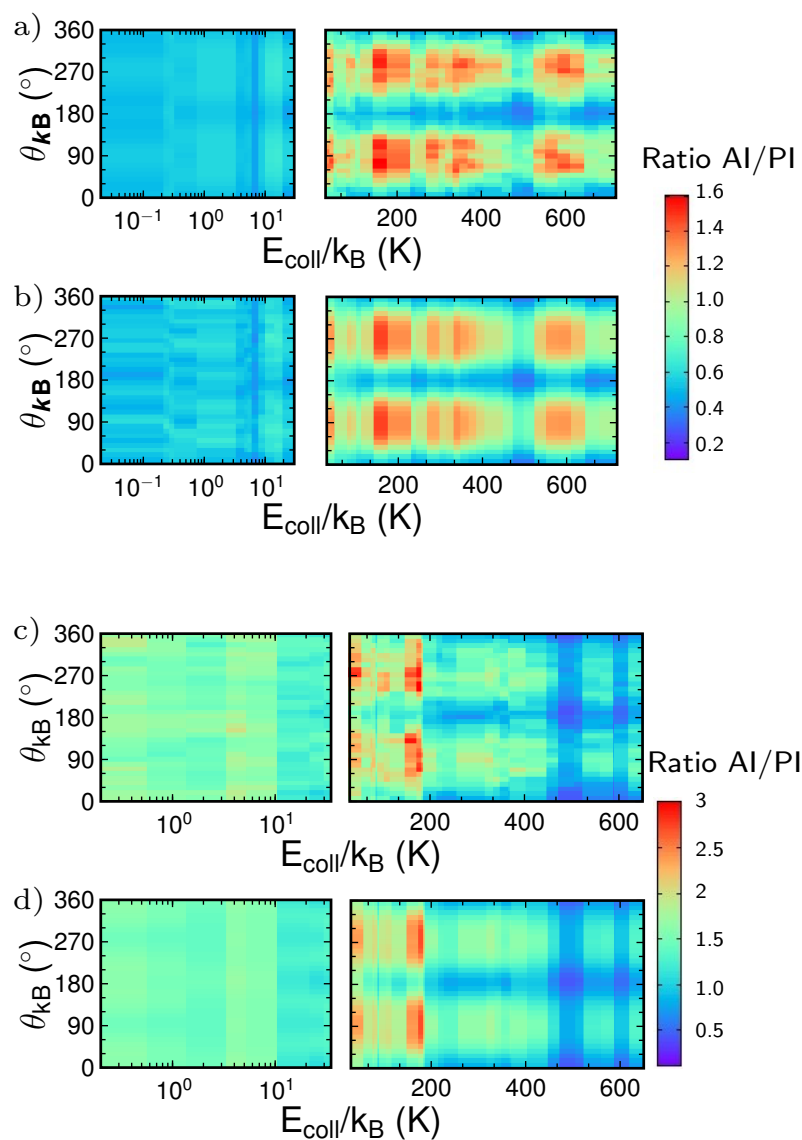


Figure 5.9 – Experimental reactivity: for (a) the $\text{Ne}^* + \text{N}_2$ reaction and (c) the $\text{Ne}^* + \text{CO}$ reaction as a function of collision energy. Fitted reactivity as a function of collision energy for (b) the $\text{Ne}^* + \text{N}_2$ reaction and (d) the $\text{Ne}^* + \text{CO}$ reaction. In all cases, the left side shows the energy range of 0.3–40 K, and the right side shows the range of 40–700 K. (Left) Raw data. (Right) Actual AI/PI obtained through a fit using Eq. 5.3.

Ω specific reactivities are shown in Fig. 5.10 for the Ne* + CO reaction (panels a-c) and the Ne* + N₂ reaction (panels d-f) for $\Omega = 0, 1$, and 2 as labeled in the respective panels. In each case, the left panel for $E_{\text{coll}} < 40$ K is obtained from R_{lowE} , while the right panel takes into account predissociation by determining AI and PI contributions using Eq. 5.3. Several striking observations can be made here:

- (1) The $\Omega = 0, 1$ reactivities are nearly zero at high energies and rise to ≈ 0.5 for the Ne* + N₂ reaction and to 2 for the Ne* + CO reaction below 40 K, and the $\Omega = 2$ reactivity is approximately 2.5 for the Ne* + N₂ reaction and approximately 3 for the Ne* + CO reaction at high energies.
- (2) Below ≈ 40 K, $\sigma_{AI}^{\Omega} > \sigma_{PI}^{\Omega}$ for the Ne* + CO reaction, and $\sigma_{AI}^{\Omega} < \sigma_{PI}^{\Omega}$ for the Ne* + N₂ reaction.

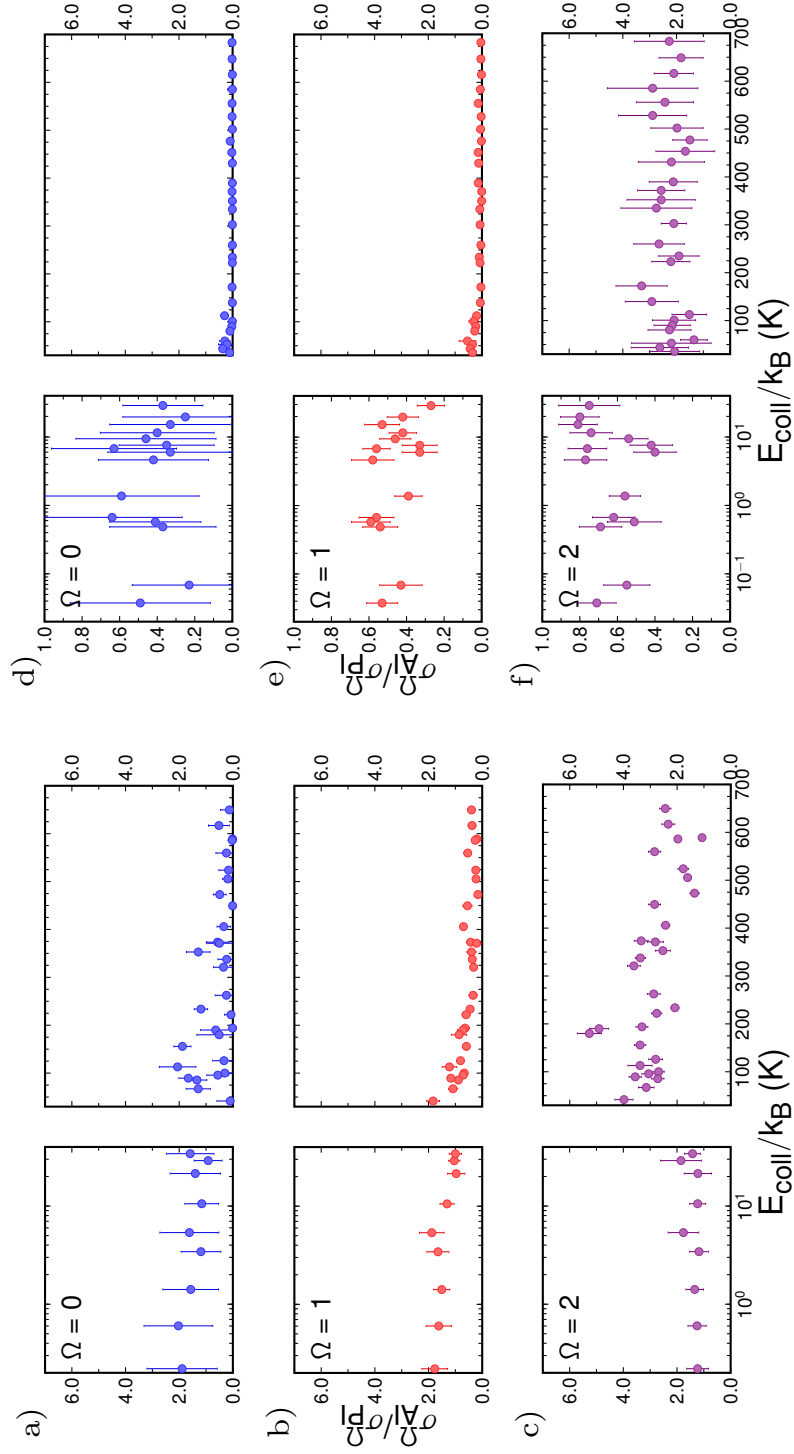


Figure 5.10 – Reaction cross section ratios for $\Omega = 0, 1$, and 2 (a)–(c) for the $\text{Ne}^* + \text{CO}$ reaction and (d)–(f) for the $\text{Ne}^* + \text{N}_2$ reaction. The error bars represent the one standard deviations of the cross-section histograms obtained from the fit.

5.4 Reaction dynamics of the Ne* + N₂, CO reactions

It has been observed in the past that the energy transfer from the Ne* atoms to molecules can lead to substantial vibrational excitation of the resulting ions.[134] It is reasonable to assume that the associative ionization reaction leads to complexes in vibrationally excited states but these are not stable and predissociate by vibrational energy transfer from the molecular bond to the [Ne-X]⁺. The results show three principal reaction channels: PI (yielding products Ne(¹S) + X⁺), AI (yielding Ne-X⁺ complexes) and AI followed by predissociation (also producing Ne(¹S) + X⁺). Their dependence on the collision energy and the orientation of Ne* was studied by orienting Ne* in a magnetic field and by recording the products in a TOF-MS.

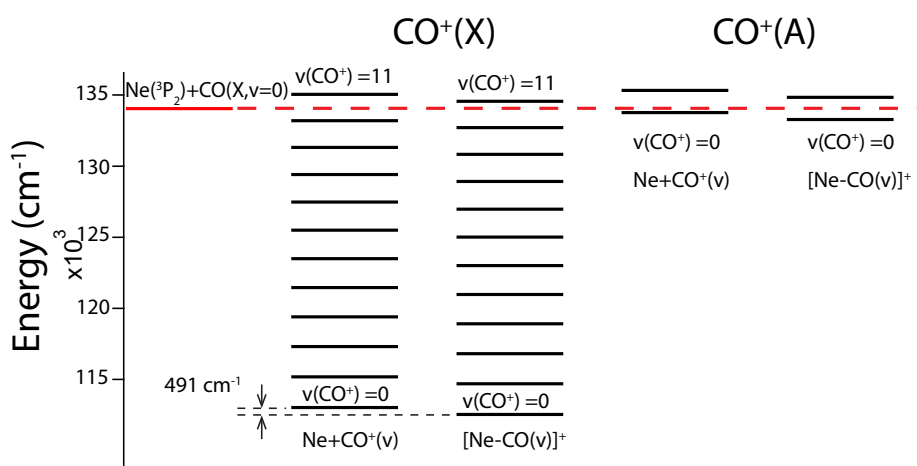


Figure 5.11 – Relevant energy levels for the Ne* + CO reaction. Successive vibrational levels of CO are indicated in each case. For both accessible electronic states, the levels of the bare ion are shown on the left, and those of the complex are shown on the right.

Here, N₂ and CO are isoelectronic molecules with similar properties in many respects.[133] To understand the difference between these two reactions, Fig. 5.11 and Fig. 5.12 present the vibronic structures of these two product ions CO⁺ and N₂⁺, respectively. The ionization potential of CO is 14.014 eV, and that of N₂ is 15.581 eV, corresponding to accessible energies of 20986.54 cm⁻¹ and 8347 cm⁻¹, respectively in the case of PI with Ne* (*E*_{exited} = 16.6 eV). The binding energies of Ne(¹S)-N₂⁺ and Ne(¹S)-CO⁺ are estimated to be 300 cm⁻¹, [134] and 491 cm⁻¹, respectively.[139]. The vibrational frequency of N₂⁺ is 2207 cm⁻¹ while the vibrational frequency of CO⁺ is 2214 cm⁻¹. [30]

In both cases, the complex's binding energy is lower than the vibrational frequency of the molecular ion which means that a single quantum of vibrational excitation produces a pre-dissociating complex ion. Because of the lower ionization energy, in the case of CO, the vibrational levels up to *v* = 10 (133202 cm⁻¹) are accessible. And the accessible state is up to *v* = 3 in the case of N₂⁺. However, the binding energy of the complex is not known with sufficient accuracy such that we don't know whether *v* = 4 is accessible or not in the present experiment.

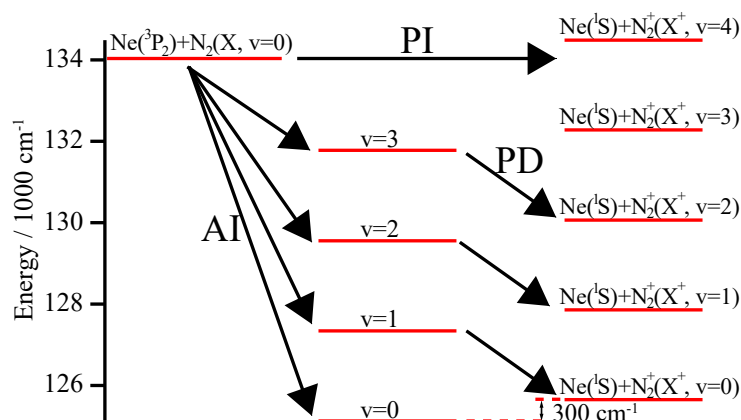


Figure 5.12 – Relevant energy levels for the $\text{Ne}^* + \text{N}_2$ reaction. AI, PI, and PD stand for associative ionization, Penning ionization, and predissociation, respectively.

The major difference between CO and N_2 is found in the electronic structure: the first excited state of N_2^+ is $A^2\Pi_{ui}$, which lies 9166 cm^{-1} , or 134826 cm^{-1} above the N_2^+ ground state. With the energy of Ne^* being 133880 cm^{-1} , this state is not accessible in our experiment even at the highest collision energies. In contrast, the first electronically excited state of CO is $A^2\Pi_i$ lies at an energy of 20733 cm^{-1} above the ionic ground state and at an energy of 133755 cm^{-1} above the ground state of neutral CO. As shown in Fig. 5.11 this opens two additional reaction channels, namely AI and PI forming $\text{Ne-CO}^+(A)$ and bare $\text{CO}^+(A)$, respectively. Assuming that the Ne-CO^+ binding energy is similar for $\text{CO}^+(X)$ and for $\text{CO}^+(A)$, only the vibrational ground state is accessible, ruling out the possibility of predissociation after AI.

As a consequence, and unlike in the case of the rare gases or N_2 , a detailed analysis of the reactivity in the case of CO must include the channels leading to electronically excited ions. The present experiment at this time can not distinguish between the formation of the two electronic states. But by assuming that electronic predissociation, corresponding to the process $\text{Ne-CO}^+(A, v=0) \rightarrow \text{Ne} + \text{CO}^+(X, v)$, is slow on the experimental time scale, the different observations of the AI/PI ratios in N_2 and CO can be explained by the fact that the AI products with electronically excited CO^+ do not predissociate at all, and by invoking a threshold dependence in the different cross sections leading to $\text{CO}^+(A)$ and $\text{CO}^+(X)$. These assumptions imply that in the range of collision energies below $\approx 200\text{ K}$ the formation of electronically $\text{CO}^+(A)$ and $\text{Ne-CO}^+(A)$ gain in relative importance, and the absence of PD explains the overall increase of the relative contribution of AI.

However this simplified model makes assumptions that demand further testing: 1. it is assumed that PI is independent of the Ne^* orientation, in analogy with the rare gases, and for both molecules studied here, independent of the final electronic state of the ion. Beyond the observations with the rare gases, the present experiment does not currently permit to test this assumption experimentally, and theoretical support is required. 2. Detection of only the final product ions does not permit the positive confirmation that $\text{CO}^+(A)$ is formed. Penning

ionization electron spectra are required for this, where the excited state would appear in the form of slow Penning electrons. 3. While not critical for the present analysis, the Penning electron spectra will rely on the time scale for electronic predissociation which at present is not known. This aspect will also have to be addressed both experimentally and theoretically.

6 Preparation of oriented ND₃ molecules

In this chapter, a new apparatus is presented which is utilized to prepare oriented ND₃ molecules in preparation of scattering experiments with Ne*. Here, we present preliminary measurements to demonstrate the first step, that is, the state-filtering and preparation of an oriented sample. Molecules are state-selected using an electrostatic hexapole guide, and the orientation is probed by REMPI, similar to the case of Ne* in the previous chapter. Section 6.1 gives an introduction to the previous studies on which this work is built and which motivates the present studies. Section 6.2 details the experimental apparatus used to determine the orientation of ND₃. The results are described and analyzed in Section 6.3.

6.1 Introduction

In the past, merged-beam studies of Ne* + ND₃/NH₃ reactions were performed in our laboratory where the branching ratio $\frac{[\text{NH}_2]^+}{[\text{NH}_2]^+ + [\text{NH}_3]^+}$, as shown in Fig. 6.1, was independent of collision energy.[15] A particularly interesting aspect of this system is the hypothesis that the two reaction channels are believed to directly reflect the relative arrangement of the ammonia molecule and Ne* during the reaction. Indeed, if the Ne* is lined up with the lone pair on ammonia, then PI dominates whereas an approach of Ne perpendicular to the *c*3 axis predominantly leads to dissociative ionization. Therefore, we would expect the branching ratio is orientation dependent if we can manipulate the orientation of reagents in these reactions.

Recently, our group controlled the orientation of Ne* with respect to ND₃ in a crossed beam experiment and it was found that the reactivity was completely insensitive to the Ne* orientation and collision energy at collision energies of 370–520 cm⁻¹. [141] It was speculated that a change in the branching between PI and DI should be observed as the collision energy is reduced, but this was not observed, presumably because the few occupied rotational states turned ammonia into an isotropic object, suppressing any steric preference. This is rationalized by considering that the branching into DI or PI results from the propensity to form an ND₃ ion in one of two different electronic states. Both these states are formed in a process that ultimately is PI, but one of them is dissociative while the other is not. Unlike the previous

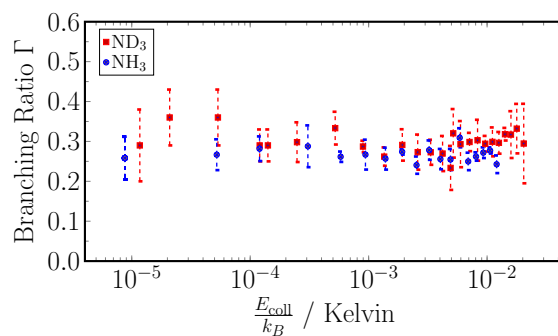


Figure 6.1 – Experimental branching ratios as a function of collision energy in the Ne* + NH₃ reaction (blue circles) and Ne* + ND₃ reaction (red squares). (Reproduced from Ref. [140])

samples described in this thesis, the branching does not depend on the orientation of the Ne* orbitals but on the ammonia molecule. Hence, the absence of steric preference with respect to orientation of Ne* is not surprising.

In order to understand the underlying dynamics better and to observe the steric effect nonetheless, we present the first step toward an experiment in which ammonia molecules are state selected and then actively oriented in an electric field which can be set parallel or perpendicular to the relative velocity of the reactants.

6.2 Experimental apparatus

Two essential requirements need to be satisfied in order to prepare an oriented ND₃ sample: (1) a beam of polarized molecules, and (2) a homogeneous electric field to control a polarized sample and to fix its orientation. Based on these requirements, we set up an experimental apparatus as sketched in Fig. 6.2 (a). A pulsed supersonic beam of ND₃ (5% seeded in Ne expanded through a general valve series 9; stagnation pressure 1.5 bar, 20 Hz) is skimmed (diameter 2 mm) and enters the main apparatus from the left side of the figure. The molecules propagate through a 30-cm hexapole guide, built from three 3D-printed and electroplated segments,[142] operated with a potential difference of 20 kV between adjacent rods.

Figure 6.2 (c) shows one of the guide segments that was 3D-printed (Formlabs Form 2) as a single poly(methylmethacrylate) piece. This allows the entire structure to be a single plastic piece, and no alignment is required. Figure 6.2 (b) shows a front view where it can be observed how the segment is selectively electroplated to produce two separated parts: two sets of electrically independent electrodes and an insulating base.

To orient and detect the reaction products, we use a rotatable TOF-MS, shown on the right side of the figure. Unlike the setup used for the magnetic orientation, a setup with electrodes arranged around the point of interaction did not work because their presence would significantly distort the electric fields of the MS. Instead, the repeller and extraction plates of a Wiley-McLaren type mass spectrometer[117] are used here first for the orientation and then, by rapidly switching to a higher potential, also for the mass analysis. The control of the direction of the orientation relative to the particle velocities is achieved by rotating the mass spectrometer around the crossing point of the two beams. A mesh is attached to the repeller plate of the mass spectrometer in order to allow the beams to enter the collision zone from a wide range of angles, thus being able to cover ammonia orientations from -90° to +90° relative to the primary beam. The pivot point for the rotation is shown as a blue circle between the first and second plate of the MS.

In the first step presented here, (2+1) resonance-enhanced multiphoton ionization (REMPI) spectroscopy is used to probe ammonia molecules and assess the degree of orientation present in the sample. For this, a laser beam is focused inside the mass spectrometer at the rotation center of the mass spectrometer. A Laser pulse energy of ~ 5 mJ/pulse is used. The well-characterized $B(\nu_2) \leftarrow X$ two-photon transition around 160 nm is chosen here, making use of the vibronic selection rules that permit excitation of only odd numbers of vibrational quanta in the ν_2 umbrella mode from the upper component of the ground state-inversion doublet (i.e., the low-field seeking states) and of only even vibrational levels from the lower component. The choice of appropriate rotational states then adds a dependence of the intensity on the direction of the laser polarization relative to the electric field, thus allowing the determination of the M_J specific populations, in analogy to the procedure used for the characterization of Ne* described in Chapter 3. Charged products are extracted into the TOF-MS and counted as a function of the direction of laser polarization and of the electric field. The laser polarization

is controlled through a $\lambda/2$ plate and a BBO polarizer. The experiments are performed in the following way: the electric field direction is kept perpendicular to the beam velocity vector while the polarization vector of the laser is tuned by a $\lambda/2$ wave plate. Next, the MS is rotated by 90° such that the E field is parallel to the beam velocity, and the polarization of the laser is controlled again as before. These two independent geometries are used to obtain the alignment moments by measuring the REMPI ions in the mass spectrometer.

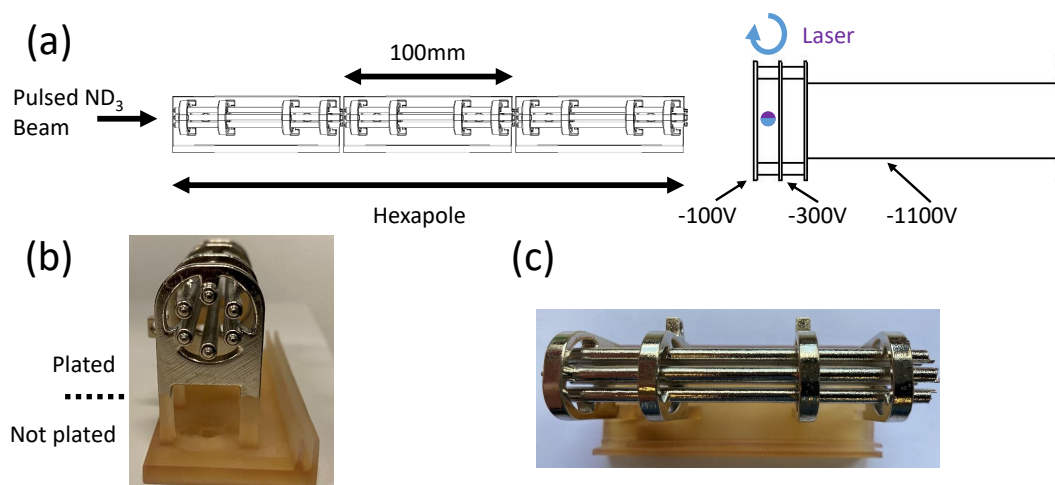


Figure 6.2 – (a) Side view of the apparatus used for the orientation of ND₃. Molecules are injected from the left. (b) Front view of the printed hexapole element. The upper part is metal plated while the lower part is the electrically insulating base. (c) Top view of a single guide element.

6.3 Experimental result

A polarized sample can be identified by the angle-dependent REMPI intensities, and by the absence of certain rotational states from the spectrum. Indeed, the hexapole has different transmissions not only for the two tunneling components of ammonia but also for the different rotational states, as can be seen from the calculation of the Stark effect outlined in Chapter 2.[88, 143] Thus, the comparison of REMPI spectra of background molecules and guided molecules, as well as the angle-dependent spectra described above should provide a reliable assessment of the degree of orientation achieved with this setup. Representative sections of the $B(v_2 = 5) \leftarrow X(v'_2 = 0)$ transition are displayed in Fig. 6.3. The top spectrum shows guided molecules (recorded at 20 kV on the guide), middle spectrum shows the unguided beam (recorded at 0 V on the guide), and bottom spectrum shows a calculation obtained with PGOPHER,[144] using a rotational temperature of ~ 15 K. The intensities are normalized to the $|1_0\rangle \rightarrow |3_1\rangle$ transition at 63029.19 cm^{-1} which required the background measurement to be multiplied by 1.5. Transitions in the simulated spectrum are labeled by the initial rotational state as J_K , and a full assignment is given in Table 6.1.

The comparison of the red and blue traces in Fig. 6.4 shows that the hexapole focuses on low-field seeking states while leaves the non-polar $J_K = 0_0$ state unchanged. The detailed comparison shown in Fig. 6.3 furthermore shows that individual rotational states are affected differently, as expected owing to the different M_J components for different J values. These spectra give a first indication that a polarized sample is produced.

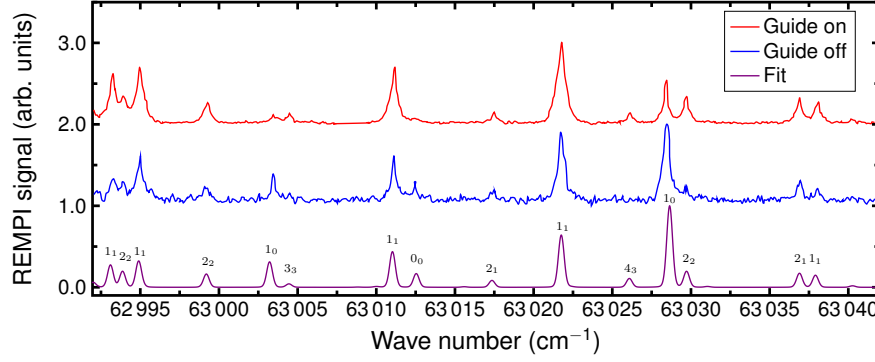


Figure 6.3 – Experimental (red and blue) and theoretical (black) REMPI spectra. The top spectrum was obtained when the guide voltage difference was 18 kV, the middle spectrum was recorded with the guide switched off. The theoretical spectrum was calculated using the PGOPHER software, assuming a rotational temperature of 15 K.

Table 6.1 – Excited state and ground state for selected transitions in the (2 + 1) REMPI spectrum of ND₃

Two-photon energy (cm ⁻¹)	Excited state (J_K)	Ground state (J_K)
62993.63	1 ₀	1 ₁
62994.42	3 ₃	2 ₂
62995.44	2 ₂	1 ₁
62999.73	2 ₁	2 ₂
63003.75	2 ₁	1 ₀
63004.97	3 ₂	3 ₃
63011.55	2 ₀	1 ₁
63012.58	2 ₁	0 ₀
63017.89	3 ₀	2 ₁
63022.3	3 ₂	1 ₁
63026.7	5 ₃	4 ₃
63029.19	3 ₁	1 ₀
63030.25	4 ₃	2 ₂
63037.46	4 ₂	2 ₁
63038.46	3 ₀	1 ₁

For further verification, we record the REMPI spectra at different orientations with the guide fixed at 18 kV, as shown in Fig. 6.5. The four spectra correspond to the following cases: 1. The electric field is parallel to the molecular beam while the laser polarization is parallel or perpendicular to the electric field (shown in panel a of Fig. 6.5). 2. The electric field is perpendicular to the molecular beam and the laser polarization is parallel or perpendicular to the electric field (panel b).

There are clear differences in the intensities between parallel and perpendicular polarization. Here, the case of $\theta_{ke} = 0^\circ$ and $\theta_{Ee} = 90^\circ$ is equivalent to the case of $\theta_{ke} = 90^\circ$ and $\theta_{Ee} = 0^\circ$ and

indeed the REMPI intensities in these cases are similar.

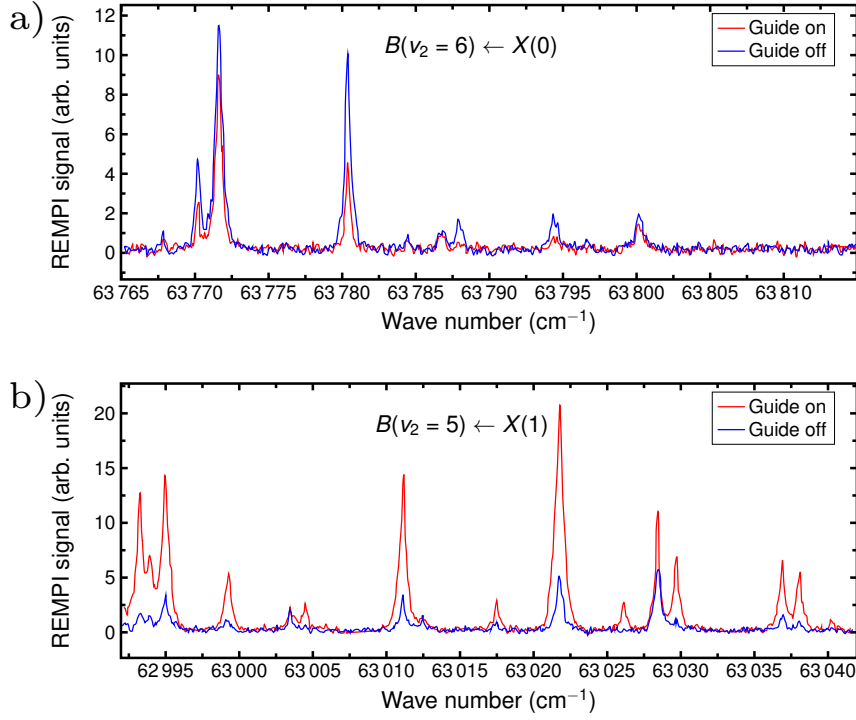


Figure 6.4 – (a),(b) REMPI spectra recorded through the $B(\nu_2 = 6)$ and $B(\nu_2 = 5)$ vibrational level, respectively. Blue traces, signal of the pure supersonic expansion; red traces, signal from guided molecules.

For a more detailed analysis we selected the $B(\nu_2 = 5, J = 3, K = 2) \leftarrow X(\nu' = 0, J' = 1, K' = 1)$ transition at 63022.3 cm^{-1} to be probed as a function of relative angles. Figs. 6.6 (a) and (b) show the intensities of this transition when the orientations are parallel and perpendicular to the molecular beam, respectively. In each case, the intensity was recorded as the laser polarization was rotated by 360° in steps of 10° . Maximum intensity is observed when the laser polarization ϵ is perpendicular to the electric field direction \vec{E} while the minimum is reached when ϵ is parallel to \vec{E} . Here the electric field strength for the orientation in all these measurements is $|\vec{E}| = 200 \text{ V/cm}$.

To quantify the polarization we determine the populations of different M_J states of the specific rotational state chosen here, using again the alignment parameters $A_q^{(k)}(J)$ as described for the case of $\text{Ne}(^3P_2)$. The REMPI intensity of a transition in an oriented ND₃ sample is written as

$$I(\theta_{ke}) = I_0 \left[1 + \sum_{k=1}^{2J} s_k(J, J', \lambda) P_k(\cos \theta_{ke}) A_q^{(k)}(J) \right] \quad (6.1)$$

where the detection sensitivities s_k are $s_1 = s_3 = 0$, $s_2 = -\frac{2}{7}$ and $s_4 = \frac{8}{245}$, respectively, as given in Ref. [119]. Here the initial state of the target transition is $|1, 1\rangle$, and we can define the

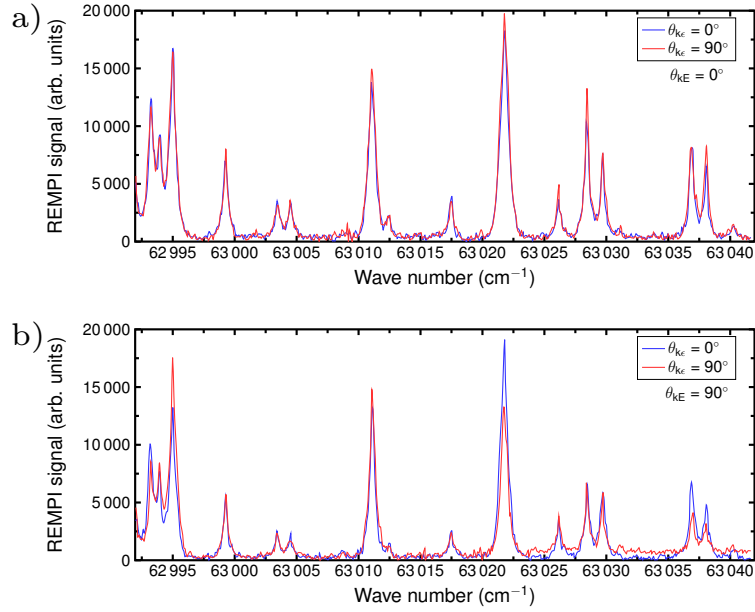


Figure 6.5 – Experimental (2+1) REMPI spectra of ND₃ recorded with different relative directions to the laser polarization ϵ , electric field axis \vec{E} , and beam velocity \vec{k} . Panels a and b were recorded with the electric field parallel and perpendicular to the molecular beam, respectively. In both panels the blue (red) spectrum was obtained with the laser polarization aligned parallel (perpendicular) to the electric field axis.

populations, using the density matrix elements, as $\rho_{0,0} = p$, $\rho_{1,1} = 1 - p$. Setting $\rho_{-1,-1} = 0$ is justified by the non-guidability of the high-field seeking states from the lower component of the inversion doublet and by assuming that no transitions from those states to odd vibrational levels in the B state are allowed even in the presence of the weak electric field used for the orientation. We note that this choice already implies that a polarization is present, because no negative M_J states are populated.

Thus, the alignment parameters can be simplified into

$$A_0^{(1)} = \frac{1}{\sqrt{6}}(1 - p) \quad (6.2)$$

$$A_0^{(2)} = -\frac{1}{2}p - \frac{1}{2} \quad (6.3)$$

$$A_0^{(3)} = \frac{1}{\sqrt{6}}(1 - p) \quad (6.4)$$

$$A_0^{(4)} = \frac{1}{12}(5p - 2) \quad (6.5)$$

Using this formalism, we can fit the population p to calculate the angle-dependent intensity, as shown with solid lines in Fig. 6.6. From the two independent fits, we find the values of $p = 0$ (panel a) and $p = 0.4562 \pm 0.27264$ (panel b), respectively. The values of p should be

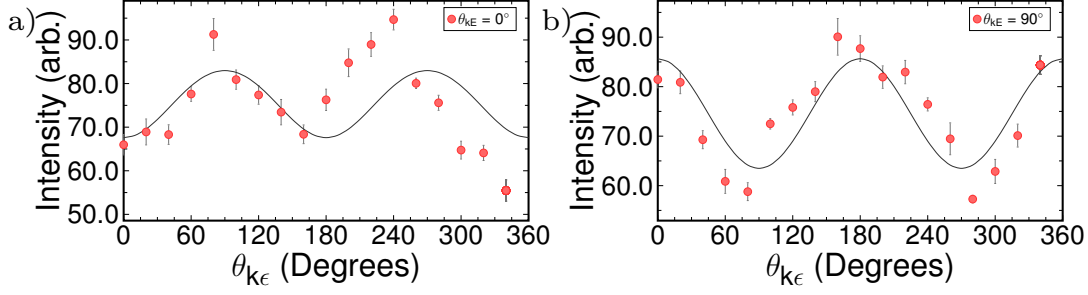


Figure 6.6 – (2+1) REMPI signal at 63022.3 cm^{-1} of ND₃ as a function of angle between the laser polarization ϵ and the beam velocity \vec{k} when the angle between the electric field \vec{E} and the beam velocity \vec{k} is 0° (a), and 90° (b).

identical in the two measurements since the guiding and state selection were the same for both measurements, provided that the samples adiabatically followed the electric field. The fact that the fits produce different results is either an indication of M_J mixing between the end of the guide and the interaction zone or a result of the true error margin from these preliminary measurements.

From the angle dependent REMPI spectra, the following two observation are made:

- The angle dependence in the line intensity confirms that the electrostatic state filtering of ammonia indeed produces a polarized sample.
- The fits do not allow us to make a definitive statement on the populations of the individual M_J states but they indicate that the populations indeed are similar.

For the present system with only two populated states ($M_J = 0$ and 1) the angle dependence of the intensity is independent of the relative populations, and changing p only changes the amplitude of the oscillation. Overall, we have demonstrated that using this setup indeed we indeed are capable of preparing an oriented sample of ND₃ that can now be used in scattering studies.

7 Conclusion and outlook

This thesis demonstrates an apparatus including a merged (or crossed) beam setup and the external magnetic field manipulation for studying reaction dynamics. Here we focus on the Penning ionization between Ne^* and other ground-state reagents (e.g., Ar, Kr, Xe, N_2 and CO) at collision energies of 0.02–1000 K. We accurately manipulated two parameters in the reactions: collision energy and the Ne^* orientation. The angular momentum \vec{J} of polarized Ne^* atoms is confirmed to be oriented in controlled magnetic fields. The steric effect is presented by the reactivity, e.g., the ratio between Penning and associative ions, as a function of Ne^* orientation.

In these crossed molecular beam experiments, we investigate the stereodynamics of the $\text{Ne}^* + \text{Rg}$ reactions ($\text{Rg} = \text{Ar}, \text{Kr}$ and Xe) at collision energies between 320 cm^{-1} and 500 cm^{-1} . The experimental data can be interpreted by the relation between the collision energy and the Ω specific cross sections ratio $\sigma_{\text{AI}}/\sigma_{\text{PI}}$. Here two postulated mechanisms (radiative and exchange mechanisms) perfectly explain the experimental data.

The second part of the thesis discusses the low-energy stereodynamics studies of the $\text{Ne}^* + \text{Ar}, \text{N}_2, \text{CO}$ reactions over collision energies of 0.06–700 K. In these reactions, we find that at low collision energies, we lose the steric control of Ne^* at $\approx 40 \text{ K}$ because of reorientation. Compared to the $\text{Ne}^* + \text{Rg}$ reactions, a substantially lower probability for associative ionization was observed for CO and N_2 and it is explained by the predissociation in the reactions. Next, we propose a simple model to extract the predissociation efficiency from the excited AI ions into PI ions after collisions and we find that NeX^+ ($\text{X} = \text{CO}$ and N_2) has a probability of 30%–60% to predissociate into X^+ after collisions.

In addition to the magnetic orientation in gas-phase chemical reactions, the final chapter presents a new experimental apparatus that is used to orient a polar molecule with Ne^* in a rotatable magnetic field. The orientation of ND_3 was probed using $(2 + 1)$ REMPI spectroscopy. ND_3 was found to be oriented in a static electric field at $|\vec{E}| = 200 \text{ V/m}$. The project will continue by finalizing the orientation characterization and then by performing crossed experiments of Ne^* with oriented ND_3 .

Bibliography

- [1] E. Herbst and J.T. Yates Jr. Introduction: astrochemistry. *Chem. Rev.*, 113:8707–8709, 2013.
- [2] R.V. Krems. Cold controlled chemistry. *Phys. Chem. Chem. Phys.*, 10(28):4079–4092, 2008.
- [3] W. Vassen, C. Cohen-Tannoudji, M. Leduc, D. Boiron, C.I. Westbrook, A. Truscott, K. Baldwin, G. Birkel, P. Cancio, and M. Trippenbach. Cold and trapped metastable noble gases. *Rev. Mod. Phys.*, 84(1):175, 2012.
- [4] J. Weiner, V. S. Bagnato, S. Zilio, and P.S. Julienne. Experiments and theory in cold and ultracold collisions. *Rev. Mod. Phys.*, 71(1):1, 1999.
- [5] G. Quemener and P.S. Julienne. Ultracold molecules under control! *Chem. Rev.*, 112(9):4949–5011, 2012.
- [6] O. Dulieu and A. Osterwalder(Editors). *Cold chemistry: molecular scattering and reactivity near absolute zero*. Royal Society of Chemistry, 2017.
- [7] N. Balakrishnan. Perspective: Ultracold molecules and the dawn of cold controlled chemistry. *J. Chem. Phys.*, 145(15):150901, 2016.
- [8] W.E. Perreault, N. Mukherjee, and R.N. Zare. Cold quantum-controlled rotationally inelastic scattering of HD with H₂ and D₂ reveals collisional partner reorientation. *Nat. Chem.*, 10(5):561–567, 2018.
- [9] K.K. Ni, S. Ospelkaus, M.H.G. De Miranda, A. Pe’Er, B. Neyenhuis, J.J. Zirbel, S. Kotochigova, P.S. Julienne, D.S. Jin, and J. Ye. A high phase-space-density gas of polar molecules. *Science*, 322(5899):231–235, 2008.
- [10] J. Toscano, H.J. Lewandowski, and B.R. Heazlewood. Cold and controlled chemical reaction dynamics. *Phys. Chem. Chem. Phys.*, 22(17):9180–9194, 2020.
- [11] A.B. Henson, S. Gersten, Y. Shagam, J. Narevicius, and E. Narevicius. Observation of resonances in Penning ionization reactions at sub-Kelvin temperatures in merged beams. *Science*, 338(6104):234–238, 2012.

Bibliography

- [12] A. Von Zastrow, J. Onvlee, S.N. Vogels, G.C. Groenenboom, A. Van Der Avoird, and S.Y.T. Van De Meerakker. State-resolved diffraction oscillations imaged for inelastic collisions of NO radicals with He, Ne and Ar. *Nat. Chem.*, 6(3):216–221, 2014.
- [13] C. Naulin and M. Costes. Experimental search for scattering resonances in near cold molecular collisions. *Int. Rev. Phys. Chem.*, 33(4):427–446, 2014.
- [14] S.D.S. Gordon, J.J. Omiste, J. Zou, S. Tanteri, P Brumer, and A. Osterwalder. Quantum-state-controlled channel branching in cold $\text{Ne}(^3P_2) + \text{Ar}$ chemi-ionization. *Nat. Chem.*, 10(12):1190–1195, 2018.
- [15] J. Jankunas, B. Bertsche, K. Jachymski, M. Hapka, and A. Osterwalder. Dynamics of gas phase $\text{Ne}^* + \text{NH}_3$ and $\text{Ne}^* + \text{ND}_3$ Penning ionisation at low temperatures. *J. Chem. Phys.*, 140(24):244302, 2014.
- [16] P.G. Jambrina, J. Croft, H. Guo, M. Brouard, N. Balakrishnan, and F.J. Aoiz. Stereodynamical control of a quantum scattering resonance in cold molecular collisions. *Phys. Rev. Lett.*, 123(4):043401, 2019.
- [17] J.J. Omiste, J. Floß, and P. Brumer. Coherent control of Penning and associative ionization: Insights from symmetries. *Phys. Rev. Lett.*, 121(16):163405, 2018.
- [18] W.E. Perreault, N. Mukherjee, and R.N. Zare. Quantum control of molecular collisions at 1 Kelvin. *Science*, 358(6361):356–359, 2017.
- [19] A. Klein, Y. Shagam, W. Skomorowski, P.S. Żuchowski, M. Pawlak, L.M.C. Janssen, N. Moiseyev, S.Y.T. van de Meerakker, A. van der Avoird, C.P. Koch, and E. Narevicius. Directly probing anisotropy in atom–molecule collisions through quantum scattering resonances. *Nat. Phys.*, 13(1):35–38, 2017.
- [20] R.D. Levine. *Molecular reaction dynamics*. Cambridge University Press, 2009.
- [21] M. Brouard and C Vallance (Editors). *Tutorials in molecular reaction dynamics*. Royal Society of Chemistry, 2015.
- [22] M.T. Bell and T. P. Softley. Ultracold molecules and ultracold chemistry. *Mol. Phys.*, 107(2):99–132, 2009.
- [23] P.E. Siska. Molecular-beam studies of Penning ionization. *Rev. Mod. Phys.*, 65(2):337, 1993.
- [24] S. Falcinelli, J.M. Farrar, F. Vecchiocattivi, and F. Pirani. Quantum-state controlled reaction channels in chemi-ionization processes: Radiative (optical–physical) and exchange (oxidative–chemical) mechanisms. *Acc. Chem. Res.*, 53(10):2248–2260, 2020.
- [25] S. Falcinelli, F. Pirani, and F. Vecchiocattivi. The possible role of Penning ionization processes in planetary atmospheres. *Atmosphere*, 6(3):299–317, 2015.

- [26] V. Le Page, Y. Keheyan, T.P. Snow, and V.M. Bierbaum. Gas phase chemistry of pyrene and related cations with molecules and atoms of interstellar interest. *Int. J. Mass Spectrom.*, 185:949–959, 1999.
- [27] Q. Li, W. Zhu, X. Zhu, and Y. Pu. Effects of Penning ionization on the discharge patterns of atmospheric pressure plasma jets. *J. Phys. D Appl. Phys.*, 43(38):382001, 2010.
- [28] H. Hotop. Analyses of ions and electrons resulting from Penning ionization. *Radiat. Res.*, 59(2):379–404, 1974.
- [29] J. Jankunas, K. Jachymski, M. Hapka, and A. Osterwalder. Observation of orbiting resonances in $\text{He}(^3\text{S}_1) + \text{NH}_3$ Penning ionization. *J. Chem. Phys.*, 142(16):164305, 2015.
- [30] NIST chemistry webbook. <http://webbook.nist.gov/>, 2020.
- [31] P.R. Brooks and E.M. Jones. Reactive scattering of K atoms from oriented CH_3I molecules. *J. Chem. Phys.*, 45(9):3449–3450, 1966.
- [32] A. Orr-Ewing. Orientation and alignment of reaction products. *Annu. Rev. Phys. Chem.*, 45(1):315–366, 1994.
- [33] J. Aldegunde, M.P. de Miranda, J.M. Haigh, B.K. Kendrick, V. Sáez-Rábanos, and F.J. Aoiz. How reactants polarization can be used to change and unravel chemical reactivity. *J. Phys. Chem. A*, 109(28):6200–6217, 2005.
- [34] R.N. Zare. Laser control of chemical reactions. *Science*, 279(5358):1875–1879, 1998.
- [35] H.J. Loesch and A. Remscheid. Brute force in molecular reaction dynamics: A novel technique for measuring steric effects. *J. Chem. Phys.*, 93(7):4779–4790, 1990.
- [36] B. Friedrich and D.R. Herschbach. Spatial orientation of molecules in strong electric fields and evidence for pendular states. *Nature*, 353(6343):412–414, 1991.
- [37] G. Granucci, M. Persico, and P. Van Leuven. Alignment of molecules in pulsed resonant laser fields. *J. Chem. Phys.*, 120(16):7438–7445, 2004.
- [38] F. Wang, J. Lin, and K. Liu. Steric control of the reaction of ch stretch-excited CHD_3 with chlorine atom. *Science*, 331(6019):900–903, 2011.
- [39] T.D. Hain, R.M. Moision, and T.J. Curtiss. Hexapole state-selection and orientation of asymmetric top molecules: CH_2F_2 . *J. Chem. Phys.*, 111(15):6797–6806, 1999.
- [40] T.D. Hain, M.A. Weibel, K.M. Backstrand, and T.J. Curtiss. Rotational state selection and orientation of OH and OD radicals by electric hexapole beam-focusing. *J. Phys. Chem. A*, 101(41):7674–7683, 1997.
- [41] M. Brouard, H. Chadwick, S.D.S. Gordon, B. Hornung, B. Nichols, J. Klos, F.J. Aoiz, and S. Stolte. Fully quantum state-resolved inelastic scattering of $\text{NO}(X) + \text{Kr}$: Differential cross sections and product rotational alignment. *J. Chem. Phys.*, 141(16):164306, 2014.

Bibliography

- [42] M. Brouard, H. Chadwick, S.D.S. Gordon, B. Hornung, B. Nichols, F.J. Aoiz, and S. Stolte. Stereodynamics in NO (X)+ Ar inelastic collisions. *J. Chem. Phys.*, 144(22):224301, 2016.
- [43] D. Watanabe, H. Ohoyama, T. Matsumura, and T. Kasai. Effect of mutual configuration between molecular orientation and atomic orientation in the oriented Ar(3P_2)+ oriented CF₃H reaction. *Phys. Rev. Lett.*, 99(4):043201, 2007.
- [44] H. Ohoyama, F. Kubo, and T. Kasai. Multidimensional steric effects for the XeI*(B, C) formations in the oriented Xe*(3P_2 , $M_J = 2$)+ oriented CF₃I reaction. *J. Chem. Phys.*, 131(13):134306, 2009.
- [45] H. Ohoyama, K. Yasuda, and T. Kasai. Steric effect in the energy transfer reaction of oriented Kr(3P_2 , $M_J = 2$)+ CO. *J. Phys. Chem. A*, 113(51):14017–14021, 2009.
- [46] H. Ohoyama, K. Yasuda, and T. Kasai. Atomic alignment effects for the formation of excimers RgX*(B, C) in the reaction of oriented Rg (3P_2 , $M_J = 2$)(Rg= Xe, Kr, Ar)+ Halogen (X)-containing molecules. *J. Phys. Chem. A*, 113(52):14785–14790, 2009.
- [47] U. Even, J. Jortner, D. Noy, N. Lavie, and C. Cossart-Magos. Cooling of large molecules below 1 K and He clusters formation. *J. Chem. Phys.*, 112(18):8068–8071, 2000.
- [48] J.D. Weinstein, R. DeCarvalho, T. Guillet, B. Friedrich, and J.M. Doyle. Magnetic trapping of calcium monohydride molecules at millikelvin temperatures. *Nature*, 395(6698):148–150, 1998.
- [49] S.Y.T. van de Meerakker, H.L. Bethlem, N. Vanhaecke, and G. Meijer. Manipulation and control of molecular beams. *Chem. Rev.*, 112(9):4828–4878, 2012.
- [50] H.L. Bethlem, G. Berden, and G. Meijer. Decelerating neutral dipolar molecules. *Phys. Rev. Lett.*, 83(8):1558, 1999.
- [51] S.Y.T. van de Meerakker, P.H.M. Smeets, N. Vanhaecke, R.T. Jongma, and G. Meijer. Deceleration and electrostatic trapping of OH radicals. *Phys. Rev. Lett.*, 94(2):023004, 2005.
- [52] H.L. Bethlem, G. Berden, F.M.H. Crompvoets, R.T. Jongma, A.J.A. Van Roij, and G. Meijer. Electrostatic trapping of ammonia molecules. *Nature*, 406(6795):491–494, 2000.
- [53] M.R. Tarbutt, H.L. Bethlem, J.J. Hudson, V.L. Ryabov, V.A. Ryzhov, B.E. Sauer, G. Meijer, and E.A. Hinds. Slowing heavy, ground-state molecules using an alternating gradient decelerator. *Phys. Rev. Lett.*, 92(17):173002, 2004.
- [54] M. Kirste, X. Wang, H. C. Schewe, G. Meijer, K. Liu, A. van der Avoird, L.M.C. Janssen, K.B. Gubbels, G.C. Groenenboom, and S.Y.T. van de Meerakker. Quantum-state resolved bimolecular collisions of velocity-controlled OH with NO radicals. *Science*, 338(6110):1060–1063, 2012.

-
- [55] T. de Jongh, M. Besemer, Q. Shuai, T. Karman, A. van der Avoird, G.C. Groenenboom, and S.Y.T. van de Meerakker. Imaging the onset of the resonance regime in low-energy NO-He collisions. *Science*, 368(6491):626–630, 2020.
- [56] E. Narevicius, C.G. Parthey, A. Libson, J. Narevicius, I. Chavez, U. Even, and M.G. Raizen. An atomic coilgun: using pulsed magnetic fields to slow a supersonic beam. *New J. Phys.*, 9(10):358, 2007.
- [57] S.D. Hogan, A.W. Wiederkehr, H. Schmutz, and F. Merkt. Magnetic trapping of hydrogen after multistage Zeeman deceleration. *Phys. Rev. Lett.*, 101(14):143001, 2008.
- [58] E. Narevicius, A. Libson, C.G. Parthey, I. Chavez, J. Narevicius, U. Even, and M.G. Raizen. Stopping supersonic beams with a series of pulsed electromagnetic coils: an atomic coilgun. *Phys. Rev. Lett.*, 100(9):093003, 2008.
- [59] M. Motsch, P. Jansen, J.A. Agner, H. Schmutz, and F. Merkt. Slow and velocity-tunable beams of metastable He₂ by multistage Zeeman deceleration. *Phys. Rev. A*, 89(4):043420, 2014.
- [60] T. Rieger, T. Junglen, S.A. Rangwala, P.W.H. Pinkse, and G. Rempe. Continuous loading of an electrostatic trap for polar molecules. *Phys. Rev. Lett.*, 95(17):173002, 2005.
- [61] S.A. Rangwala, T. Junglen, T. Rieger, P.W.H. Pinkse, and G. Rempe. Continuous source of translationally cold dipolar molecules. *Phys. Rev. A*, 67(4):043406, 2003.
- [62] B. Bertsche and A. Osterwalder. State-selective detection of velocity-filtered ND₃ molecules. *Phys. Rev. A*, 82(3):033418, 2010.
- [63] S. Chervenkoy, X. Wu, J. Bayerl, A. Rohlfes, T. Gantner, M. Zeppenfeld, and G. Rempe. Continuous centrifuge decelerator for polar molecules. *Phys. Rev. Lett.*, 112(1):013001, 2014.
- [64] X. Wu, T. Gantner, M. Koller, M. Zeppenfeld, S. Chervenkoy, and G. Rempe. A cryofuge for cold-collision experiments with slow polar molecules. *Science*, 358(6363):645–648, 2017.
- [65] A. Bergeat, J. Onvlee, C. Naulin, A. Van Der Avoird, and M. Costes. Quantum dynamical resonances in low-energy CO ($j = 0$) + He inelastic collisions. *Nat. Chem.*, 7(4):349–353, 2015.
- [66] G. Dupeyrat, J. Marquette, and B.R. Rowe. Design and testing of axisymmetric nozzles for ion-molecule reaction studies between 20° K and 160° K. *Phys. Fluids*, 28(5):1273–1279, 1985.
- [67] I.R. Sims, J.L. Queffelec, A. Defrance, C. Rebrion-Rowe, D. Travers, P. Bocherel, B.R. Rowe, and I.W.M. Smith. Ultralow temperature kinetics of neutral–neutral reactions. the technique and results for the reactions CN + O₂ down to 13 K and CN + NH₃ down to 25 K. *J. Chem. Phys.*, 100(6):4229–4241, 1994.

Bibliography

- [68] C. Berteloite, M. Lara, A. Bergeat, S.D. Le Picard, F. Dayou, K.M. Hickson, A. Canosa, C. Naulin, J.M. Launay, I.R. Sims, and M. Costes. Kinetics and dynamics of the $S(^2D_1)+H_2 \rightarrow SH + H$ reaction at very low temperatures and collision energies. *Phys. Rev. Lett.*, 105(20):203201, 2010.
- [69] C. Amarasinghe and A.G. Suits. Intrabeam scattering for ultracold collisions. *J. Phys. Chem. Lett.*, 8(20):5153–5159, 2017.
- [70] C. Amarasinghe, H. Li, C.A. Perera, M. Besemer, J. Zuo, C. Xie, A. van der Avoird, G.C. Groenenboom, H. Guo, J. Kłos, and A.G. Suits. State-to-state scattering of highly vibrationally excited NO at broadly tunable energies. *Nat. Chem.*, 12(6), 528–534, 2020.
- [71] P.M. Koch and J.E. Bayfield. Electron loss in low-energy $H^+ - H$ (high n) merged-beam collisions. *Phys. Rev. Lett.*, 34(8):448, 1975.
- [72] H. Hus, F. Youssif, A. Sen, and J.B.A. Mitchell. Merged-beam studies of the dissociative recombination of H_3^+ ions with low internal energy. *Phys. Rev. A*, 38(2):658, 1988.
- [73] H. Bruhns, K.A. Kreckel, H. and Miller, X. Urbain, and D.W. Savin. Absolute energy-resolved measurements of the $H^- + H \rightarrow H_2 + e^-$ associative detachment reaction using a merged-beam apparatus. *Phys. Rev. A*, 82(4):042708, 2010.
- [74] J. Jankunas, B. Bertsche, and A. Osterwalder. Study of the $Ne(^3P_2) + CH_3F$ electron-transfer reaction below 1 K. *J. Phys. Chem. A*, 118(22):3875–3879, 2014.
- [75] A.J. Alexander, M. Brouard, K.S. Kalogerakis, and J.P. Simons. Chemistry with a sense of direction—the stereodynamics of bimolecular reactions. *Chem. Soc. Rev.*, 27(6):405–415, 1998.
- [76] E.J. Aoiz, M. Brouard, S.D.S. Gordon, B. Nichols, S. Stolte, and V. Walpole. A new perspective: imaging the stereochemistry of molecular collisions. *Phys. Chem. Chem. Phys.*, 17(45):30210–30228, 2015.
- [77] J. Zou, S.D.S. Gordon, and A. Osterwalder. Sub-Kelvin stereodynamics of the $Ne(^3P_2) + N_2$ reaction. *Phys. Rev. Lett.*, 123(13):133401, 2019.
- [78] M.H.G. De Miranda, A. Chotia, B. Neyenhuis, D. Wang, G. Quémener, S. Ospelkaus, J.L. Bohn, J. Ye, and D.S. Jin. Controlling the quantum stereodynamics of ultracold bimolecular reactions. *Nat. Phys.*, 7(6):502–507, 2011.
- [79] G. Scoles, D. Bassi, U. Buck, and D. Laine. *Atomic and molecular beam methods*, volume 1. Oxford university press, 1988.
- [80] J.M. Hayes and G.J. Small. Supersonic jets, rotational cooling, and analytical chemistry. *Anal. Chem.*, 55(4):565A–574A, 1983.

-
- [81] W. Christen, K. Rademann, and U. Even. Supersonic beams at high particle densities: Model description beyond the ideal gas approximation. *J. Phys. Chem. A*, 114(42):11189–11201, 2010.
- [82] H. Haberland, U. Buck, and M. Tolle. Velocity distribution of supersonic nozzle beams. *Rev. Sci. Instrum.*, 56(9):1712–1716, 1985.
- [83] M.D. Morse. Supersonic beam sources. *Exp. Methods Phys. Sci.*, 29:21–47, 1996.
- [84] P. Jansen and F. Merkt. Manipulating beams of paramagnetic atoms and molecules using inhomogeneous magnetic fields. *Prog. Nucl. Magn. Reson. Spectrosc.*, 120-121:118–148, 2020.
- [85] S. DePaul, D. Pullman, and B. Friedrich. A pocket model of seeded supersonic beams. *J. Phys. Chem.*, 97(10):2167–2171, 1993.
- [86] Y.T. Lee, J.D. McDonald, P.R. LeBreton, and D.R. Herschbach. Molecular-beam kinetics: Evidence for short-range attraction in halogen atom–molecule exchange reactions. *J. Chem. Phys.*, 49(5):2447–2448, 1968.
- [87] Y. Shagam and E. Narevicius. Sub-Kelvin collision temperatures in merged neutral beams by correlation in phase-space. *J. Phys. Chem. C*, 117(43):22454–22461, 2013.
- [88] B. Bertsche. *Low Energy Collisions in Merged Neutral Molecular Beams*. PhD thesis, EPFL, Lausanne, (6210), 2014.
- [89] A. Osterwalder. Merged neutral beams. *EPJ Tech. Instrum.*, 2(1):10, 2015.
- [90] A.J. Orr-Ewing and R.N. Zare. Orientation and alignment of reaction products. *Annu. Rev. Phys. Chem.*, 45(1):315–366, 1994.
- [91] D.J. Griffiths and D.F. Schroeter. *Introduction to quantum mechanics*. Cambridge University Press, 2018.
- [92] M.N.R. Ashfold, R.N. Dixon, R.J. Stickland, and C.M. Western. 2 + 1 MPI spectroscopy of B 1E” state NH₃ and ND₃: rotational analysis of the origin bands. *Chem. Phys. Lett.*, 138(2-3):201–208, 1987.
- [93] L. Fusina, G. Di Lonardo, and J.W.C. Johns. The ν_2 and ν_4 bands of ¹⁴ND₃. *J. Mol. Spectrosc.*, 118(2):397–423, 1986.
- [94] D. Papoušek, J.M.R. Stone, and V. Špirko. Vibration-inversion-rotation spectra of ammonia. a vibration-inversion-rotation Hamiltonian for NH₃. *J. Mol. Spectrosc.*, 48(1):17–37, 1973.
- [95] E.E. Nikitin and R.N. Zare. Correlation diagrams for hund’s coupling cases in diatomic molecules with high rotational angular momentum. *Mol. Phys.*, 82(1):85–100, 1994.

Bibliography

- [96] V. Henri and M.C. Teves. Absorption spectrum and constitution of sulphur vapour. predissociation of molecules. *Nature*, 114(2877):894–895, 1924.
- [97] S. Green and J. Hutson. Spectral line shape parameters for HF in a bath of Ar are accurately predicted by a potential inferred from spectra of the van der Waals dimer. *J. Chem. Phys.*, 100(2):891–898, 1994.
- [98] A. Garc a Vela. On the validity of the time-dependent self-consistent-field. approach: application to the vibrational predissociation of Cl₂–Ne. *Chem. Phys. Lett.*, 290(1-3):155–163, 1998.
- [99] A.J. McCaffery and R.J. Marsh. Vibrational predissociation of van der waals molecules: An internal collision, angular momentum model. *J. Chem. Phys.*, 117(20):9275–9285, 2002.
- [100] R.N. Zare. *Angular momentum: understanding spatial aspects in chemistry and physics*. Wiley-Interscience, 1988.
- [101] H. Morgner. Angular distribution of electrons emitted in Penning ionisation and similar processes. *Journal of Physics B: Atomic and Molecular Physics*, 11(2):269, 1978.
- [102] H. Morgner. Population of fine-structure levels of Ar⁺ (²P_{3/2,1/2}) in Penning ionisation of ar by metastable Ne*. *J. Phys. B At. Mol. Phys.*, 18:251–258, 1985.
- [103] T.F. O’Malley. Theory of dissociative attachment. *Phys. Rev.*, 150(1):14, 1966.
- [104] T.F. O’Malley. Theory of dissociative attachment. *Phys. Rev.*, 156(1):230, 1967.
- [105] C.A. Arango, M. Shapiro, and P. Brumer. Cold atomic collisions: Coherent control of Penning and associative ionization. *Phys. Rev. Lett.*, 97(19):193202, 2006.
- [106] S.S. Op De Beek, J.P.J. Driessen, and S. Kokkelmans. Ionization widths for Ne (3l)-Ar systems (l = s, p): Application to ionization and intramultiplet mixing cross sections. *Phys. Rev. A*, 56(4):2792–2805, 1997.
- [107] M.J. Verheijen and H.C.W. Beijerinck. State selected total Penning ionisation cross sections for the systems Ne*(³P₀, ³P₂) + Ar, Kr, Xe and N₂ in the energy range 0.06 < E₀(eV) < 8.0. *Chem. Phys.*, 102(1-2):255–273, 1986.
- [108] D. Hausamann and H. Morgner. The heteronuclear rare gas ions: a simple model for the determination of the potential curves. *Mol. Phys.*, 54(5):1085–1099, 1985.
- [109] T.E. Simos. A new numerov-type method for the numerical solution of the Schr dinger equation. *J. Math. Chem.*, 46(3):981–1007, 2009.
- [110] T.N. Rescigno and C.W. McCurdy. Numerical grid methods for quantum-mechanical scattering problems. *Phys. Rev. A*, 62(3):032706, 2000.

-
- [111] U. Even. The even-lavie valve as a source for high intensity supersonic beam. *EPJ Tech. Instrum.*, 2(1):17, 2015.
- [112] M. Zinner, P. Spoden, T. Kraemer, G. Birkel, and W. Ertmer. Precision measurement of the metastable 3P_2 lifetime of neon. *Phys. Rev. A*, 67(1):010501, 2003.
- [113] N.E. Small-Warren and L.C. Chiu. Lifetime of the metastable 3P_2 and 3P_0 states of rare-gas atoms. *Phys. Rev. A*, 11(6):1777, 1975.
- [114] C.E. Heiner, G. Meijer, and H.L. Bethlem. Motional resonances in a molecular synchrotron. *Phys. Rev. A*, 78(3):030702, 2008.
- [115] J. Jankunas, T.P. Reisman, K.S. and Rakitzis, and A. Osterwalder. Oriented O(3P_2), Ne(3P_2), and He(3S_1) atoms emerging from a bent magnetic guide. *Mol. Phys.*, 114(2):245–252, 2016.
- [116] <https://www.magnetic-declination.com/Switzerland/Lausanne/354325.html>, 2020.
- [117] W.C. Wiley and I.H. McLaren. Time-of-flight mass spectrometer with improved resolution. *Rev. Sci. Instrum.*, 26(12):1150–1157, 1955.
- [118] E.B. Saloman and C.J. Sansonetti. Wavelengths, energy level classifications, and energy levels for the spectrum of neutral neon. *J. Phys. Chem. Ref. Data*, 33(4):1113–1158, 2004.
- [119] T.P. Rakitzis and A.J. Alexander. Photofragment angular momentum distributions in the molecular frame. ii. single state dissociation, multiple state interference, and nonaxial recoil in photodissociation of polyatomic molecules. *J. Chem. Phys.*, 132(22):224310, 2010.
- [120] J. Zou, S.D.S. Gordon, S. Tanteri, and A. Osterwalder. Stereodynamics of Ne(3P_2) reacting with Ar, Kr, Xe, and N₂. *J. Chem. Phys.*, 148(16):164310, 2018.
- [121] S.Y. Tang, A.B. Marcus, and E.E. Muschlitz Jr. Velocity dependence of the ionization of Ar, Kr, and Xe on impact of metastable neon atoms. *J. Chem. Phys.*, 56(1):566–572, 1972.
- [122] R.H. Neynaber and G.D. Magnuson. Penning and associative ionization in the metastable neon-krypton system. *Phys. Rev. A*, 14(3):961, 1976.
- [123] R.H. Neynaber and G.D. Magnuson. Chemi-ionization in collisions of metastable neon with argon. *Phys. Rev. A*, 11(3):865, 1975.
- [124] W.P. West, T.B. Cook, F.B. Dunning, R.D. Rundel, and R.F. Stebbings. Chemiionization involving rare gas metastable atoms. *J. Chem. Phys.*, 63(3):1237–1242, 1975.
- [125] A. Niehaus. Penning ionization. *Ber. Bunsenges. Phys. Chem.*, 77(8):632–640, 1973.
- [126] H.L. Kramer, J.A. Herce, and E.E. Muschlitz Jr. Formation and collisional dissociation of heteronuclear rare-gas associative ions. *J. Chem. Phys.*, 56(8):4166–4170, 1972.

Bibliography

- [127] R.W. Gregor and P.E. Siska. Differential elastic scattering of $\text{Ne}^*(3\text{ s }^3P_{2,0})$ by Ar, Kr, and Xe: Optical potentials and their orbital interpretation. *J. Chem. Phys.*, 74(2):1078–1092, 1981.
- [128] C.A. Arango, M. Shapiro, and P. Brumer. Coherent control of collision processes: Penning versus associative ionization. *J. Chem. Phys.*, 125(9):094315, 2006.
- [129] S. Falcinelli, F. Vecchiocattivi, and F. Pirani. General treatment for stereo-dynamics of state-to-state chemi-ionization reactions. *Commun. Chem.*, 3(1):1–11, 2020.
- [130] A. Aguilar-Navarro, B. Brunetti, S. Rosi, F. Vecchiocattivi, and G.G. Volpi. Velocity dependence of the cross section for Penning and associative ionization of argon atoms by metastable neon atoms. *J. Chem. Phys.*, 82(2):773–779, 1985.
- [131] W. Bussert, T. Bregel, J. Ganz, K. Harth, A. Siegel, M.W. Ruf, H. Hotop, and H. Morgner. Ionizing collisions of laser-excited rare gas atoms. *J. Phys. Colloq.*, 46(C1):C1–199, 1985.
- [132] J. Zou and A. Osterwalder. Investigation of the low-energy stereodynamics in the $\text{Ne}(^3P_2) + \text{N}_2$, CO reactions. *J. Chem. Phys.*, 153(10):104306, 2020.
- [133] H. Hotop and A. Niehaus. Reactions of excited atoms and molecules with atoms and molecules: V. comparing of Penning electron and photoelectron spectra of H_2 , N_2 and CO. *Int. J. Mass Spectrom. Ion Phys.*, 5(5-6):415–441, 1970.
- [134] D.M. Sonnenfroh and S.R. Leone. Bimodal rotational distributions of N_2^+ produced in the thermal energy Penning ionization of N_2 by $\text{Ne}^*(^3P_2)$. *Int. J. Mass Spectrom. Ion Processes*, 80:63–82, 1987.
- [135] L. Appolloni, B. Brunetti, F. Vecchiocattivi, and G.G. Volpi. Penning and associative ionization of nitrogen, oxygen, carbon monoxide, and nitric oxide by collision with metastable neon atoms. *J. Phys. Chem.*, 92(4):918–921, 1988.
- [136] J. Baudon, P. Feron, C. Miniatura, F. Perales, J. Reinhardt, J. Robert, H. Haberland, B. Brunetti, and F. Vecchiocattivi. Optical potentials for $\text{Ne}^*(^3P_{2,0})\text{--Ar}$, N_2 interactions. *J. Chem. Phys.*, 95(3):1801–1807, 1991.
- [137] C.Y. Ng, T. Baer, and I. Powis. *Cluster ions*, volume 1. John Wiley & Son Limited, 1993.
- [138] E.J. Bieske, A.M. Soliva, and J.P. Maier. The $\text{B} \leftarrow \text{X}$ electronic spectrum of $\text{N}_2^+\text{--Ne}$. *J. Chem. Phys.*, 94(7):4749–4755, 1991.
- [139] R. Kong, X. Shan, S. Wang, Y. Zhang, L. Sheng, L. Hao, and Z. Wang. Experimental and theoretical study of $\text{Ne}\cdot\text{CO}$ cluster. *J. Electron Spectros. Relat. Phenomena*, 160(1-3):49–53, 2007.
- [140] S.D.S. Gordon and A. Osterwalder. The stereodynamics of ion forming reactions. *Int. Rev. Phys. Chem.*, 39(2):109–134, 2020.

- [141] S.D.S. Gordon and A. Osterwalder. Energy and orientation independence of the channel branching in $\text{Ne}^* + \text{ND}_3$ chemi-ionisation. *Phys. Chem. Chem. Phys.*, 21(26):14306–14310, 2019.
- [142] S.D.S. Gordon and A. Osterwalder. 3D-printed beam splitter for polar neutral molecules. *Phys. Rev. Appl.*, 7(4):044022, 2017.
- [143] E.W. Steer, L.S. Petralia, C.M. Western, B.R. Heazlewood, and T.P. Softley. Measurement of the orientation of buffer-gas-cooled, electrostatically-guided ammonia molecules. *J. Mol. Spectrosc.*, 332:94–102, 2017.
- [144] C.M. Western. PGOPHER: A program for simulating rotational, vibrational and electronic spectra. *J. Quant. Spectrosc. Radiat. Transf.*, 186:221–242, 2017.

Junwen Zou
Guiyuan, No.7, 401
528000, Foshan, China

Email : dwight.zou@gmail.com
Mobile : +8613924872183

EDUCATION

École polytechnique fédérale de Lausanne

Doctoral Assistant, Physical Chemistry
Thesis Advisor: Dr. Andreas Osterwalder
Low-energy Stereodynamics of Ion-forming Reactions

Lausanne, Switzerland

Sep. 2016 – Now

Ludwig Maximilian University of Munich

Master of Science, Material Science, GPA: 1.45/1.0
Thesis Advisor: Prof. Ulf Kleineberg
Phase-tagged Electron Dynamics on Attosecond Timescale

Munich, Germany

Oct. 2014 – Dec. 2015

Université de Rennes 1

Master of Science, Material Science, GPA: 14.8/20.0

Rennes, France

Sep. 2013 – Oct. 2014

Southwest University

Bachelor of Science, Physics, GPA: 3.75/5.0

Chongqing, China

Sep. 2009 – June. 2013

EXPERIENCE

Laboratoire Kastler-Brossel

Research Assistant
Simulation of Single Photon Emission in Dot-in-Rod Nanocrystal

Paris, France

May. 2014 – July. 2014

Laboratoire Charles Fabry

Research Assistant
Circuit Design for the Laser Frequency Locking

Palaiseau, France

Mar. 2016 – July. 2016

PUBLICATIONS

- [1] **Zou, J.**, and Osterwalder, A. (2020). Investigation of the low-energy stereodynamics in the $\text{Ne}(^3P_2) + \text{N}_2$, CO reactions. The Journal of Chemical Physics, 153(10), 104306.
- [2] **Zou, J.**, Gordon, S. D., and Osterwalder, A. (2019). Sub-Kelvin Stereodynamics of the $\text{Ne}(^3P_2) + \text{N}_2$ Reaction. Physical Review Letters, 123(13), 133401.
- [3] Gordon, S. D., Omiste, J. J., **Zou, J.**, Tanteri, S., Brumer, P., and Osterwalder, A. (2018). Quantum State Controlled Channel Branching in Cold $\text{Ne}(^3P_2) + \text{Ar}$ Chemi-Ionisation. Nature Chemistry, 10, 1190-1195.
- [4] **Zou, J.**, Gordon, S. D., Tanteri, S., and Osterwalder, A. (2018). Stereodynamics of $\text{Ne}(^3P_2)$ reacting with Ar, Kr, Xe, and N_2 . The Journal of Chemical Physics, 148(16), 164310.
- [5] Gordon, S. D., **Zou, J.**, Tanteri, S., Jankunas, J., and Osterwalder, A. (2017). Energy Dependent Stereodynamics of the $\text{Ne}(^3P_2) + \text{Ar}$ Reaction. Physical Review Letters, 119(5), 053001.
- [6] Schmidt, J., Guggenmos, A., Chew, S.H., Gliserin, A., Hgner, M., Kling, M.F., **Zou, J.**, Spth, C., and Kleineberg, U. (2017). Development of a 10 kHz high harmonic source up to 140 eV photon energy for ultrafast time-, angle-, and phase-resolved photoelectron emission spectroscopy on solid targets. Review of Scientific Instruments, 88(8), 083105.

CONFERENCES

- CCMI 2018 "Stereodynamics of $\text{Ne}(^3P_2) + \text{X}$ ($\text{X}=\text{Rg}, \text{N}_2$) Reactions" Athens, GA, US (Poster)
- iCOMET 2019 "Sub-Kelvin Stereodynamics of the $\text{Ne}(^3P_2) + \text{N}_2$ Reaction" Hefei, China (Talk)
- Fall Meeting of the SCS 2018 "Stereodynamics of $\text{Ne}(^3P_2) + \text{X}$ ($\text{X}=\text{Rg}, \text{N}_2$) Reactions", Lausanne, Switzerland (Poster)
- Fall Meeting of the SCS 2019 "Sub-Kelvin Stereodynamics of the $\text{Ne}(^3P_2) + \text{N}_2$ Reaction", Zurich, Switzerland (Poster)

AWARDS

Teaching excellence award 2018

SCGC, EPFL

SKILLS

Computer: Fortran, LaTeX, LabVIEW, COMSOL, SOLIDWORKS, MATLAB

Laboratory: Mass spectrometry, Vacuum technique, Cryogenics, Laser